ENGINEERING GUIDELINES FOR THE EVALUATION OF HYDROPOWER PROJECTS

CHAPTER 11 - ARCH DAMS

MARCH 14, 2018

FEDERAL ENERGY REGULATORY COMMISSION

888 First Street NE

Washington, DC 20426

TABLE OF CONTENTS

11-1 INTRODUCTION

11-1.1 Purpose

This chapter of the Guidelines provides guidance on the criteria and procedures used by the FERC to evaluate the safety and structural integrity of existing arch dams under its jurisdiction.

The material presented in this chapter assumes that the reader has a general knowledge and understanding of the basic principles of arch dams, i.e., how they are designed, constructed, operated, and maintained.

The intent of this chapter **is not** to mandate new analyses and investigations regardless of whether or not they are needed. Rather, the variety of issues addressed and computation methods put forward are an attempt to anticipate the variety of problems that could be encountered. This chapter should not be interpreted as requiring every test, analysis, and investigation that it describes at every dam. It may well be that for a given dam, specific failure mechanisms suggested in this chapter are not pertinent. Analysis should always be directed at evaluating the viability of potential failure modes. **If there are no failure modes of concern, then no analysis is necessary.**

11-1.2 Applicability

This guidance is applicable to FERC engineers and licensees engaged in the safety evaluation of existing arch dams.

11-1.3 Definition of Safety

Safety is defined as the adequacy against an uncontrolled release of reservoir water. It is safety that has to be demonstrated by the licensee or the licensee's consultant.

11-1.4 Evaluation Criteria

Evaluation of safety involves the identification of all possible failure modes, and then demonstrating through engineering principles that the failure modes are not credible. For explanation of the potential failure mode analysis (PFMA), see Chapter 14 of this guideline.

Factors of safety are tied to the failure mode being considered. For example: Failure modes that involve sliding on failure plane are analogous to the failure modes describe in Chapter 3. Similar factors of safety would be expected. Dynamic failure modes will require a case by case evaluation. Factors of safety for rock erosion failure modes may be difficult to quantify.

11-1.4.1 Review of Existing Data and Site Inspection

A thorough knowledge must first be gained on a dam. Construction records and photographs are of great value. Dam instrumentation records should be reviewed, especially to identify any trends or long term changes in behavior.

Review of PFMA is extremely important. The PFMA of record should be reviewed to see that all potential failure modes have been identified and appropriately categorized. Potential failure modes must be described in sufficient detail so that the full path to failure is clearly understood. For example, "Overstressing of dam causes failure" is not acceptable. A better description is shown below:

1) Thermal loading causes cracking at or near the dam foundation from station 2+35 to 4+19.
2) Significant load is transferred around this area to the right thrust block.
3) Additional dam thrust destabilizes thrust block.
4) Thrust block movement is sufficient to deny arch action to the dam.
5) Monoliths 1 and 2 topple.
6) Reservoir is lost.

Engineering analyses should be reviewed and their adequacy judged by whether or not they address the concerns of the PFMA.

11-1.4.2 Method of Analysis

Analysis methods must be capable of addressing the failure mode of concern. This guideline does not require a specific type of analysis. Rather it requires that failure modes be appropriately evaluated. Consider the failure mode outlined above. A linear elastic finite element analysis could indicate whether or not thermal loading is likely to cause cracking. A non-linear finite element analysis, which admits cracking and sliding, could determine how much load is transferred away from the cracked area and onto the thrust block. The non-linear analysis could also tell how much the thrust block is likely to slide and whether Monoliths 1 and 2 are likely to topple.

Since a failure mode requires a chain of events to occur, one can evaluate the credibility of the failure mode at any one event. If for example, it can be shown that there is not enough dam thrust to move the thrust block under any scenario, then whether or not thermal cracking occurs becomes irrelevant and need not be investigated.

The FERC does not endorse any particular dam evaluation software. However, it is imperative that modeling assumptions consider the actual physical characteristics of the dam. Almost all arch dams consist of cantilever monoliths separated by vertical joints. In addition, the rock abutments that arch dams rely on for support are jointed. These joints cannot sustain tension. Analyses that fail to account for jointing and known pre-existing cracks are often misleading and should therefore be avoided.

11-1.5 General Geometric Considerations

Arch dams are suited for relatively narrow valleys with competent rock in the abutments. Typically the angle subtended by the arch at the crest is between 90° and 120°. The arch radius at the crest is typically between 1 and 2 times the height of the dam. Thickness at the base of the crown cantilever is typically 15 to 25 percent of the height.

Noted Swiss dam engineer Giovanni Lombardi proposed the "Lombardi Number", sometimes called the "Boldness Factor" for the categorization of arch dams. The number is dimensionless and is defined as follows:

$$\frac{S^2}{VH}$$

Where S is the surface area of the middle surface of the dam, V is the dam volume, and H is the height of the crown cantilever. Lombardi opines that when the number is 20 or greater, the dam is likely to have problems with excessive shear at the rock/concrete interface.

When the radius of curvature is significantly greater than the height of the dam, the dam can act more like a curved gravity dam than a true arch.

This guideline should not be interpreted as a condemnation of dams that fall outside of these basic geometric rules. However dams that are significantly outside of these parameters may warrant special scrutiny.

11-2 FOUNDATION CONSIDERATIONS

11-2.1 General

The abutments of an arch dam are particularly critical to the stability of the dam because they are required to resist the majority of the reservoir forces that attempt to push the structure in a downstream direction. Foundation information must provide sufficient geological detail to identify and locate any potential sliding wedges of rock that could cause instability. If such features are found to exist, a stability analysis must be performed to assure that there is an adequate factor of safety against abutment sliding. FERC staff must require that sufficient information and analysis be provided to support a review that verifies the findings with regard to the stability of the foundation and abutments.

11-2.2 Field Investigations

Field investigations are well described in Chapter 5 of these Guidelines and in the U.S. Army Corps of Engineers EM 1110-1-2908 (1994). The following narrative is intended as a summary and for the purpose of additional elaboration where required to specifically address the requirements of this Guideline.

11-2.2.1 Foundation Features That Create Stability Concerns and Warning Signs

Jointing - A feature of primary concern is a large wedge of rock in an abutment foundation created by a planar rock fracture or the intersection of two or more rock fractures whose intersection trend daylights in a downstream direction. Because of the high intact strength of most rock formations, failure is improbable unless it can occur along preexisting fractures. For a failure to occur, movement of the rock wedge must be kinematically possible. In other words, the

orientation of the rock fractures or slide planes must daylight in a direction that allows movement to take place. In addition, the joint must have enough persistence to allow movement to occur without shearing a great deal of intact rock.

In addition to joint orientation, joint connectivity must be considered. Joint connectivity determines whether kinematically possible wedges are small, and of little consequence, or large and capable of compromising the stability of the dam. See Figure 11-2.1 for an example of a potential abutment wedge stability problem.

Fig. 11-2.1

Hydrostatic Pressure - The stability of an abutment rock wedge is affected by the hydrostatic pressure in the joints that define the wedge as can be seen in Figure 11-2.2. Rock blocks that are perfectly stable in the dry can become very unstable if the joints defining them become pressurized. The drilling of joint drainage holes to relieve hydrostatic pressure is often very effective in increasing wedge stability. However, drain holes can be plugged or freeze in the winter. When abutment stability relies on drainage, the drains must be maintained.
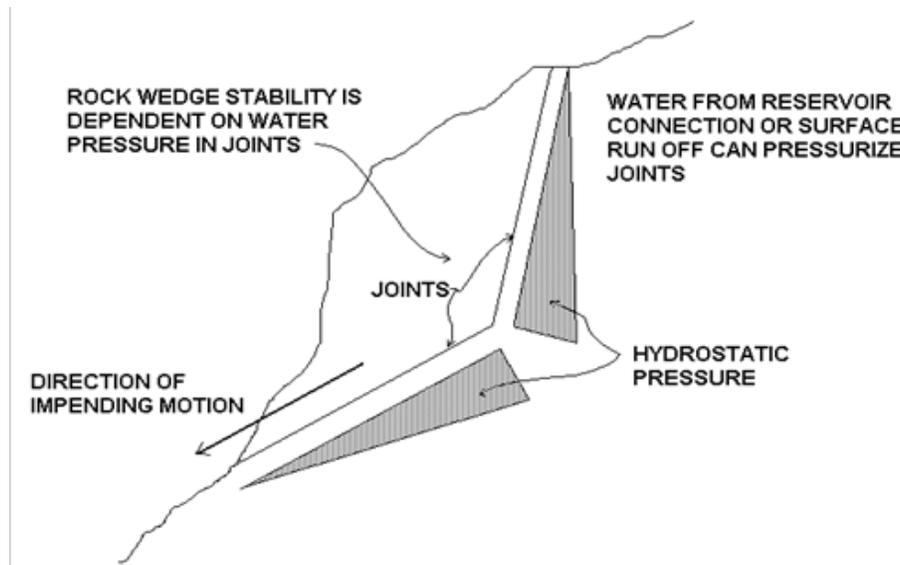
Fig. 11-2.2

Faults - Zones of faulted or sheared rock within the foundation must be carefully considered. A fault is a rock fracture distinguished from a joint by virtue of translational movement of one wall relative to the other wall at some time during the geologic record. If a fault is found to be present, the question as to whether it is active or inactive must be answered. If it is determined to be an active fault, its effect upon the structure during movement must be very carefully assessed and appropriately acted upon.

Additionally, the fault's effect upon the static stability of the foundation must be determined. Since it is a pre-sheared feature in the rock, it probably provides a plane of reduced strength to resist movement. In many cases slickensides and clay gouge are formed, which greatly reduce the rock strength. The fault orientation is significant in the effect it has on reducing stability against sliding in the foundation.

Another concern is the permeability of a through-going fault. If the sheared rock is very brittle and the shearing process forms a zone of primarily broken rock (breccia), it may form a highly permeable path for water passage beneath the dam. If the shearing movement forms a clay gouge within the breccia zone, the result may be a very impervious barrier in the foundation. Such a barrier to seepage can in some configurations result in the development of abnormally high uplift pressure in the foundation.

Coal Seams - Coal seams or beds in the foundation of an arch dam are a feature of concern. The clay layers associated with coal beds are an even greater concern. This combination in the foundation of an arch dam can form a plane with significantly lower shearing resistance than the surrounding rock. It should be evaluated both for planar failure and as a wedge in combination with the fracture pattern existing in the rock mass.

<u>Planar Features</u> - Planar features such as bedding, fissility, shale or clay seams, schistocity, foliation, cleavage, and stress relief features such as exfoliation and valley relief joints may all form sides of a rock wedge and therefore are features of some concern to be included in the abutment foundation stability analysis.

<u>Sudden Changes in Stiffness</u> - Adjacent rock beds with radically different moduli of deformation are of some concern. This difference may cause unexpected stress concentrations.

11-2.3 Material Parameter Selection

Experienced engineering and geologic judgment are very important in the selection of foundation material parameters for use in analytical procedures. Refer to the <u>Rock Testing Handbook </u>(1990) for more detail on laboratory testing than provided in this Guideline.

11-2.3.1 Shear Strength of Foundation Interface

Sliding at the concrete/foundation interface is not often an issue for arch dams. However, it can be a failure mode if the dam's length to height ratio is large. In addition, if the dam relies on thrust blocks for support, the thrust blocks' stability may be controlled by sliding.

Factors to be considered in estimating the shear strength of the foundation interface include base friction angle and the roughness or asperity angle "i" of the interface, and embedment of the structure into the rock. The typical foundation contact is cracked due to the annual thermal cycling of the dam, which causes the dam to deflect upstream and downstream. For this reason, cohesion is typically not assumed at the interface, unless it is the cohesion associated with shearing through asperities. If cohesion is used, the asperity angle should not be used because the cohesion assumes shearing through asperities.

The roughness or asperity angle may be difficult to estimate and because of this may have to be ignored. In some cases, it may be possible to estimate the asperity angle from photographs of the foundation prior to concrete placement. Another possibility is to estimate the irregularity from closely spaced core borings. Refer to Figure 11-2.3 for a diagrammatic representation of interface roughness.
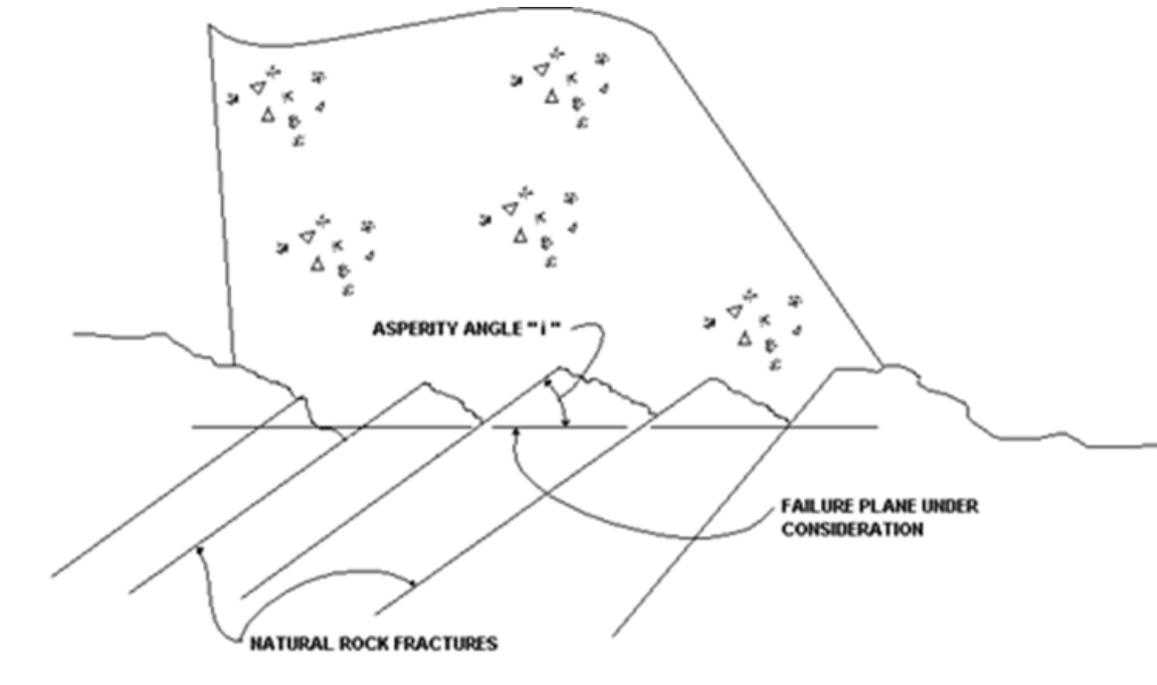
Fig. 11-2.3

Where information exists for determination of an asperity angle at the interface between the structure and the foundation, this angle may be added to the friction angle as a resisting force in the stability analysis if the least resistance to sliding includes overriding the irregularities. It is not applicable where the least resistance is developed by shearing through the rock of the irregularities.

Embedment may possibly be determined from as-built drawings, construction photographs, and borings. This factor can be very important for preventing sliding on the interface provided the concrete is placed against the embedded surface, which would mobilize the downstream rock strength before movement could occur.

The process of evaluating the possibility of a sliding failure for arch dams is not as straight forward as is the case of gravity dams. Failure mechanisms must be considered in 3D. If the arch is well keyed into the foundation, downstream sliding can only be enabled by up the abutment sliding. Figure 11-2.4, depicts the direction and magnitude of foundation thrust force at the dam/foundation interface for a typical arch dam.
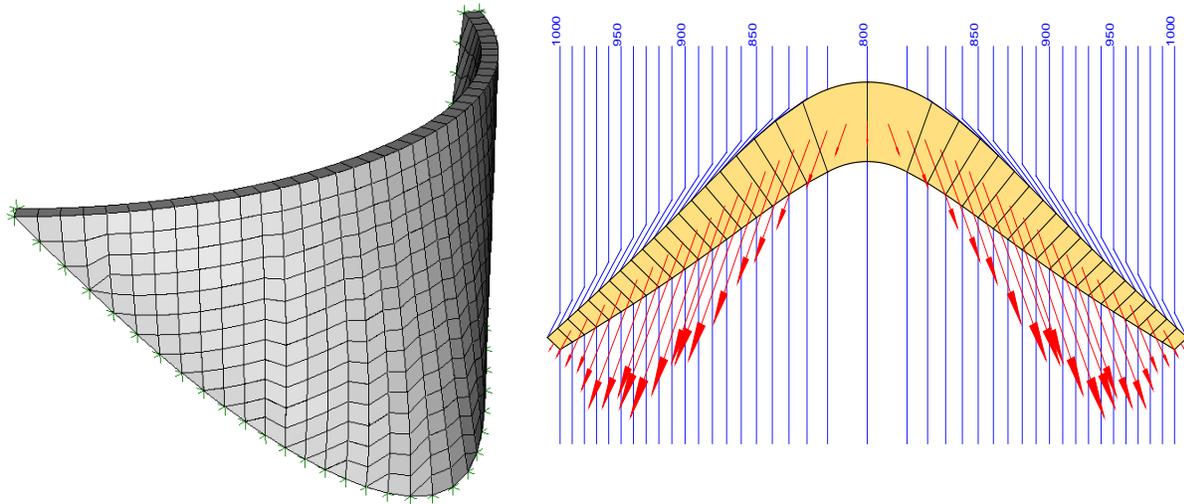
Fig. 11-2.4

Local exceedance of the shear strength of the interface may not be an indication of dam failure. Excessive shear stress may be able to be re-distributed. However, once peak shear strength is exceeded, shear strength should be downgraded to residual values.

A sliding factor of safety (FSS) that characterizes the ability of the arch to redistribute shear along the interface can be developed by conducting sequential nonlinear analyses in which the friction angle is incrementally reduced to determine the limiting value. The limiting value is the lowest friction angle for which the software can find a numeric solution.

$$FSS = \frac{\tan \theta_{actual}}{\tan \alpha_{limit}}$$

Where: θ_{actual} = actual interface friction angle

α_{limit} = limiting value determined by analysis

11.2.3.2 Dam/Foundation Keying

The orientation of the contact surface between the dam and foundation is of great importance. Note the contour lines in the following example (Figure 11-2.5).
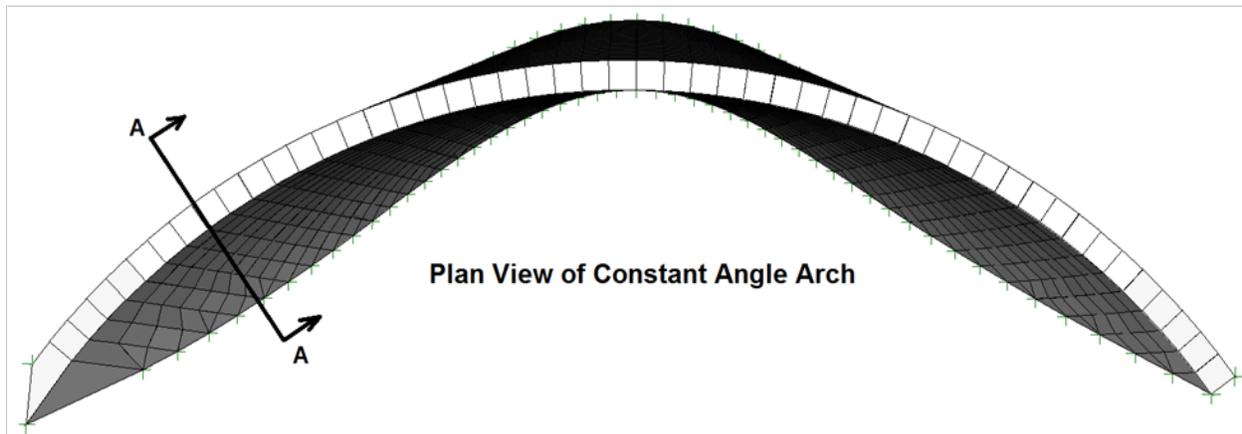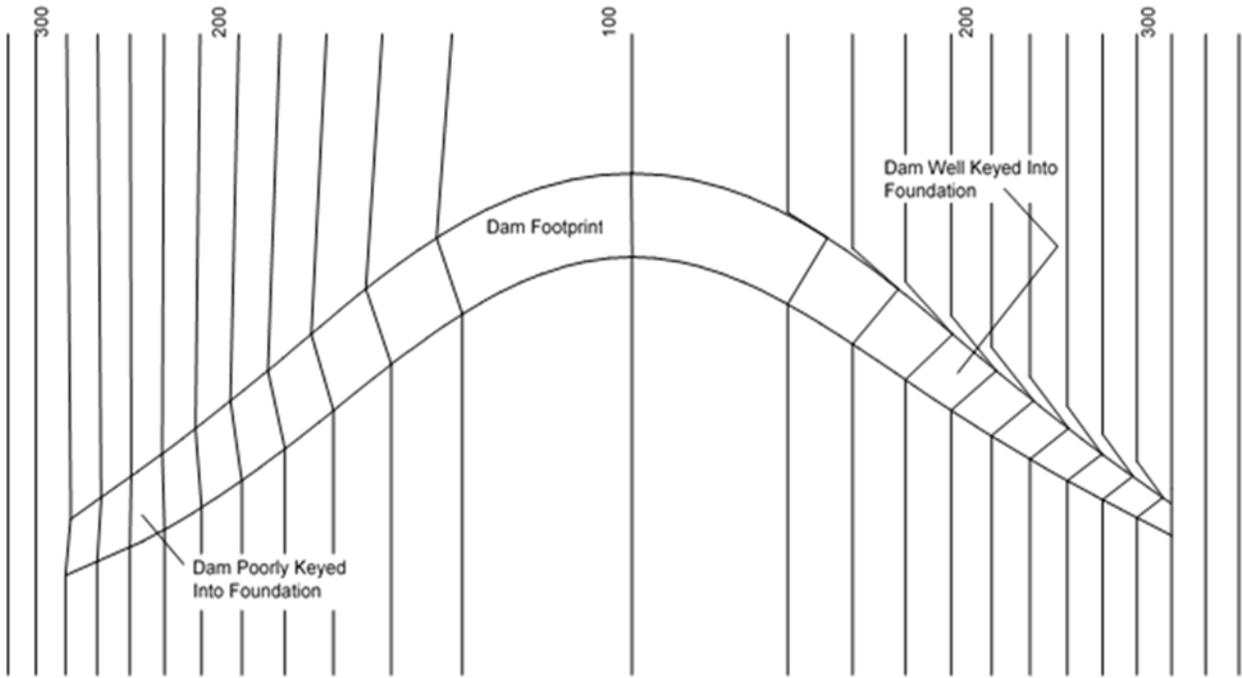
Fig. 11-2.5

Contours on the left abutment indicate that the contact between dam and foundation is oriented in such a way that the dam cannot slide downstream without sliding up the abutment. This is a well keyed situation. Contours on the right side however indicate that the dam is not keyed into the abutment at all. Note Section A-A shown in yellow on the side view of the dam. The arch thrust vectors cross the dam/foundation contact at a very acute angle.
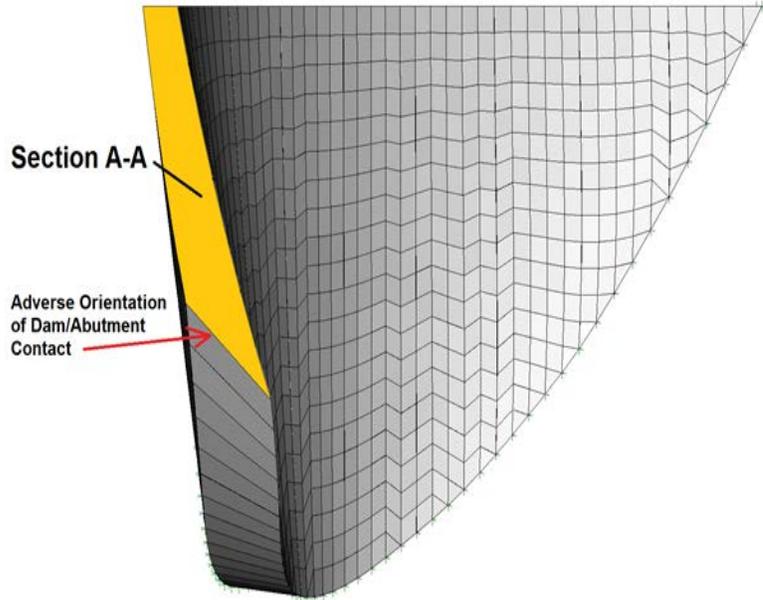
Local sliding will occur, which will deny the arch necessary support. The stress plot below shows the flow of stress around this area. Note the stress' tendancy to dive below the area of adverse orintation.
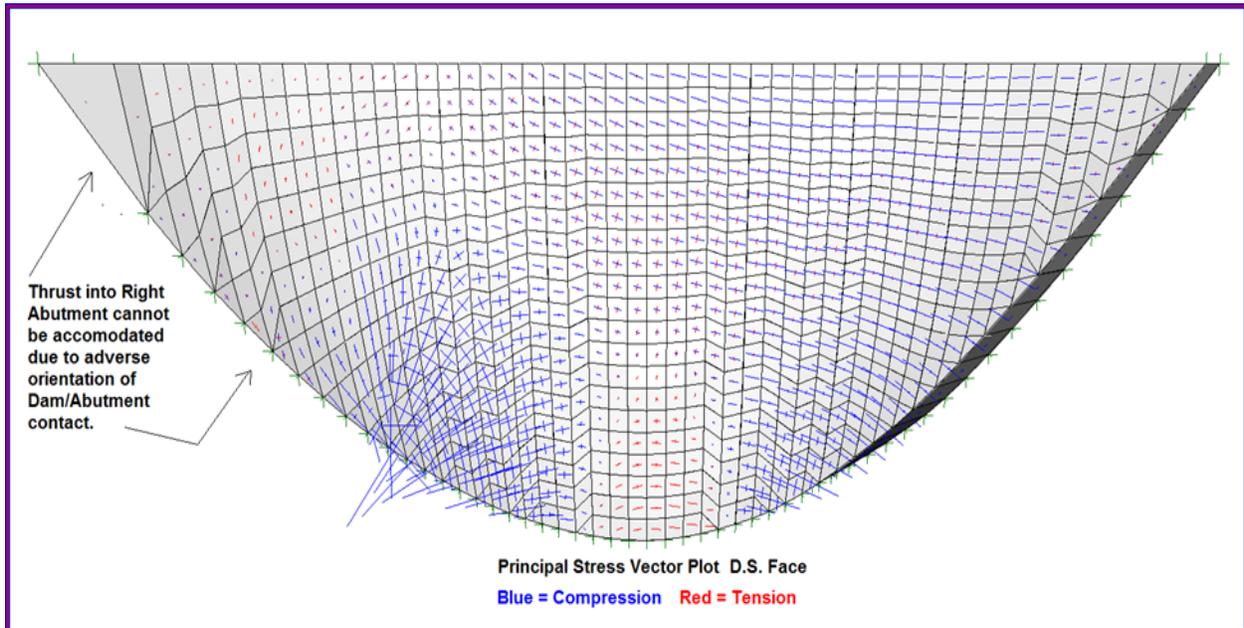
Fig. 11-2.6

The result of the local sliding is the negation of arch action on the right side. Failure of the right side monoliths will result as shown in Figure 11-2.7.
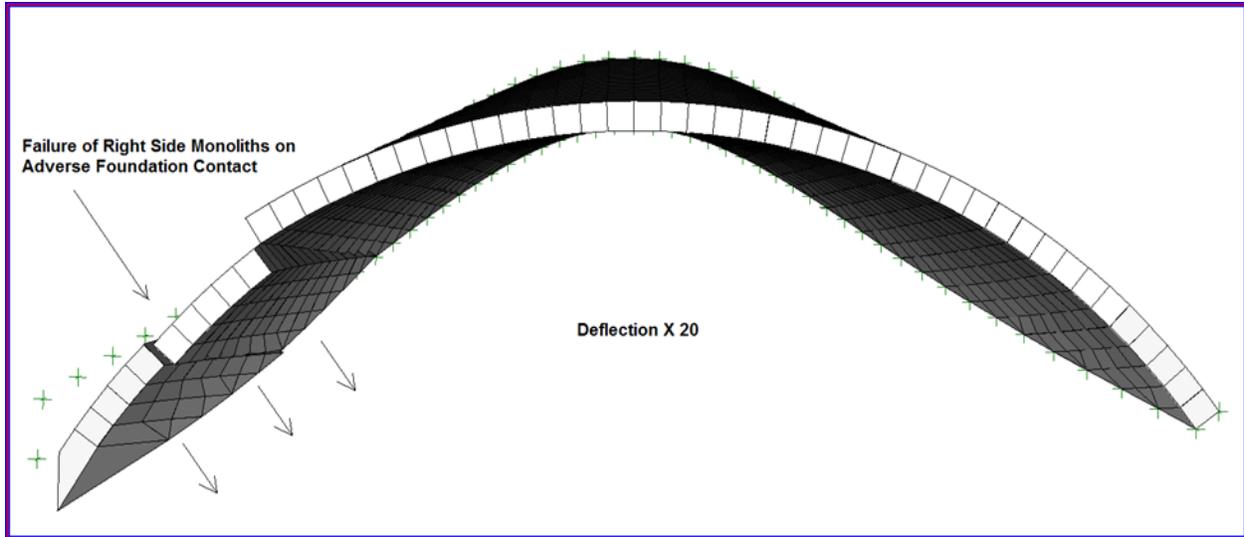
Fig. 11-2.7

11-2.3.3 Potential Foundation Failure Planes and Wedges

The abutment foundations are particularly critical to the stability of an arch dam. Abutment instability can develop along either a planar discontinuity or a combination of planar discontinuities, which intersect to form an unstable wedge.

Sliding on a plane in 3D requires a generalization of the 2D sliding concepts used in gravity dams.

An arbitrarily oriented plane has an upward directed normal vector. Any applied force that makes an angle less than the friction angle, (φ) will not cause sliding. Any applied force that makes an angle with the normal greater than φ will cause sliding (see Figure 11-2.8). The definition of sliding factor of safety is:

Fig. 11-2.8

$$FSS = \frac{Tan(\phi)}{Tan(\alpha)} \qquad (11\text{-}2.1)$$
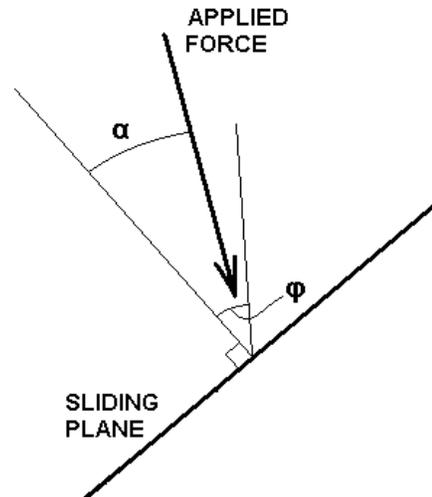
Definition of potential sliding planes in 3D is by specification of strike and dip. Strike is the angle of the line formed by the intersection of the sliding plane with horizontal, measured eastward from north. The dip is the angle between the sliding plane and horizontal (see Figure 11-2.9). If i, j, and k are the unit normal vectors in the east, north, and up directions

11-11

respectively, then the i, j, and k coordinates of the strike, the dip, and the upward directed normal to the sliding plane are as follows:

	i	j	k
Strike	Sin(S)	Cos(S)	0
Dip	Cos(S)*Cos(D)	-Sin(S)*Cos(D)	-Sin(D)
Normal	Cos(S)*Sin(D)	-Sin(S)*Sin(D)	Cos(D)

(11-2.2)

Figure 11-2.9 depicts the Friction Cone. This cone is the 3D generalization of Figure 11-2.8. Force vectors within the cone will not cause sliding, force vectors outside the cone will. Factor of safety is still defined as shown by Equation 11-2.1, but the determination of the angle between the upward directed normal to the sliding plane and the applied force vector (α) must be done in 3D. This can be done using vector dot products.
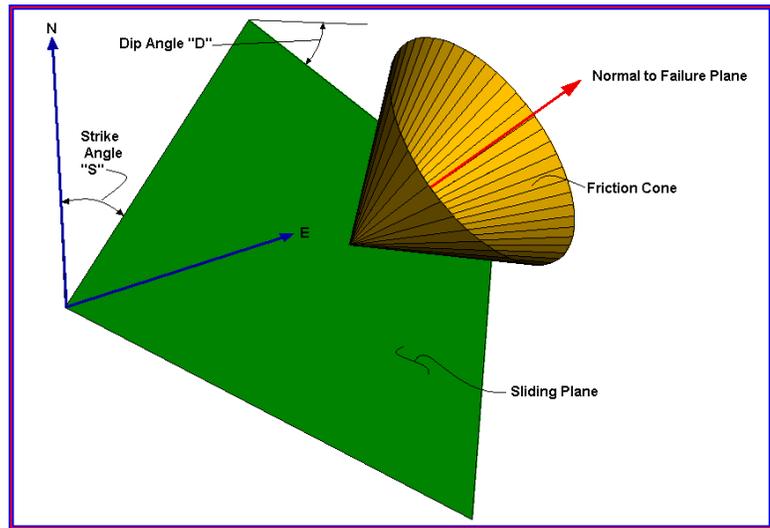
Fig. 11-2.9

$$Cos(\alpha) = -\frac{\vec{F}}{|F|} \bullet \vec{N} \qquad (11-2.3)$$

Consider the following example. A sliding plane exists striking North 30° East dipping 50°. (See Figure 11-2.10) The i, j, and k coordinates of the upward directed unit normal vector to the sliding plane are:

$$i = Cos(30)*Sin(50) = 0.663$$
$$j = -Sin(30)*Sin(50) = -0.383$$
$$k = Cos(50) = 0.643$$

Now consider a force vector with the following components:

$$F_{East} = -20, \quad F_{North} = 10, \quad F_{Up} = -30$$

11-12

The total magnitude of the force is:

$$\sqrt{(-20)^2 + 10^2 + (-30)^2} \ = \ 37.42$$
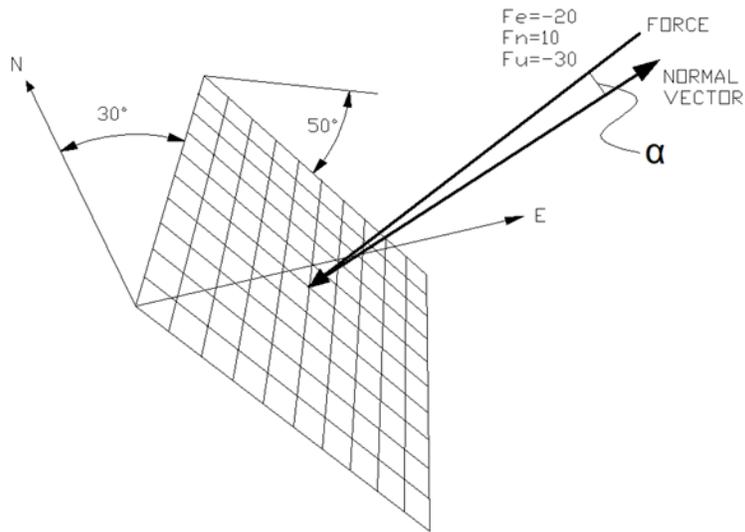
Fig. 11-2.10

The normalized force vector is then:

$$i = -20/37.42 = -0.535$$
$$j = 10/37.42 = 0.267$$
$$k = -30/37.42 = -0.802$$

From Equation 11-2.3:

$$Cos(\alpha) = 0.535*0.663 + 0.267*0.383 + 0.802*0.643 = 0.973 \rightarrow \alpha = 13.4°$$

A factor of safety can now be compared to the friction angle using Equation 11-2.1.

Sliding can also occur on two intersecting joint planes. Consider Figure 11-2.11, the force vector F is the sum of applied forces acting on the wedge, including the wedge weight, any hydrostatic forces, and dam thrust.

$$-\vec{F} = \vec{N}1 + \vec{N}2 + \vec{V}$$

N1•i + N2•i + V•i = -F•i

N1•j + N2•j + V•j = -F•j

N1•k + N2•k + V•k = -F•k

$$\text{Safety Factor} = \frac{\left(\left|\vec{N}1\right|*Tan(\varphi 1) \ +\left|\vec{N}2\right|*Tan(\varphi 2)\right)}{\left|\vec{V}\right|}$$
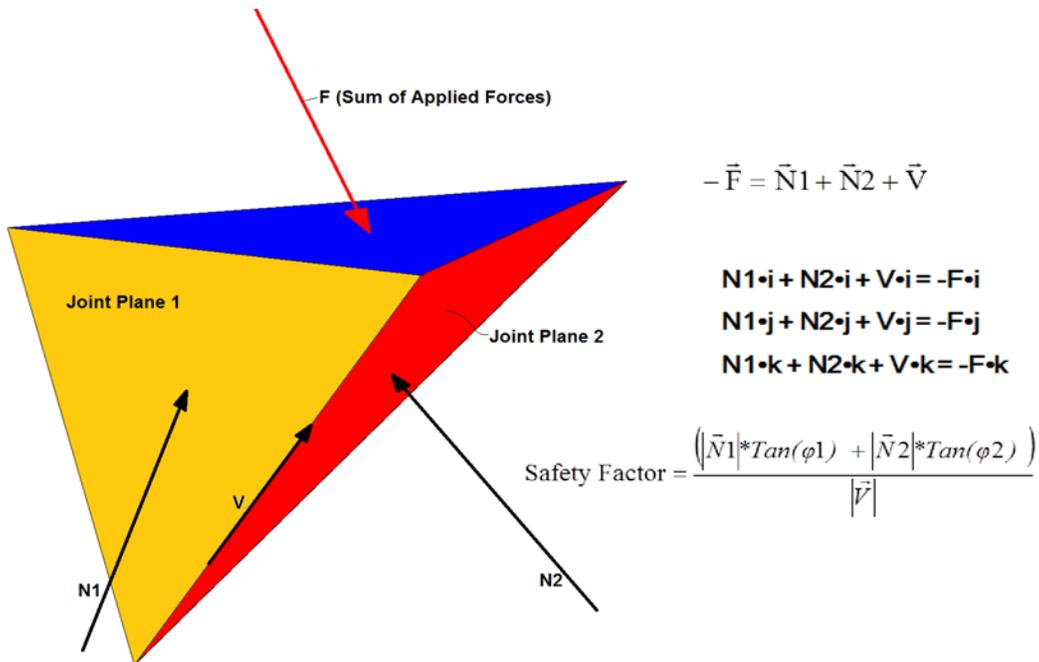
Fig. 11-2.11

The vectors N1 and N2 are acting normal to their respective joint planes. If two plane sliding is to occur, then the direction of sliding must be along a line which defines the intersection of plane 1 and 2. A 3rd vector "V" is defined by this intersection.

From simple force equilibrium, one can write the above equations, where i, j, and k are the unit vectors in the east, north, and upward directions respectively. Note that the magnitude of V is limited by the frictional resistance generated by N1 and N2.

An example of rock wedge instability and its effect on arch dam behavior is presented below.

Fig. 11-2.12

Vertical Release
Plane Assumed

Trace of Joint 1 Daylighting
on Abutment

20

75

Trace of Joint 2 Daylighting
on Abutment

Keel Formed by
Intersecting Joint
Planes
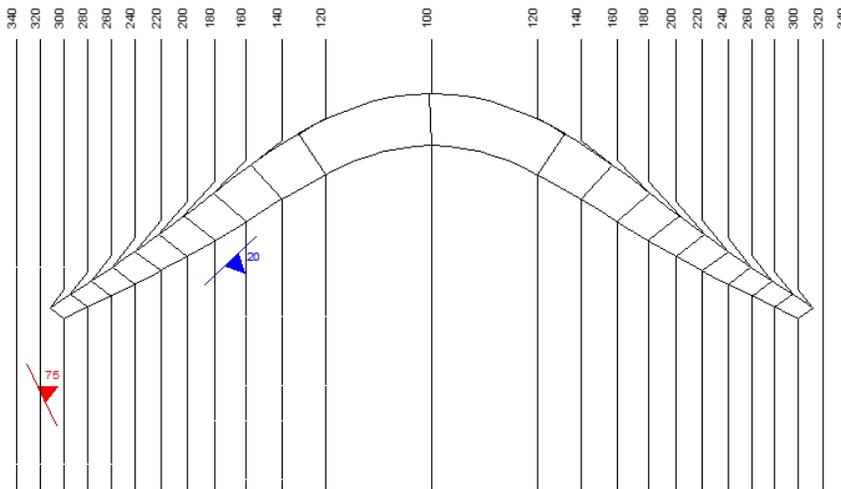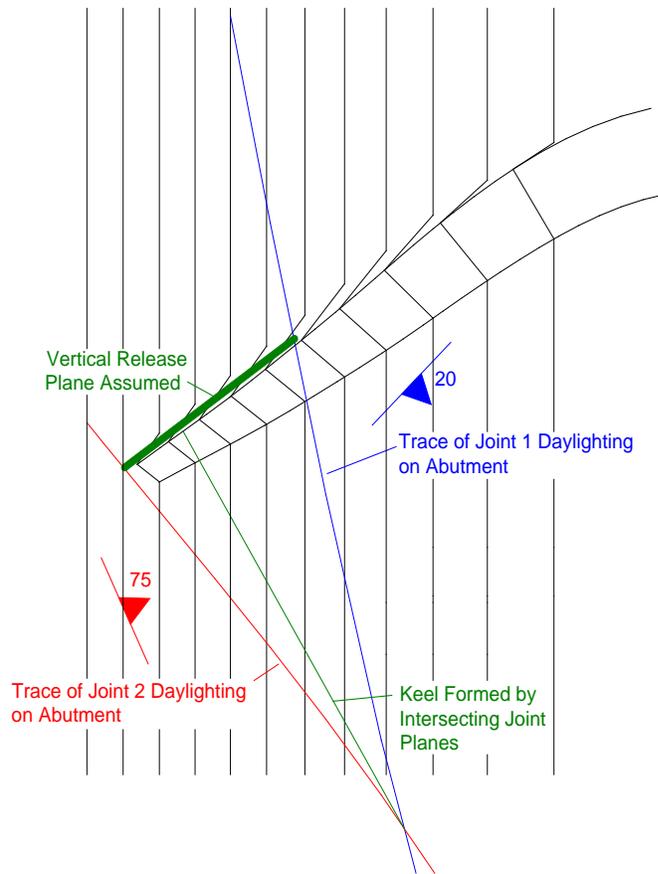
Fig. 11-2.13

As can be seen from the contour lines in Figure 11-2.12, the dam is well keyed into the abutments. However, all rock masses are jointed. Here the right abutment has two joints. Joint 1 (blue) strikes North 45° East dipping 20°. Joint 2 (red) strikes North 25° West dipping 75°.

These joints daylight as shown adjacent.

They also intersect along a keel line shown in green. We shall posit a vertical release plane upstream of the dam. Its exact geometry is not very important and its existence need not be proven. This release plane and Joint 1 and 2 define a roughly tetrahedral wedge.

The reason to posit a release plane is that the contrary assumption (no release plane) necessarily implies that:

1) The jointed rock mass has sufficient tensile capability to restrain motion downstream along the keel.
2) The rock mass in not pervious and so reservoir pressure cannot exert itself on the wedge.

Neither of these are reasonable assumptions.

Figure 11-2.14 is a 3D rendering of the dam and rock wedge. The figure depicts the geometry of the wedge defined by the intersecting Joints 1 and 2 and the release plane.

Note that it is possible for the wedge to slide while in contact with both joint planes in the direction of the keel line. It is also possible to slide on Joint 1 alone, moving away Joint 2 toward the river valley. However this motion would be inhibited at the upstream side of the wedge by the thrust of the dam.
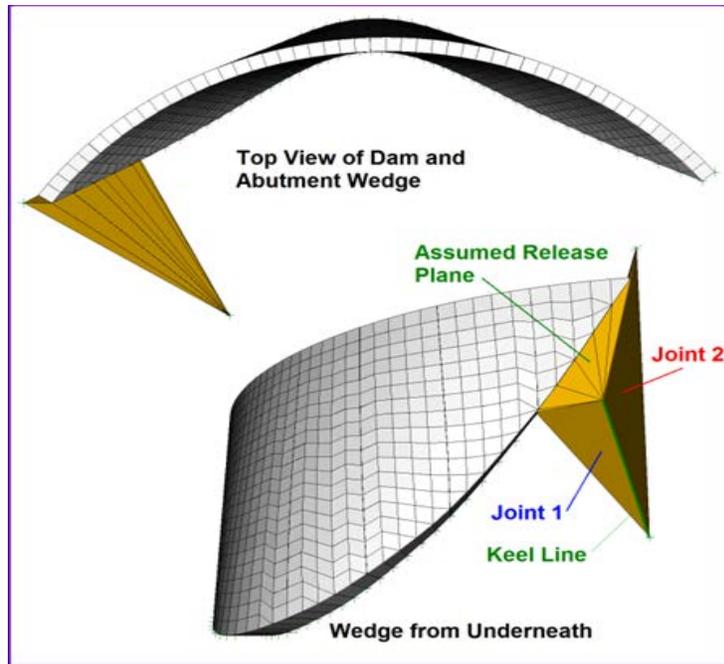
Fig. 11-2.14

The magnitude and direction horizontal components of the forces acting on the wedge are depicted in Figure 11-2.15. Note that there is a large force in the direction of the river channel produced by hydrostatic pressure on the joint planes. This force can be greatly reduced if the joint planes are drained. Hydrostatic force will be applied to the release plane in any case, however it may be possible through drainage to reduce or eliminate the pressure in the joint planes downstream of the dam.

The forces applied to the wedge, in addition to the wedge weight must be equilibrated by forces normal to the joint planes and whatever shear forces can be sustained on the joint planes.

Fig. 11-2.15

11-16
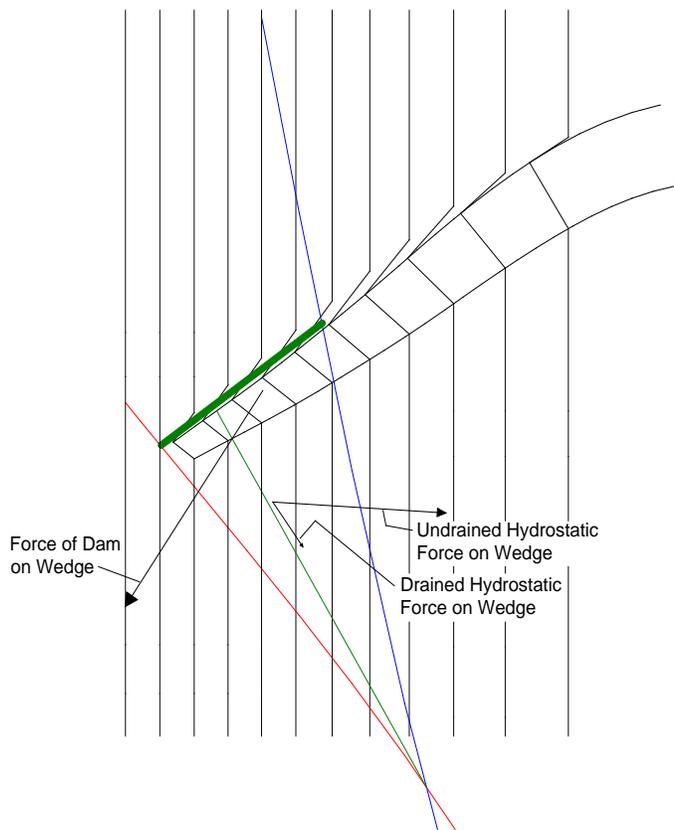
The tables below show the sum of forces acting on the wedge for both the case of hydrostatic pressure acting on the joint planes, and the case where hydrostatic pressure is relieved through drainage.

Undrained Case

Force (kips)	Riverward	Upstream	Up
Wedge Weight			-11699
Dam Thrust	-10469	-15586	-6352
Hydrostatic	13167	-791	9698
Total→	2698	-16377	-8354

Drained Case

Force (kips)	Riverward	Upstream	Up
Wedge Weight			-11699
Dam Thrust	-10469	-15586	-6352
Hydrostatic	2280	-3228	15
Total→	-8189	-18814	-18036
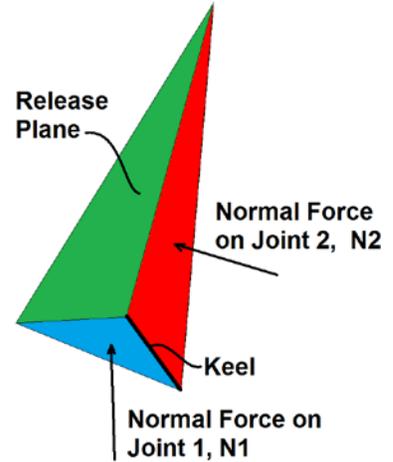
Based on the strike and dip of the joint planes and Equations 11.2.2, the i, j, and k coordinates of N1, N2, and V are:

	i	j	k
N1	0.242	-0.242	0.940
N2	0.875	0.408	0.259
V	0.478	-0.813	-0.332

Therefore, for the undrained case;

$$||N1||*(0.242) + ||N2||*(0.875) + ||V||*(0.478) = -2698$$

$$||N1||*(-0.242) + ||N2||*(0.408) + ||V||*(-0.813) = 16377$$

$$||N1||*(0.940) + ||N2||*(0.259) + ||V||*(-0.332) = 8354$$

(Refer to Figure 11-2.11)

Solving this set of simultaneous equations results in:

$$||N1|| = 1060 \text{ kips}, ||N2|| = 6122 \text{ kips}, ||V|| = -17387 \text{ kips.}$$

Note that the vector V is limited by joint plane friction. The magnitude of V cannot exceed ||N1||*tan(φ1) + ||N2||*tan(φ2), where φ1 and φ2 are Joint 1 and 2 friction angles. If it does, sliding will occur. Therefore a factor of safety can be defined as follows:

$$FS = \frac{[\left\|N1\right\| * Tan(\varphi 1) + \left\|N2\right\| * Tan(\varphi 2)]}{\left\|V\right\|}$$

If the joint friction angles are 35°, the resulting factor of safety is 0.29 for the undrained case. For the drained case, the factor of safety is ≈1.0.

The calculations above broke the analysis process up into two distinct phases. First, the dam was analyzed assuming that the rock wedge would be capable of resisting whatever forces the dam imposed on it. Once these forces were determined, the stability of the wedge was evaluated. This approach is valid, yet sometimes overly conservative, as it ignores strain compatibility. Movement of the wedge will change the load applied to it by the dam. In some cases, stability may be achieved by the forces in the dam altering their trajectories around the wedge area as the wedge shifts slightly.

Rather than break the analysis into two uncoupled phases, it is possible to evaluate total system stability in one phase by incorporating the wedge into the model of the dam. If this is done, strain compatibility is satisfied and the possibility of stress redistribution resulting in an altered stable condition is admitted.

Consider the undrained case. The results of this type of analysis are shown in Figure 11-2.17. Initially the force from the dam acted to push the wedge into the abutment. However, wedge movement all but eliminates the thrust from the dam. While the upstream corner of the wedge is restrained by the portion of the dam it is still in contact, the rest of the wedge slides away from the Joint 2 plane and moves riverward on the Joint 1 plane being driven largely by the hydrostatic force in Joint 2.

The far right dam monolith bears mostly on the wedge, but a portion of it is founded left of the wedge. As the wedge moves, the monolith pivots about the vertical contraction joint it is keyed to and also begins to rotate downstream.
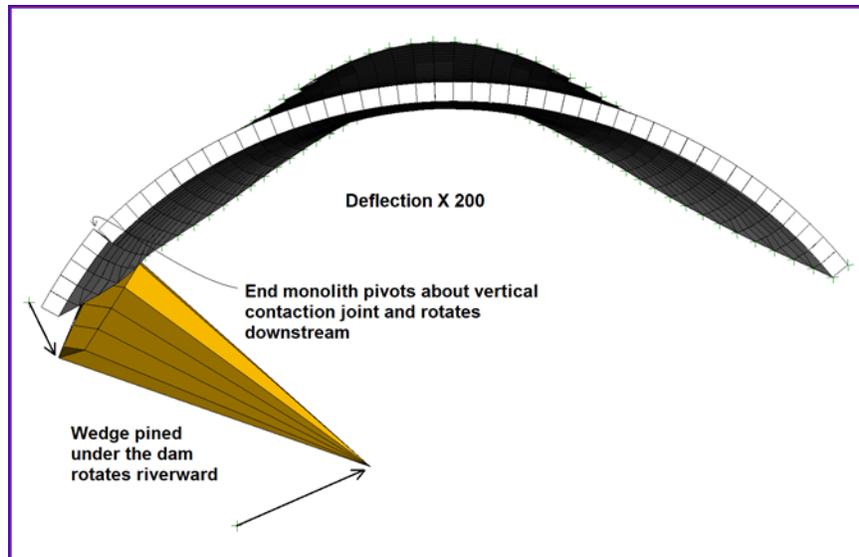
Fig. 11-2.17

Failure in non-linear analyses is indicated by the inability of the mathematical algorithm to converge. In this case, the model did not converge, indicating that there was no way to achieve force equilibrium in the dam/wedge system.

In this case, the finite element solution results in the same conclusion as did the two phase analysis that was initially done. Note however that the two phase analysis indicated sliding along the keel line, whereas the fully coupled strain compatible analysis indicates that the wedge slides out from under the dam and then begins to rotate riverward. The possibility of rotational movement cannot be captured with conventional kinematic block analysis.

An event tree is listed below:

1. There is a moveable rock wedge in the abutment of sufficient size such that loss of the wedge would leave a significant portion of the dam unsupported.
2. There is a reduction in the ratio of resisting forces to driving forces due to any number of events:
    a. A seismic event induces some block movement, opening up joints to water flow from the reservoir, increasing uplift on the slide planes.
    b. A seismic event produces enough movement to reduce the joint plane friction angle from peak to residual.
    c. Rain water from a large storm runs into the joints, pressurizing them.
    d. Etc.
3. Resisting forces are overcome and the wedge moves.
4. The movement does not reduce driving forces or increase resisting forces, so movement continues.
5. The dam has insufficient redundancy to bridge over the wedge.
6. The dam fails.

11-2.3.4 Foundation Modulus of Deformation

The modulus of deformation provides a measure of the overall foundation stiffness. It attempts to factor in the jointing and lack of homogeneity in foundation. It is a representation of the deformational property of the rock mass as a whole, with all its discontinuities, as contrasted with the modulus of elasticity of an intact specimen of the rock.

The parameter is of importance if accurate stress determinations (especially near the foundation interface) are required for the evaluation of a failure mode. However, in most cases, the inelastic behavior of the dam is of greatest importance (sliding, overturning, etc.). Therefore, accurate determination of the foundation modulus is often not critical. It is not unreasonable to assume a foundation modulus in the range of 2×10^6 psi.

If a failure mode is contingent upon the accurate determination of the deformation modulus, analyses with upper and lower bound deformation moduli should be performed in order to bracket behavior.

Where no data is available, it is possible to develop an estimate of the foundation modulus by testing representative intact specimens of the rock obtained from core samples to determine modulus of elasticity of intact rock, then applying an appropriate reduction factor to convert from the modulus of elasticity of the intact rock to the modulus of deformation of the rock mass. Refer to Hendron (1968) for a study, which demonstrated that the fracture frequency in the rock mass is a primary factor in the reduction of the elastic modulus of a rock mass from the modulus of an intact specimen. Hendron provides examples of how rock quality designation (*RQD*) and velocity ratio may be used to estimate the appropriate reduction factor.

Table 11-2.1 Geomechanics Classification of Jointed Rock Masses (Bieniawski, 1990)

A. Classification Parameters and Their Ratings.

	PARAMETER		RANGE OF VALUES						
1	Strength of intact rack material	Point-load strength index	>10MPa	2 - 4 MPa	2 - 4 MPa	1 - 2 MPa	For this low range, uniaxial compressive test is preferred		
		Uniaxial Compressive strength	>250MPa	100-250 MPa	50–100 MPa	25-50 MPa	5-25 MPa	1 -5 MPa	<1 MPa
	Rating		15	12	7	4	2	1	0
2	Drill core quality RQD		90% - 100%	75% - 90%	50% - 75%	25%- 50%	<25%		
	Rating		20	17	13	8	3		
3	Spacing of discontinuities		> 2 m	0.6-2 m	200-600 mm	60-200 mm	< 60 mm		
	Rating		20	15	10	8	5		
4	Condition of discontinuities		Very rough surface Not continuous No separation Unweather-ed wall rack	Slightly rough surface Separation < 1 mm slightly weathered walls	Slightly rough surface Separation < 1 mm Highly weathered walls	Slicken-sided surface OR Gauge < 5 mm thick OR Separation 15 mm continuous	Soft gauge > 5 mm thick OR Separation >5 mm Continuous		
	Rating		30	25	20	10	0		
5	Ground Water	inflow per 10 m tunnel length	None	< 10 liters/min	10-25 liters/min	25-125 liters/min	> 125 liters/min		
		Ratio: (joint water pressure)/(major principle stress)	OR_____ 0 OR_____	OR_____ 0.0 - 0.1 OR_____	OR_____ 0.1 - 0.2 OR_____	OR_____ 0.2 - 0.5 OR_____	OR_____ > 0.5 OR_____		
		General Conditions	Dry	Damp	Wet	Dripping	Flowing		
	Rating		15	10	7	4	0		

B. Rating Adjustment for Joint Orientation.

Strike and dip orientations for joints		Very favorable	Favorable	Fair	Unfavorable	Very unfavorable
Ratings	Tunnels	0	-2	-5	-10	-12
	Foundations	0	-2	-7	-15	-25
	Slopes	0	-5	-25	-50	-60

C. Rock Mass Classes Determined From Total Rating.

Rating	100←81	80←61	60←41	40←21	<20
Class No.	I	II	III	IV	V
Description	Very good rock	Good rock	Fair rock	Poor rock	Very poor rock

D. Meaning of Rock Mass Classes.

Class No.	I	II	III	IV	V
Average Stand-up time	10 years for 15 m span	6 months for 8 m span	1 week for 5 m span	10 hours for 2.5m span	30 minute for 1m span
Cohesion of the rock mass	> 400 kPa	300-400 kPa	200-300 kPa	100-200 kPa	<100 kPa
Friction angle of rock mass	>45	35 - 45	25 – 35	15 - 25	<15

Galera, Alvarez, and Bieniawski (2007) developed a relationship between Bieniawski's (1979) Rock Mass Rating (RMR) system and the modulus of deformation of rock masses which has been shown to be valid on other projects. This relationship is as follows:

$$E_m = E_i * e^{\frac{(RMR-100)}{36}}$$ (11-2.4)

Where: E_m = Modulus of Deformation measured in gigapascals (GPa)

E_i = Intact Rock Modulus

1 GPa = 145,037.7 psi.

Factors included in Bieniawski's *RMR* are unconfined compressive strength or point load strength index, *RQD*, spacing of discontinuities, condition of discontinuities, and ground water. Refer to Table 11-2.1 for his Geomechanics Classification of Jointed Rock Masses.

It must be realized that the modulus of deformation is often difficult to quantify. The techniques discussed above can be useful, however it may be more prudent to run several analyses with differing foundation moduli bracketing reasonable expected values rather than to spend effort in laboratory testing and field investigations attempting to more precisely quantify the modulus of deformation.

11-2.4 Foundation Rock Erodibility

The erosion of a plunge-pool downstream of a functioning arch dam spillway is a common occurrence unless measures have been taken to prevent it. It is a natural way for the energy of the falling water to be dissipated. Erosion of even very strong and massive rock can occur at the

location of impingement of the water falling from a high dam spillway. Two examples of deep erosion of strong rock include the 79 ft. (24m) deep plunge-pool eroded in blocky andesite at Alder Dam in the USA and the 65 ft. (20m) deep plunge-pool eroded in excellent granite at Picote Dam in Portugal described by Mason (1984). Typically, the rate of plunge-pool erosion decreases with depth until a stable configuration is reached. Plunge-pools are sometimes planned for in the design of a spillway as a means of energy dissipation, but plunge-pool formation can cause a stability problem if it continues to grow laterally, eroding the dam foundation.

Figure 11-2.18 depicts two failure modes of concern. First, if plunge-pool erosion unlocks rock blocks and allows wedges underneath the dam to be blown out by the reservoir pressure, the entire reservoir could escape underneath the dam. Second, if the undermining is of sufficient extent, the dam itself could be destabilized to the point of failure.
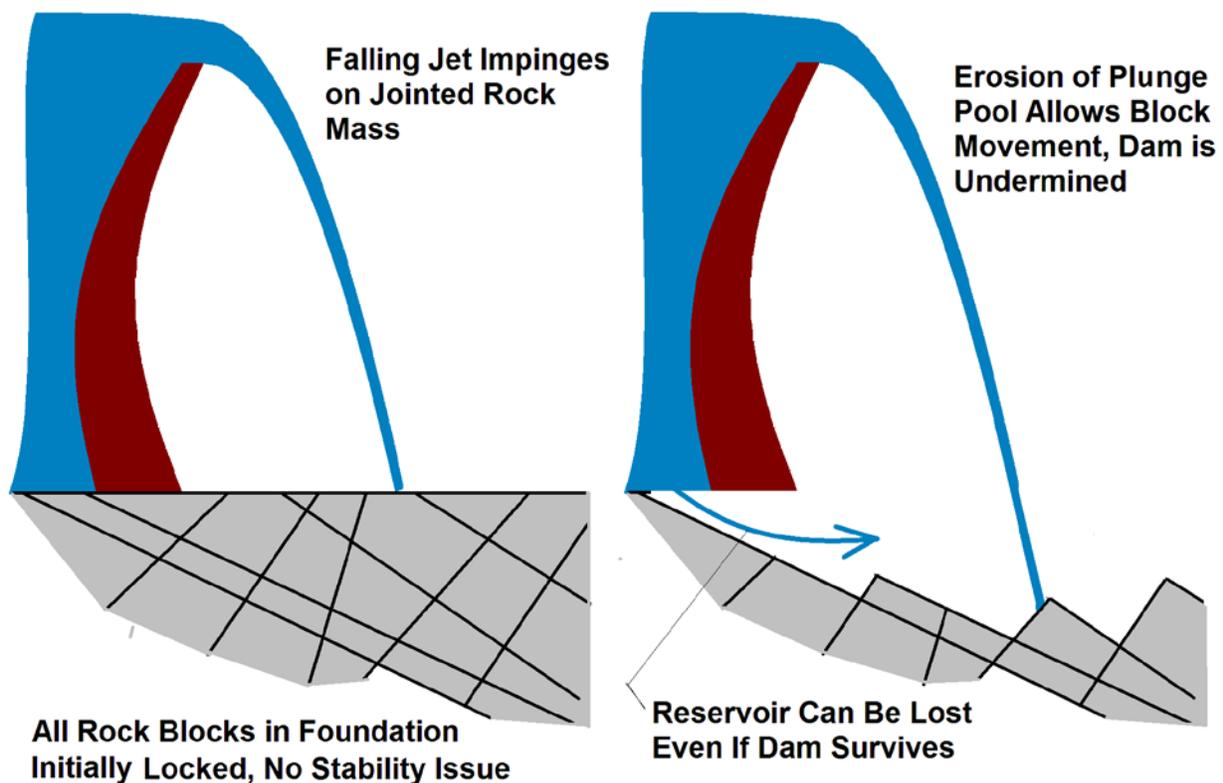
Fig. 11-2.18

11-2.4.1 Field Investigations

If the dam has a history of flood discharges, much can be learned from how the plunge pool area has held up under previous floods. Field investigations can be conducted to determine the extent of previous erosion that may have occurred and to provide data for determining the threat to the structure posed by possible future erosion during flood events. Investigations may include

hydrographic surveys to establish the depth and extent of an existing plunge-pool, and by repeating surveys after spillway flows it is possible to determine plunge-pool stabilization or continued growth. Engineering geology investigations can be conducted to provide data on the foundation rock conditions including such things as rock type, fracture spacing and condition, bedding frequency, zones of weaker rock such as softer beds and sheared rock zones, unconfined compressive strength, orientation of beds and fractures, etc. Borings may be required to provide data for the engineering geology investigations.

11-2.4.2 Assessing the Erodibility of Rock

The erodibility of rock has been the subject of numerous studies by both engineering geologists and hydraulic engineers. These studies have provided considerable insight into this very complex problem. The complexity of the interaction of the water forces with the endless variety of rock conditions encountered, however, makes each situation unique.

Rock erodibility is controlled by the following factors:

1. Intact rock strength (unconfined compressive strength).
2. Fracture frequency (size of individual rock blocks).
3. Orientation of fracture sets.
4. Shear strength and condition of fractures (continuity, roughness, aperture opening, in-filling material and alteration or weathering condition of wall rock).
5. Weak planes in the intact rock (bedding, foliation, schistocity, fissility, etc.)
6. Faults and shear zones.

An assessment of rock erodibility must take these factors into account. For detailed guidance on assessment of rock erosion, see Appendix A of this chapter.

11-2.4.3 Historic Observations of the Depth and Extent of Erosion

Table 11-2.11 shows that in some cases deep erosion has been experienced even though the rock in the impact area was apparently hard. In general the depth of erosion depends upon the energy of the falling jet, the duration of the flow, and the character of the rock.

Table 11-2.2 Historic Scour Depths of Plunge-Pools.

	Material	Country	q (cfs/ft)	Head (ft)	Depth (ft)
Alder	Andesite	USA	20,000[2]	300	79
Naciemento	SS, MS[1]	USA		250	
Picote	Granite	Portugal	1250	213	118
Kariba	Gneiss	Zimbabwe		415	160
Tarbela	Limestone	Pakistan	570	320	121
			854	323	160
Karakaya		Turkey	1034	413	131
			619	403	90
Keban		Turkey	351	360	75
				335	44
Killckaya		Turkey	130	245	39
Elmali	Granite		32	89	49
Kondopoga	Granite		149	39	21
Cabora Bassa		Mozambique	2957	300	223
			283	315	75
Ukai	Basalt	India	854	154	95
Guri	Basalt	Venezuela	52,800[2]		118

[1] Abbreviations are: SS-Sandstone, MS-Mudstone.
[2] Only the total discharge for the spillway was available.

11-3 CONCRETE MATERIAL PARAMETERS

Concrete properties are required for analyses. The analyses performed are contingent upon failure modes. Therefore the importance of a given concrete property is a function of how it affects the failure mode under consideration.

Previous arch dam guidelines had allowable stress acceptance criteria. Typically, a linear elastic analysis was performed, either by finite element or trial load, and the stress results were compared with "allowable" stresses that were typically some fraction of the compressive strength. This being the case, accurate determination of the compressive strength was of great importance.

This guideline has no allowable stress acceptance criteria.

Sampling and testing programs must be aimed at determining properties that matter to the failure modes in question.

11-3.1 Visual Inspection of the Concrete

Careful visual inspection is the most important investigation that can be done. For example, it is usually the case that a crack in the concrete has far more effect on the behavior of the dam than does a variation in ultimate compressive strength or the modulus of elasticity.

11-3.2 Ultrasonic Pulse Velocity Test

The purpose of in-situ ultrasonic pulse velocity or UPV testing is to evaluate the overall quality of concrete in existing concrete dams. Suitable equipment and standard procedure for pulse velocity tests are described in ASTM C-597. The method is based on the principle that the velocity of an ultrasonic pulse through a material is related to dynamic modulus of elasticity, density, and Poisson's ratio of the material. Any changes in the modulus caused by deterioration, cracks, poor compaction, voids, joints, etc., would affect the velocity of ultrasonic pulses. Such defects and variations in the concrete increase the ultrasonic transit time, and thus results in a slower velocity. Velocity in an elastic medium is related to elastic modulus as shown below:

$$V = \sqrt{\frac{E\,(1-\mu)}{\rho\,(1+\mu)(1-2\,\mu)}}$$

(11-3.1)

Also, Elastic modulus E and concrete compressive strength (f'c) are related as follows:

$$E = 57000 * \sqrt{f'c} \qquad \text{ACI 318-14 EQ. 19.2.2.1.b}$$

Where E and f'c are in psi.

Using the two equations above, and assuming $\rho = 4.5$ slugs/ft^3 and $\mu = 0.17$, one can generate the following chart:
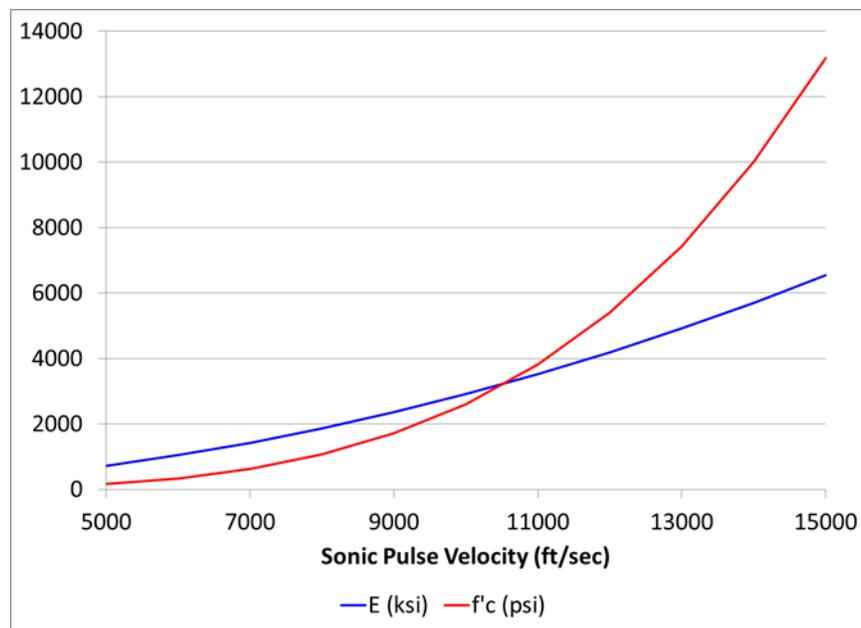

Fig. 11-3.1

Figure 11-3.1 shows the rough relationship between pulse velocity, elastic modulus, and strength. The figure is not at all precise. Actual values of f'c could vary ±50 percent or more.

However, a general trend can be seen. Concrete with velocities below 9000 ft/sec is probably poor and concrete with velocities above 11000 ft/sec is probably pretty good.

UPV testing can be used to determine relative concrete condition, identifying areas of weak concrete and strong concrete. If accurate determination of strength is required (and it often is not), velocity measurements must be calibrated with compression testing.

The UPV testing equipment consists of a transmitter and receiver transducer coupled to a signal generator and a recording device displaying transit time. The piezoelectric transducers are placed against the dam to be examined in various strategic configurations. The signal generator produces electric pulses which cause the transmitter to vibrate at its natural resonant frequency, producing sound waves that pass through the concrete, reaching the receiver, which will be detected by the recording device which will then display the transit time. The velocity is calculated from the time elapsed for the pulse to travel a predetermined length through the dam or a test specimen

The UPV works effectively, if both surfaces of the concrete dam are accessible and sound waves pass through minimum number of joints. With each pass through a joint, the wave front is dispersed and losses 50 to 70 percent of its amplitude.

Sonic Coring Tests. Sonic coring (sonic logging) tests work the same way as the UPV tests, except that the transmitter and receiver are sealed and placed in adjacent vertical core holes to check the quality and uniformity of concrete. During the tests, coring holes are filled with water to create acoustic coupling for transmission of ultrasonic pulses between transducers and the concrete. This method can be used in certain situations, such as underwater regions of the dam or when a more controlled spot check for establishing the quality of concrete is required.

11-3.3 Concrete Coring and Specimen Parameters

Concrete coring should be performed in conformance with ASTM C42. The purpose of coring is twofold. First, a random coring and testing program can be used to determine the uniformity of the concrete, and to locate problem areas. Second, once potential problem areas are discovered, coring can be concentrated in these areas to better define properties. While average values of strength and elastic modulus are of some value for structural analysis, investigations should focus on "weak links" since these problem areas are more likely to govern the safety of the dam, than the average properties.

Normally, concrete cores are extracted from the downstream face of the dam by drilling horizontally or from inside the dam galleries. When vertical drilling is done to extract samples, care should be taken to obtain samples with intact bond between construction lifts so that the strength of lift joints can be determined. The condition of the entire core should be accurately logged during drilling. The impression of an experienced engineer during a visual inspection of the extracted core is very important in ensuring that the test results are indicative of the condition of the dam.

Concrete cores extracted from different locations generally show different strength depending on the batches of concrete placed at that location. They are also influenced by the aggregate sizes within a particular specimen and the local deterioration of the mass concrete. The material

parameters from a testing program should therefore be based on the overall condition of all cores and deterioration of the dam concrete and not just on a selected "best" core samples.

11-3.4 Petrographic Examination of Concrete

Where there is evidence of concrete deterioration, a petrographic examination of concrete specimens should be carried out to ascertain the presence of any deleterious chemical actions such as alkali-aggregate reactivity (AAR). This examination should be conducted in accordance with ASTM C856, Petrographic Examination of Hardened Concrete.

11-3.5 Elastic Properties

An estimate of the elastic modulus (E) and Poisson's ratio (μ) of concrete is necessary for finite element modeling. However, the exact value of the modulus is often not critical. In most failure modes, the elastic deformations are dwarfed by sliding or overturning concerns. In addition, dynamic behavior of the dam is a function of $\sqrt{E}$, thus a factor of two error in the modulus would result in only a 41 percent error in computed natural frequencies. Poisson's ratio typically varies from 0.15 to 0.2 and has little effect on analysis results.

If accurate determination of E is required, the static modulus of elasticity (chord modulus) and Poisson's ratio should be determined in accordance with the standard test method described by ASTM C469.

11-3.6 Thermal Properties

The basic properties required for performing a thermal stress analysis include coefficient of thermal expansion, specific heat, thermal conductivity, and thermal diffusivity. Thermal analysis may not be very important. See 11-4.3 for a discussion of thermal loading.

Coefficient of Thermal Expansion. The coefficient of thermal expansion for concrete varies directly with the coefficient of thermal expansion of the aggregates, and typically the values range from 3.5 to 7 x10^{-6} in./in./°F. In the absence of measured data, an average value of 5 x10^{-6} in./in./°F may be used.

Specific Heat. Specific heat is storing heat capacity per unit temperature. Compared to a specific heat of 1.0 for water, specific heat of mass concrete typically varies between 0.20 and 0.25 Btu/lb-°F. In the absence of measured data, an average value of 0.22 Btu/lb-°F should be used.

Thermal Conductivity. Thermal conductivity is a measure of the ability of a material to direct heat flow. Typical values of thermal conductivity for mass concrete ranges from 13 to 24 Btu-in./hr-ft^2-°F.

Thermal Diffusivity. Thermal diffusivity is the rate of heat flow through a unit area divided by the product of the specific heat times the density times the gradient. For mass concrete, it varies in the range of 0.02 to 0.06 ft^2/hr. In the absence of measured data, an average value of 0.04 ft^2/hr. may be used.

11-3.7 Strengths of Concrete

1-3.7.1 Compressive Strength

The compressive strength of concrete shall be determined in accordance with ASTM 39.

11-3.7.2 Tensile Strength

While there are many methods of determining the tensile strength of concrete, this parameter has little significance in the performance of an arch dam. Core samples can be obtained and tested in a variety of ways, but the tensile strength of an arch dam is usually limited by the ability of horizontal lift joints, vertical contraction joints, and pre-existing cracks to resist tension. For this reason, the accurate determination of the tensile strength of the intact concrete is typically not necessary.
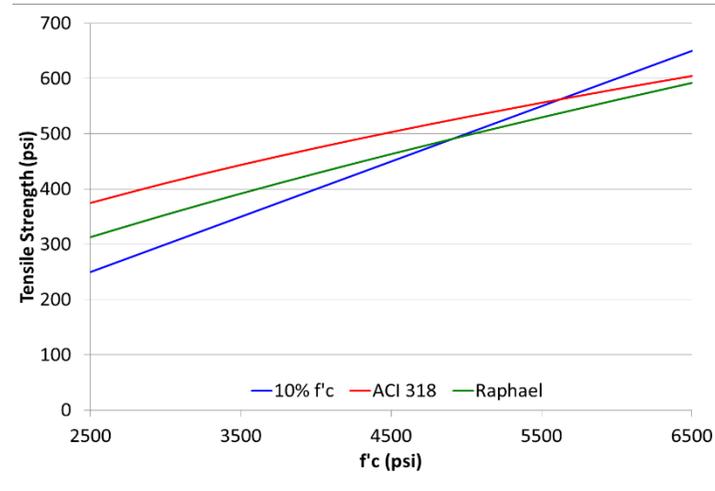
Fig. 11-3.2

It is recognized that principal axis tension may exist. Reasonable estimates of tensile strength as a function of f'c include:

$f_t = 10\%\ f'c$
$f_t = 7.5*(f'c)^{1/2}$ ACI 318
$f_t = 1.7*(f'c)^{2/3}$ Raphael (1984)

Since this measure of tensile strength has been developed without regard for any specific weakness in the mass concrete, such as the lift joints, and because the tensile strength across such joints may be much less than in the homogenous material, it would be judicious to assume the tensile strength for the lift joints is less than that for the homogenous concrete. In fact, the actual tensile strength across the poorly constructed lift joints of some older dams could be even drastically lower than that for the homogeneous concrete.

If a failure mode is contingent upon high tensile strength, there is very likely a problem.

11-3.7.3 Shear Strength

Although arch dams are designed to resist load by compressive arch stresses, shear stress can be a problem on certain planes within the dam, especially near the foundation. The simplest criterion for failure for concrete under multiaxial stresses is based on the Mohr-Coulomb theory. The Mohr-Coulomb diagram shown in Figure 11-3.3 represents a procedure for determining the failure under combined stress states from which an estimate of the shear strength can be obtained. In this figure, the point at which the failure envelope intersects the vertical axis represents the strength of concrete in pure shear. Using this method the shear strength of the

concrete has been found to be approximately 16 percent of the uniaxial compressive strength. It must be remembered that lift joint strength may be significantly less than intact concrete.
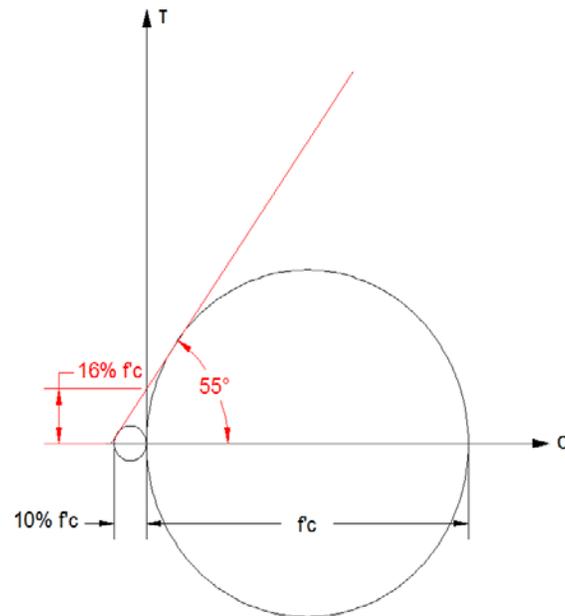
Fig. 11-3.3

11-3.8 Dynamic Material Properties

During earthquake excitation, the rate of loading is much greater than in a short-term compression test. The strains in a typical concrete dam earthquake response are developed at frequencies of 2.5 to 25 Hz, which corresponds to times from zero to peak load of 10 to 100 milliseconds. Tests performed at such rapid rates of loading demonstrate that the dynamic modulus of elasticity is about 25 percent greater than that observed in short term tests, and this increased modulus should be used in the dynamic response analyses. Tests performed at loading rates typical of earthquake response, such as those mentioned above with regard to the dynamic modulus of elasticity, have shown that on average tensile strength is increased by about 50 percent at these high strain rates. If a failure mode is highly dependent on these properties, this may be of some importance.

11-4 LOADING

Loads can be categorized into two basic types; static and dynamic. Static loads are sustained loads that do not change, or change slowly compared to the natural periods of vibration of the structure. Static loads can be further divided into follower and non-follower loads. Follower loads are loads that do not change due to the dam's deflection. Examples of these are gravity and hydraulic pressure. Because follower loads can follow the dam's deflection, they have the ability to do work. Non-follower loads are loads that are relieved by dam deflection and therefore cannot do work. Examples of these are thermal or AAR expansion, and loads due to thermal expansion of ice.

Dynamic loads are transitory in nature. They are typically seconds or less in duration. Because of the speed at which they act, the inertial characteristics of the dam as well as its stiffness affect the dam's behavior. Examples of dynamic loads include earthquake-induced forces, blast-induced forces, fluttering nappe forces, or forces caused by the impact of ice, debris, or boats. Because of their short duration, and in the case of earthquake constant reversals, they cannot do work.

Failure takes work. In order for a dam to fail, very big heavy objects have to be moved over a distance. For this reason, non-follower loads and dynamic loads cannot cause failure by themselves. What they can do is cause damage. If the damage caused is such that the dam can no longer resist the follower loads, then failure can occur.

This kind of progression is depicted adjacent. The event tree may be something like described below:

1) Severe seismic shaking causes opening of vertical contraction joints and a set of large cracks near the foundation approximately parallel to it.
2) Misalignment of cantilevers is such that arch action is no longer present over large areas of the dam.
3) In damaged state, static reservoir loads produce enough movement of now free cantilevers that the dam fails.
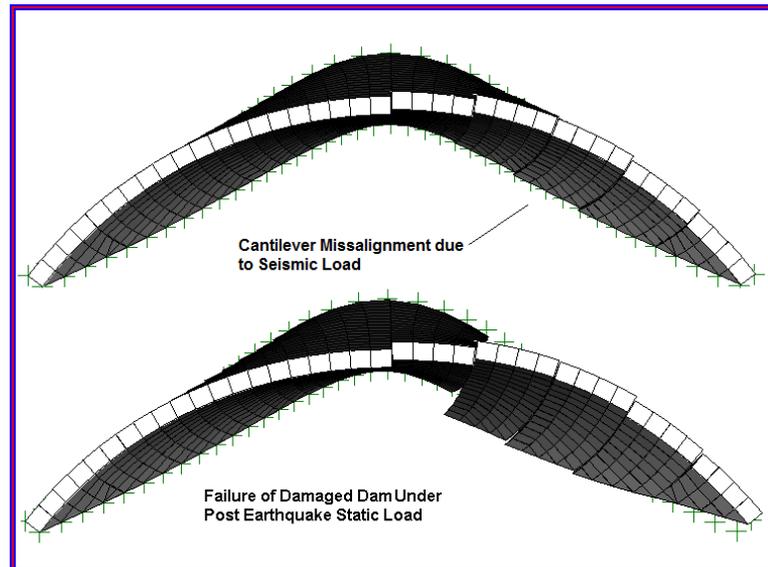
Fig. 11-4.1

Arch dams are subject to the same loads as any other type of dam. There are certain loads however that are more likely to adversely affect an arch dam. The loads listed in the following sections may require special consideration.

11-4.1 Hydrodynamic Excitation

In rare instances arch dams with crest overflow spillways can be subject to forces produced by a "fluttering nappe". Nappe flutter is caused by resonance between air trapped in the cavity between the nappe and the downstream face of the dam. Vibrations induced by such a fluttering nappe could be of importance to the safety of tall and thin arch dams. Because the trapped air between the nappe and the dam is critical to the feedback of this vibration, the potential for nappe flutter can be eliminated by insuring that the air behind the nappe is not trapped. This can be achieved with flow splitters.

11-4.2 Ice Load

Ice can produce significant loads against the face of an arch dam. For this reason, ice load must be considered where reservoir freezing can be expected. Ice loads can be categorized into two different types; static loads, produced by the ice in contact with the dam when the reservoir is completely frozen, and dynamic loads, caused by the impact of large floating sheets of ice colliding with the dam.

Static ice load is caused by the thermal expansion of the ice or by the wind and current drag. Pressures generated by the thermal expansion depend on the temperature rise and the ice properties. Wind drag depends on properties of the exposed surface and on the direction and velocity of the wind.

The magnitude of ice loading depends on the thickness of the ice cover. When actual measurements of ice pressure are not available, ice loading may be taken as 5 kips per square foot along the contact surface with the dam. For example, a 2-foot thick layer of ice would apply a 10 kip per linear foot load along the axis of the dam.

The radial distribution of ice pressure is of some concern, especially for thin arch dams. Arch dam design assumes that loads will be radially uniform. If this is not the case, large bending stress in the arch direction could result. Radial variation of the ice load could be caused by un-even heating, differences in thickness, or the absence of ice over part of the arch due to powerhouse intakes. In addition to the possibility of non-uniform loading, there is the fact that the ice itself interacts structurally with the dam, complicating the determination of the arch's response. The applied ice load must be representative of the site specific conditions.

Another possible source of ice loading is ice impact. In many northern rivers, large ice sheets, sometimes weighing many tons, can float down river under the influence of high spring discharges. The force of these impacts can be roughly calculated by equating the kinetic energy of the moving ice sheet and the energy dissipated in crushing ice against the object that it impacts. Refer to the U.S. Army Corps of Engineers EM-1110-2-1612 "Ice Engineering" for additional guidance.

11-4.3 Thermal Loading

Temperature changes can produce large stresses in dams. Thermal cracking will almost certainly happen at the dam/foundation interface. In addition, vertical joints will open and close in response to yearly temperature changes. While the stresses produced by thermal loading can be quite high, they are not follower forces. As soon as cracking or shifting occurs, thermal stress is relieved. **It is often more expeditious to assume cracking and proceed with non-linear analysis than to try to prove that thermal stresses will not induce cracking.**

The figure below shows the contrast between an un-cracked dam under thermal loading and a dam where thermal strains are accommodated through base cracking and vertical joint opening. Note that in the latter case, thermal tensile stresses all but disappear.
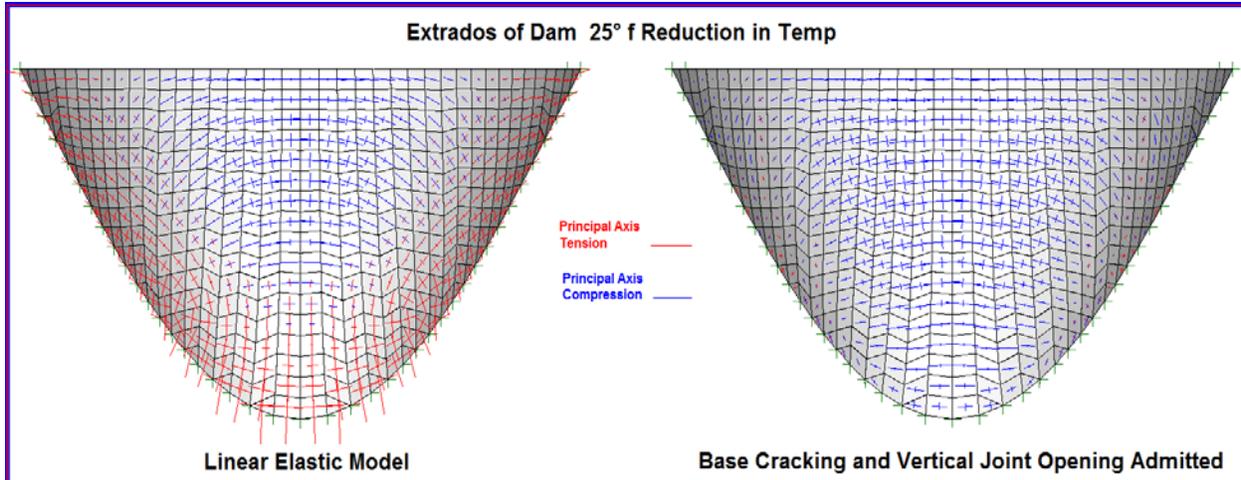
Fig. 11-4.2

Because forces resulting from temperature loading are not follower forces, they cannot drive a failure mechanism. Failure mechanisms require movement and as soon as movement occurs, thermal stresses are relieved. What thermal stress can do is damage. They can cause cracking, which may weaken the dam and reduce its ability to resist other loads.

A failure mode sequence involving thermal loading might look like the event tree described below.

1) Thin arch dam relies on massive thrust block for stability.
2) Summer thermal loading causes the arch to expand at a greater rate than the thrust block.
3) The differential expansion results in the arch applying an upward force to the thrust block.
4) The upward force initiates base cracking in the thrust block.
5) Base cracking subjects the thrust block to greater uplift force.
6) Increased uplift plus increased horizontal force due to arch expansion destabilizes thrust block.
7) Thrust block moves enough to deny the arch support.
8) Dam fails.

Note here that it is hydrostatic loading that fails the dam, however the thermally induced cracking made it possible.

Thermal analyses like all other analyses should be done in the context of a failure mode. What has often happened in the past is that a general stress analysis was done, including thermal loading. The stress results were then compared to allowable stress acceptance criteria. Since there was a great desire to show that stresses were within acceptance criteria, and since thermal loading was often the largest contributor to stress, the importance of thermal analysis was over emphasized. In the absence of a clearly defined failure mode these analyses were not helpful and were misleading. Often fictitious high tensile stresses were indicated, especially in the case of linear models. In the absence of a failure mode, these stresses were meaningless.

More guidance on thermal loading can be found in "Arch Dam Design", EM-1110-2-2201 USACE, May 1994.

11-4.4 Loading Due to Expansive Concrete (AAR)

Alkali-Aggregate Reactivity (AAR), also known as alkali-silica reactivity (ASR) or alkali-carbonate reactivity (ACR), has been found in a large number of concrete dams and hydroelectric plants around the world. The reaction occurs between certain aggregates and alkalis in the cement, leading to the formation of gels, which then absorb water and expand, causing increased stress, cracking of the concrete, and structural deformations. Three basic requirements for expansive AAR to occur are: 1) presence of deleteriously reactive aggregates, 2) sufficient concentration of alkali, and 3) adequate levels of moisture in the concrete.

FERC's experience with several dams under our jurisdiction has shown that the chemical reaction and resulting swell can continue for decades, maybe even indefinitely. The rate of swell is a function of confining stress. Growth slows to zero when the strain energy resulting from increased swell becomes greater than the chemical energy derived from the reaction. (Charlwood et al. 1992) An example of this stress dependence is depicted in Figure 11.4.3. Actual values are site specific.

AAR swell is somewhat similar to thermal loading. It can cause cracking and high stress. It differs from thermal loading in the sense that it does not reverse itself.
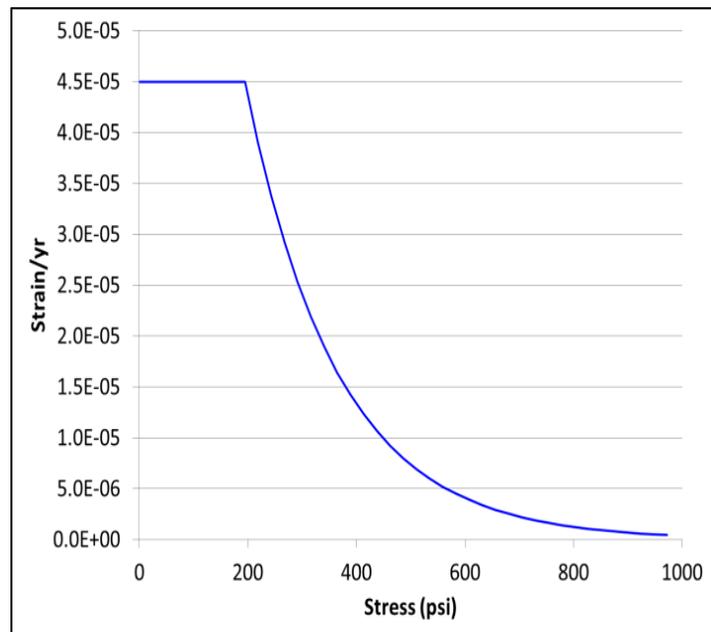
Fig. 11-4.3

As with all other loading, the main concern with AAR is whether or not it can produce a failure mechanism. It is not a follower force and so it cannot produce failure without the help of gravity and hydraulic loading.

Figure 11-4.4 shows the effect of AAR swell on dam stress as well as on the status of the dam/foundation contact. AAR effects produce a significant peak compressive stress increase, from 467 psi to 1501 psi, but this in itself is not necessarily problematic. What is of potential importance is the direction of the principal stresses. Note that in the no swell case, the principal stress vectors dive into the abutments approximately perpendicular to them. In the swell case, the principal stresses have a clear upward trajectory as they enter the abutments. This may cause up abutment sliding. If this occurs, the frictional strength of the dam/foundation contact could be exceeded and reduced to residual values. A potential failure mechanism is described as the following:

1) AAR swell causes an increase in shear stress at the dam/foundation contact.

2) Shear failure occurs resulting in up abutment sliding, resulting in residual shear strength on the dam/foundation contact.

3) Movement along dam/foundation contact opens pathways for additional uplift.

4) The combination of reduced shear strength and higher uplift on the dam foundation contact results in dam failure.

In addition to the changes to the stress state on the dam foundation contact, AAR can change the magnitude and direction of dam thrust applied to rock blocks in the abutment or thrust blocks (see Figure 11-4.5). This also could have failure mode implications.

Fig. 11-4.4

Fig. 11-4.5

11-4.5 Earthquake Loading

The purpose of the consideration of earthquake loading is to determine whether or not damage will be significant enough to compromise the dam's ability to resist the static, post-earthquake forces. What is of interest is not peak stress, but rather induced offsets and cracking. If it can be shown that with reasonably conservative assumptions with respect to earthquake induced

damage, the post-earthquake static loads can be resisted, then earthquake loading need not be directly considered.

For example, suppose the failure mode described below is being investigated:

1) Cross valley seismic loading causes bending moments in excess of the flexural capacity of a gate pier.
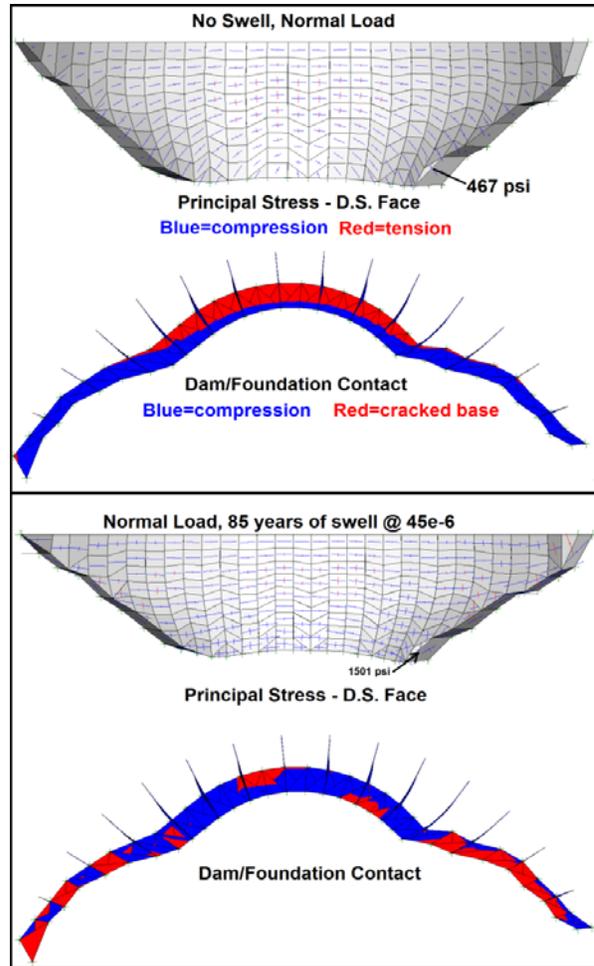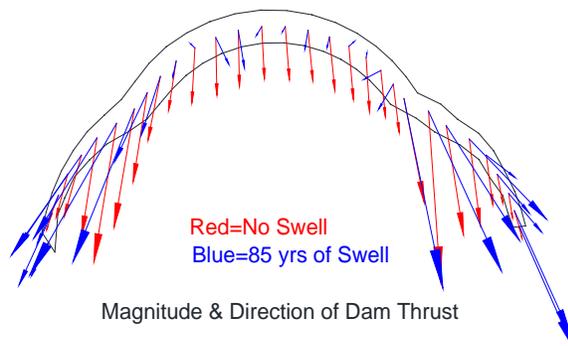2) Pier reinforcing steel yields.
3) Pier begins to rock back and forth in the cross valley direction.
4) Reinforcing steel ruptures.
5) Without reinforcing, pier cannot resist static gate load. Pier slides downstream, releasing a portion of the reservoir.

The plausibility of each event listed above can be evaluated. For example, a 3D, linear elastic, dynamic finite element analysis could be done to evaluate the plausibility of Event 1. This would probably involve modeling the entire dam and not just the pier in question because the dam will very likely amplify the ground motions due to its own structural response. If analysis shows that moment capacity is indeed exceeded, Events 2, 3, and 4 could be investigated with 3D non-linear dynamic analysis.

However, is also possible to evaluate this failure mechanism by analyzing the plausibility of Event 5. This could be done relatively simply with a 2D static stability analysis. A crack plane at the base of the pier could simply be assumed, and the effect of the reinforcing steel could be reduced based on the amount of anticipated damage.

Using the logic presented above, it is often possible to evaluate the effects of earthquake loading without sophisticated dynamic modeling. When possible, this means of dealing with earthquake loading should be used.

In cases where it is decided that the behavior of the structure in the midst of the earthquake is of consequence, dynamic analysis must account for the actual features of the structure.

11-4.5.1 Earthquake Response Spectrum

If it is determined that dynamic analysis is required, response spectra should be developed for both horizontal and vertical ground motions. Spectra should be developed consistent with the Guidelines contained in Chapter 13. The spectra should be developed for 5 percent damping. The evaluation of most dynamic failure modes will require a time history analysis because non-linear effects will have to be taken into account. Therefore, the response spectrum will typically not be used in analysis. However, the response spectrum should still be generated for the purposes of selecting the appropriate time history records.

11-4.5.2 Time History Earthquake Input

Time histories of ground motions should be developed consistent with the guidelines contained in Chapter 13. They should be developed for three components of motion (two horizontal and one vertical). Time histories may be either (a) recorded or simulated-recorded time histories or

(b) response spectrum matched time histories as described in Chapter 13. Typically a minimum of three sets of ground motion records will be required.

11-5 ANALYSIS TECHNIQUES

11-5.1 Overview

As stated in Section 11-1.4.2, the method of analysis must address the failure mode of concern. There is not one right way to evaluate the plausibility of a failure mode. In addition, analysis tools are constantly evolving. The following discussion should not be seen to require the analyses that it describes.

11-5.2 Finite Element Analysis

The finite element procedure is the numerical method most often used for the structural analysis of arch dams. This guideline assumes that the reader is already familiar with the general theory of finite element analysis of elastic solids (Zienkiewics, 1971; Bathe and Wilson, 1976). The following remarks are intended only to point out some special considerations in the application of this technique to arch dam analysis.

11-5.2.1 Structural Modeling Considerations

The finite element analysis of arch dams is based on the same assumptions that underlie all finite element analyses. This being the case, the basic principles that govern element formulation, mesh construction, and load application are as valid in the analysis of arch dams as they are anywhere in structural mechanics. There are, however, certain special with respect to arch dam analysis:

1) As in the case of gravity dam analysis, the dam/foundation interface shall be assumed to be incapable of resisting tension normal to it. Analyses that assume that the dam is "welded" to the foundation are **not** acceptable. This usually requires the use of a gap/friction contact at the dam/ foundation contact.
2) Uplift forces acting on potential failure surfaces cannot be ignored.
3) The effect of vertical contraction joints and preexisting cracks have to be taken into account. This does not mean that every crack has to be included in the model. Consider the principle stress plot of the cracked dam shown in Figure 11-5.1. The diagonal crack and the vertical contraction joint are not included in the finite element model. However, they are in regions of compressive stress which will tend to keep these cracks closed, and if shear stress on the crack surface is within the friction cone (Figure 11-2.9), the crack will not affect the behavior of the dam and therefore need not be included in the model.
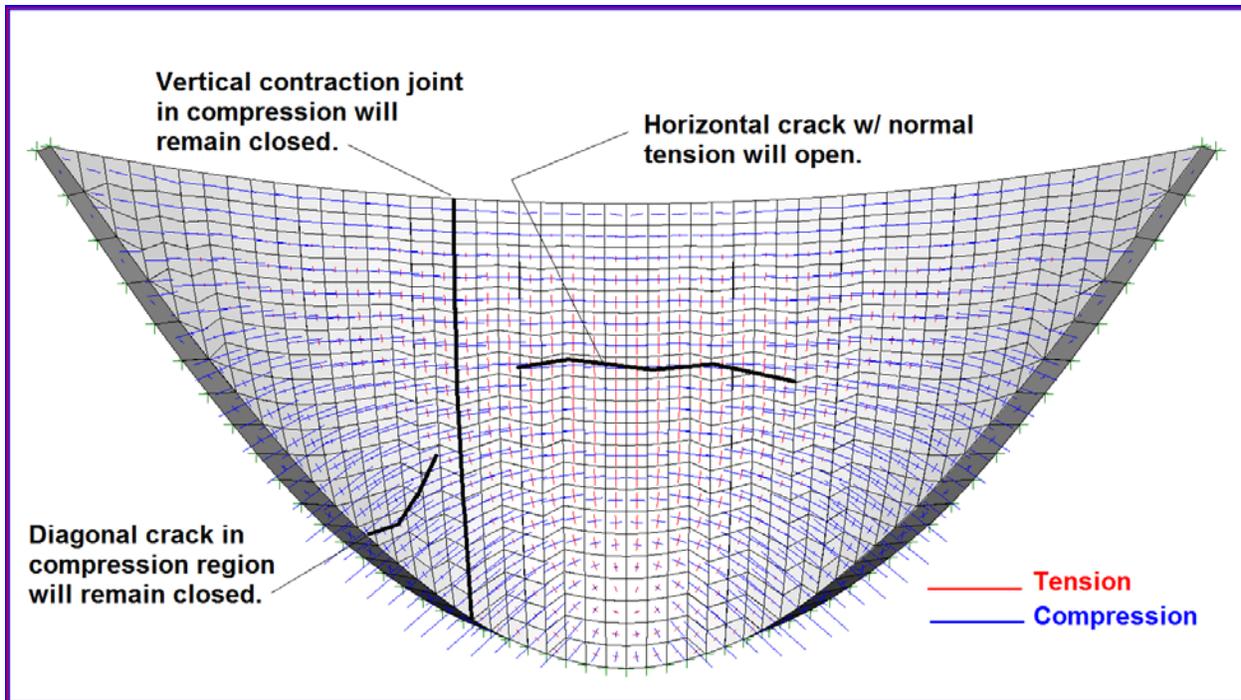
Fig. 11-5.1

The horizontal crack on the other hand is oriented in such a way that tensile stress is applied normal to it. In this situation the crack cannot be ignored; it must be included in the model.

4) Mesh density is a function of the purpose of the model. If stress concentration at openings or corners is to be captured, the mesh must be very fine. However, if global sliding and rocking are the concern, the mesh can be quite coarse.

Consider the two models depicted adjacent. An initial 5° tilt is imposed on a pier, and then the pier is allowed to wobble back and forth. The pier in this example is 50 ft. high, 10 ft. wide and has typical concrete elastic properties.

Figure 11-5.2 shows a plot of top horizontal deflection. Note that the dynamic rocking behavior is not identical but quite similar for the fine and coarse mesh models.

Coarse   Fine
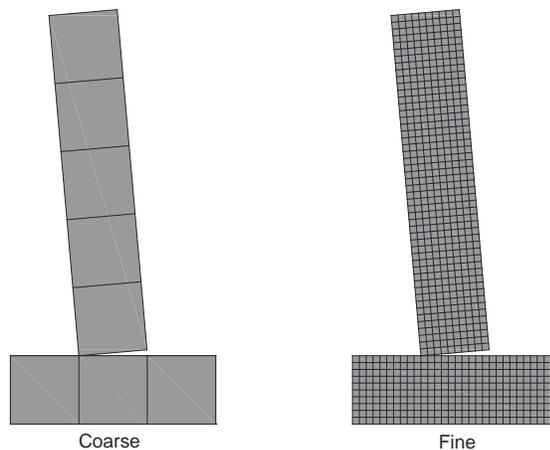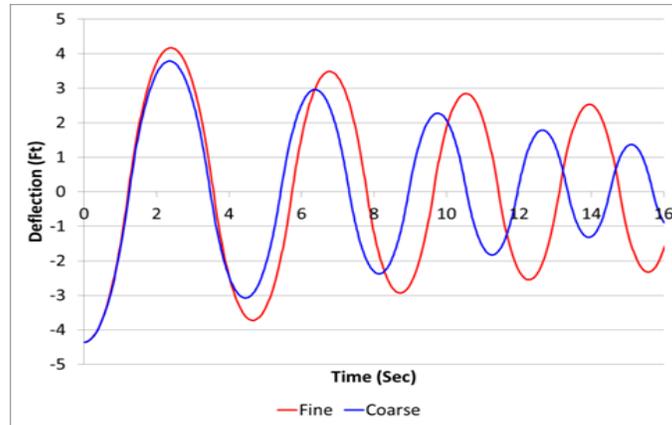
Fig. 11-5.2

5) Hydrodynamic coupling with the reservoir has a big effect in the dynamic behavior of the dam. Arch dams tend to be thin. This means the mass of concrete that is accelerated in dynamic loading is less than the mass of concrete accelerated in a gravity dam. The accelerated water is therefore likely to be a bigger portion of the total system mass. Figure 11-5.3 shows the flow field associated with the Westergaard added mass theory. The two dams depicted are of equal height and are subjected to the same rigid body unit acceleration. Note the difference in portion of total system mass accounted for by the reservoir.
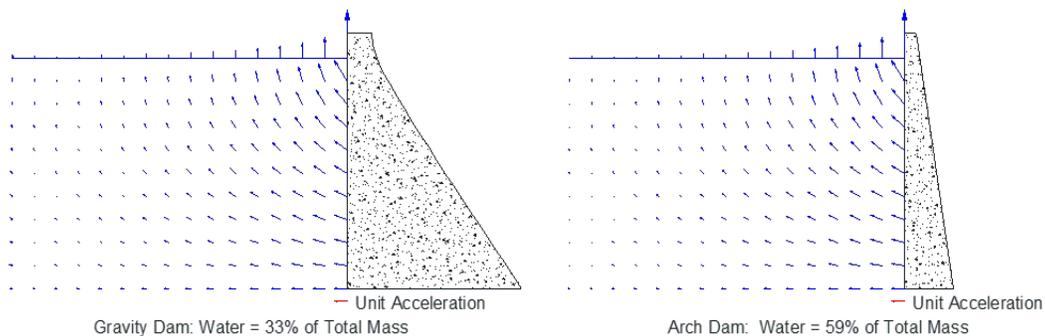
Fig. 11-5.3

Because of this, it is more important to account for hydrodynamic effects in the seismic analysis of an arch dam than it is in other types of dams.

The reservoir may be modeled directly using finite elements with zero shear strength, but this often results in numerical instability because elements with no shear strength admit zero energy displacements. Nodal displacements for the water elements can be huge, and while physically meaningless, they can cause elements to effectively turn themselves inside out.

Acoustic elements especially formulated to hydrodynamic modeling exist but are currently not in wide use.

The use of Westergaard added mass theory is acceptable. It is understood that the Westergaard pressure distribution was derived from a rigid body displacement of a vertical 2-dimensional upstream face. This being the case, it is not compatible with the modes of vibration, nor does it rigorously address the 3D nature of an arch dam.

Westergaard theory is described below:

$$M_{added} = \rho * \sum_{i=1,3,5..}^{\infty} \left(\frac{8H}{(i\pi)^2}\right) \sin\left(\frac{i\pi y}{2H}\right)$$

Where:

ρ is the mass density of water
H is the reservoir depth
Y is the distance below the water surface
M_{added} is the distributed added mass
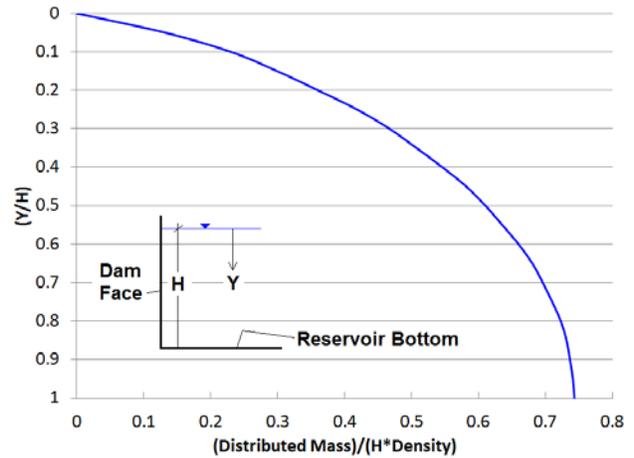
In the following example the Westergaard theory is compared to a more rigorous hydrodynamic solution. A 50 ft. high pier surrounded by water is considered. The pier is assumed to be fixed to its foundation and to behave elastically. The rigorous model shown in Figure 22-5.4 has water modeled directly using zero shear strength elements. A small displacement element formulation is used so that the water elements do not distort to the point of numerical instability. Surface wave propagation is enabled by springs attached to the water surface nodes. These springs have a stiffness equal to the unit weight of water times the nodal tributary length. The Westergaard model consists of nothing but the pier with nodal masses increased as per Westergaard theory.

The dynamic input to both models is depicted in Figure 11-5.5. The velocity input corresponds to a 1 g, 2 Hz acceleration, and 0.5 second duration.
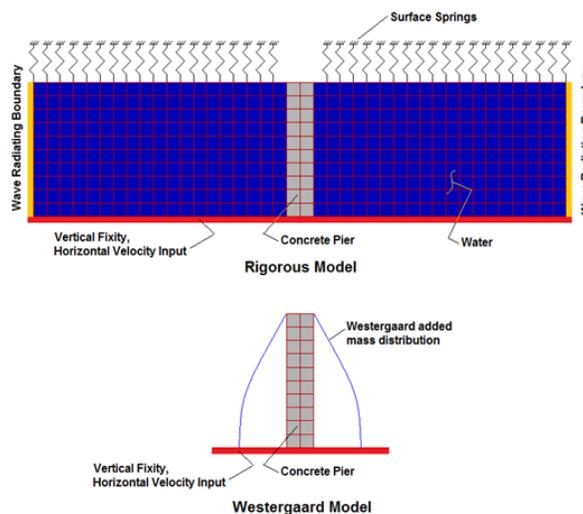
Fig. 11-5.4
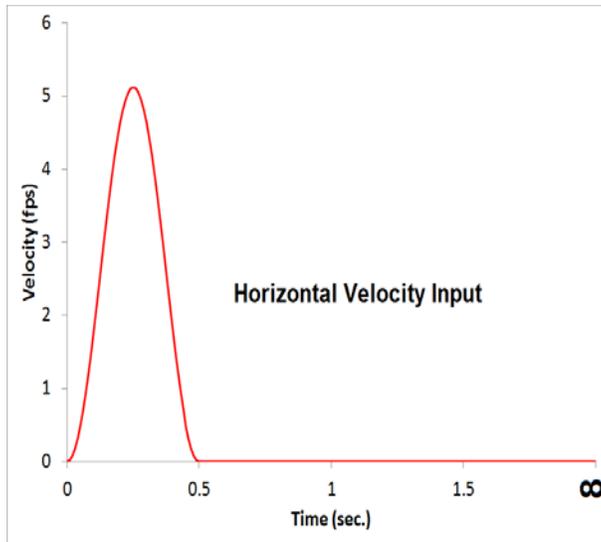
Fig. 11-5.5

Figure 11-5.6 depicts the resulting base moments. Note that there is very little difference between the rigorous model and the Westergaard model.

Any dynamic model of an arch dam must admit the failure mode of interest. This typically means that the model will have gap friction elements to include the effects of vertical contraction joints, horizontal cracks, the dam/foundation interface, and possible failure surfaces within the rock abutments. The hydrodynamic coupling solution must be compatible with gap friction elements, i.e. it must admit differential displacements over zero distance.
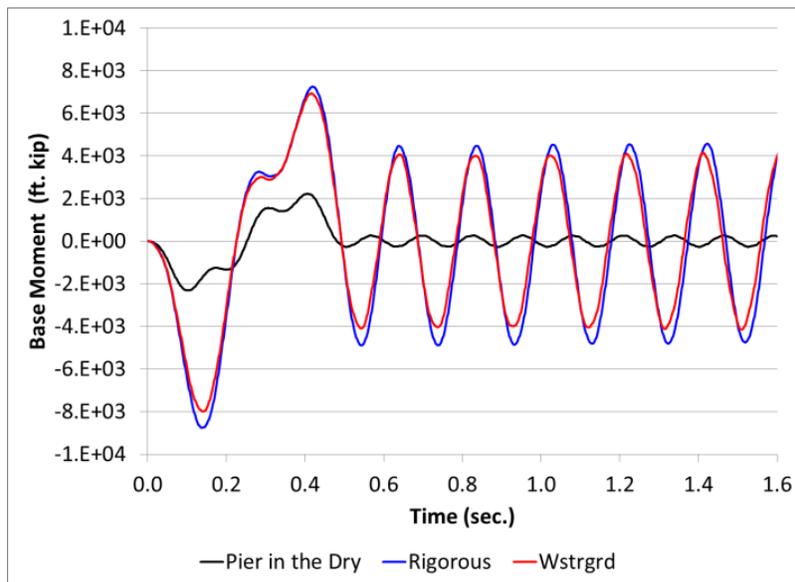
Fig. 11-5.1

The Westergaard theory, while crude, does not have a problem accommodating non-linear behavior associated with gap friction elements.

11-41

11-6 INSTRUMENTATION

A complete discussion of the types of instruments typically used at dams is contained in Chapter 9. The following paragraphs are intended to help staff understand the special instrumentation considerations for arch dams.

11-6.1 Movement Monitoring

Surveys

Movement of the dam, especially at the crest, can be measured by survey. Fixed targets can be attached to the dam at desired locations and a total station laser survey instrument can be set up at stationary locations away from the dam. Using triangulation, movement of a point on the dam can measured. Survey measurements can be challenging at arch dams since there may not be accessible positions away from the dam that can serve as benchmarks. There have been instances where a stationary benchmark position away from the dam turned out to not be stationary. It is also true that usually the survey is trying to pick up changes in distances of a fraction of an inch at a distance of several hundred if not thousands of feet.

Extensometers

Extensometers are rods, typically made of metal, which are anchored into deep stationary rock at the bottom of a bore hole. The rod then extends to the top of the borehole. If there is relative movement in the rock mass or concrete between the top and bottom of the rod, in a direction parallel to the rod, this movement can measured. It will show up as a change in position between the top end of the rod and a gage on the extensometer head (see Figure 11-6.1).

The extensometer's ability to read movement in contingent upon the angle α. What the extensometer actually reads is the real movement δ times the cosine of α, where α is the angle between the direction of movement and the axis of the extensometer.
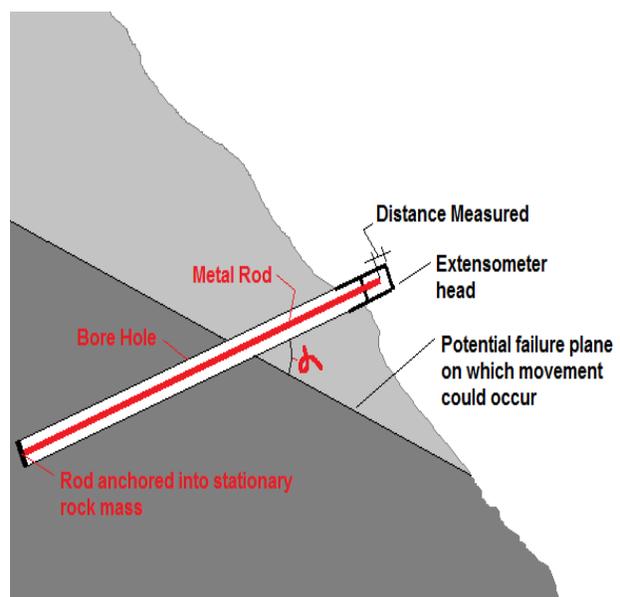
Fig. 11-6.1

Often the direction of movement is not known. This problem can be overcome by the use of multiple extensometers (see Figure 11-6.2). If e1 and e2 are the readings from extensometers E1 and E2 then:

$$e1 = \cos(\alpha) * \delta X + \sin(\alpha) * \delta Z$$

$$e2 = \cos(\text{ß}) * \delta X + \sin(\text{ß}) * \delta Z$$

This 2D relationship between measured extension and relative movement can be inverted as follows:

Fig. 11-6.2

$$D = \cos(\alpha) * \sin(\text{ß}) - \cos(\text{ß}) * \sin(\alpha)$$

$$\delta X = \frac{(e1 * \sin(\text{ß}) - e2 * \sin(\alpha))}{D}$$
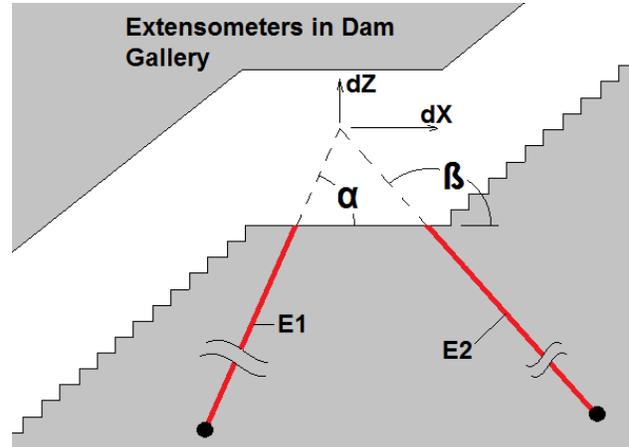
$$\delta Z = \frac{(-e1 * \cos(\text{ß}) + e2 * \cos(\alpha))}{D}$$

In the above example, the plane which E1 and E2 lie in is considered vertical, and therefore relative motion in and out of the page would not be detected. Using similar logic, a 3D solution can also be derived so that 3-axis motion can be measured using three extensometers.

Extensometers are subject to thermal error. The elongation and contraction of the extensometer rod due to temperature change is sometimes greater than the deflections that one is trying to measure. Some extensometer sets come with thermistors attached to the rod so that the temperature of the rod can be known and the associated expansion and contraction can be corrected.

Plumb Lines

Plumb lines are a very good direct measurement tool for horizontal deflection. They require no mathematics or triangulation, they are not temperature sensitive, and they can have very high precision. The typical arrangement is shown adjacent. Note that the horizontal offset between points A and B is directly indicated (see adjacent figure).
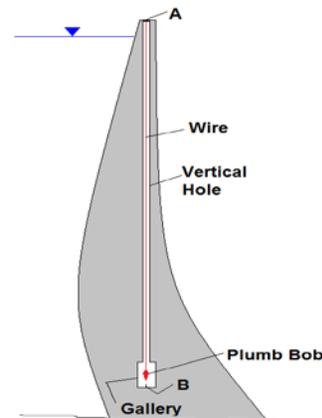
Inverted Plumb Lines

Inverted plumb lines can be used when the bottom point is not accessible. A ring float floating in a fluid (typically water and antifreeze) in an annular tub tensions the plumb line from the top. The float remains over the bottom attachment point of the plumb line so relative horizontal

movement between the bottom attachment point and the annular tub can be read directly (see figure below).
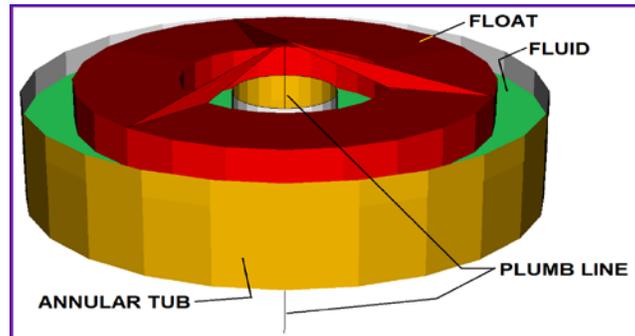
Inclinometers

Inclinometers work by sensing the tilt of a probe as it is raised up a vertical hole. The tilt is the first derivative of horizontal displacement with respect to vertical position, so the measured tilt can be integrated to yield displacement (see adjacent figure). Inclinometers have the advantage of being able to not just measure total relative displacement between two points, but also where in the vertical alignment offsets are located.
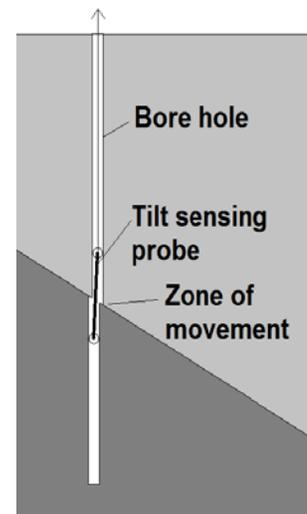
Figure 11-6.3 shows inclinometer data as it varies with time. The initial borehole which in this case was drilled in October of 2000, was relatively vertical. Note that in April of 2001 a clear movement occurs at about elevation 106. The movement grows with time. This is indicative of a failure surface which intersects the inclinometer borehole at this elevation.

Fig. 11-6.3

11-44
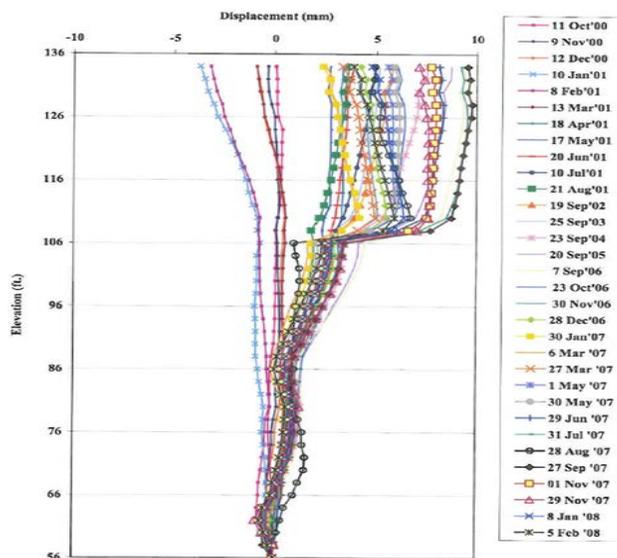
11-6.2 Hydrostatic Pressure Monitoring

As was observed in the abutment wedge example of the Foundation Considerations, Section 11-2, hydrostatic pressure can have a big effect on the stability of abutment rock wedges. Any failure mechanism that involves sliding on a failure surface is affected by hydrostatic pressure acting on that failure surface.

The Malpasset dam failure (France 1959) was largely the result of uplift pressure in the left abutment that had not been anticipated.

The typical devices for measurement of hydrostatic pressure are appropriate for the evaluation of these types of failure modes.

11-6.3 Flow Monitoring

Monitoring of leakage, gallery drain flow, etc. is often done at arch dams. Changes is flow can be an indicator of a failure mode developing.

11-7 HISTORIC DAM INCIDENTS

11-7.1 Overview

There is no comprehensive listing of arch-dam failures. However, available listings are contained in more than one publication. Babb and Mermel (1968) listed 600 dam incidents (including failures) of which only seven involved arch dams, two involved multiple arch dams, and two involved gravity-arch dams. The dams they list are as follows: Matilija (U.S.A., 1965); Vajont (Italy, 1963); Malpasset (France, 1959); Moyie River (U.S.A., 1938); Alla Sella Zerbino; Allessandria (Italy, 1935); Lake Lanier (U.S.A., 1926); Gleno (Italy, 1923); Lake Hodges (U.S.A., 1918); Manitou (U.S.A., 1917); and Tolla (France, 1892).

The International Commission on Large Dams (ICOLD) Bulletin 99 (1995) lists seven arch dam failures, three of which are also listed by Babb and Mermel (Malpasset, Gleno, and Moyie River). The other four arch dam failures listed by ICOLD are: Leguaseca (Spain, 1987), Meihua also called Plum (China, 1981), Idbar (Yugoslavia, 1960); and Vaughn Creek (U.S.A., 1926).

In addition, in a paper entitled "Lesson from Serious Incidents at Seven Arch Dams" presented at the 1997 annual conference of the Association of State Dam Safety Officials, G.S. Sarkaria described incidents at Le Gage, El Fryle, Koelenbrein, and Zeuzier dams. Following is a summary of the historical incidents and failures involving arch dams:

Matilija, California. The concrete dam was completed in 1949 and was a combination of gravity and arch structure. It was 163 feet high with a crest length of 620 feet. In 1965, the dam was judged to be unsafe as a result of deterioration of the concrete due to expansive aggregate. Foundation conditions were also judged to be poor. The reservoir was drained, the dam was eventually demolished, and the site was submerged by a new dam downstream.

Vajont, Italy. This thin-arch concrete dam, which is 905 feet high, was overtopped by a huge landslide-generated wave. Inflow to the reservoir was normal at the time. The resulting

overtopping was estimated to be as much as 300 feet. The dam itself suffered little damage, but the reservoir was a total loss. The resulting flood caused great loss of life in the downstream areas. A detailed description of failure of Vajont Dam is provided in Section 11-7.2.1.

Malpasset, France This thin-arch concrete dam, which was 218 feet tall, failed due to a movement of the left abutment in December 1959. The movement was thought to be due to sliding on a rock wedge formed by intersection of a fault with gneissic foliation in the rock of the left abutment. The principle cause of the failure was not directly due to the passage of a flood in that the dam was never overtopped. However, a very large flood was being passed when the failure occurred. The official death toll was 396 people killed in the ensuing flood, which suddenly struck the village of Frejus. The dam was a complete loss and is further discussed in Section 11-7.3.

Le Gage, France This very thin 150 feet high arch dam developed extensive cracking on both faces of the dam after first filling of the reservoir in 1955. Cracking continued to worsen for the next 6 years. After the failure of Malpasset dam, Le Gage was abandon and a new thicker arch dam was constructed upstream.

El Fryle Dam, Peru This 200 feet high arch dam experienced a major slide on one of the abutments during filling. The dam did not collapse. A concrete thrust block abutment was constructed and the dam was saved.

Moyie River, Idaho This 53-foot high concrete arch dam, located on the Moyie River, was approximately 64 feet thick at the base and 24 feet wide at the crest. During passage of a major flood in 1926, the spillway, which was located on one abutment, was undermined. The erosion completely washed out one of the abutments. The abutment was replaced and the dam is still in use.

Alla Sella Zerbino, Allessandria, Italy This concrete arch-gravity structure was only 39 feet high with a crest length of 262 feet and a reservoir capacity of 14,000 acre-ft. It failed on August 13, 1935, as a result of overtopping and sliding on its foundation. One hundred lives were lost.

Lake Lanier, North Carolina This constant-radius concrete arch dam was constructed in 1925. It had a thickness of 12-1/2 feet at the base and 1 foot at the top. It was 62 feet high with a crest length of 236 feet. One of the abutments (cyclopean masonry) washed out as a result of the failure of soft rock in the abutment on January 21, 1926. The remainder of the dam was unharmed.

Manitou, Colorado This concrete arch dam was 50 feet tall with a crest length of 300 feet. A portion of the dam failed in 1924 due to deterioration of the concrete.

Tolla, France This very thin arch dam was 295 feet high with a crest length of 435 feet. Owned by Electricite DeFrance, the dam experienced severe cracking. It was buttressed in response. Cracking may have been the result of large temperature stresses.

Koelnbrein, Austria Cracks and substantial leakage appeared in the lowest foundation gallery when the reservoir was 80 percent full two years after first filling. Full uplift pressure was

observed over the entire base in the central portion of the dam. Major repair was undertaken between 1989 and 1994.

Zeuzier, Switzerland The dam behaved satisfactorily for 20 years, then began to deflect upstream due to riverward movement of the left abutment.

Meihua (Plum), China This experimental masonry arch dam was 72 feet high and had a crest length of 211 feet. It was completed in 1981 held a reservoir of only 93 acre-ft. It failed shortly after filling in 1981. The dam failed as a result of structural failure due to excessive uplift movement along a peripheral joint as described in Section 11-7.3.2. The scheme was abandoned after failure.

Idbar, Yugoslavia This concrete arch dam was 125 feet high with a crest length of 354 feet. It was completed in 1959 and failed in 1960. Failure was during first filling and resulted from piping and erosion of the foundation.

Vaughn Creek, USA This concrete arch dam was 62 feet high with a crest length of 312 feet. The dam was completed in 1926 and failed during first filling. Seepage and poor materials in the dam caused failure.

The above incidents indicate that safety of an arch dam can be threatened by overtopping due to major floods and landslides, abutment sliding, erosion of foundation-abutment rock, and the deterioration or poor construction materials.

11-7.2 Landslide Case

The Vajont Dam, constructed between 1957 and 1960 is located on the Vajont River in northern Italy near the towns of Longarone, Pirago, Casso and Erto. The dam is a 276 meter (905 ft.) high, double curvature, thin arch dam. On 9 October 1963 during reservoir filling a catastrophic landslide movement occurred suddenly over a 2 km (1.2 mile) reach of the southern or left bank of the reservoir. According to Muller (1987) the slide mass consisted of a volume of 275 million cubic meters (360 million cubic yards), which generated a wave 260 meters (853 feet) high. Hendron and Patton (1985) describe a wave which crested 100 meters (328 feet) above the top of the dam and had a height of 70 meters (230 feet) downstream at the confluence of the Vajont and Piave Rivers. More than 2,000 people lost their lives in this catastrophe. Longarone and Pirago were the towns most severely affected. The dam structure itself survived the overtopping by the wave of water and the impact of the load of earth placed against it by the landslide, thus providing an excellent example of the structural strength of an arch dam.

11-7.3 Abutment Failure Cases

11-7.3.1 Malpasset Dam

Malpasset Dam, 220 ft. high, Frejus, France –Failed in 1959 after a slow initial filling period which took 5 years. The dam was a thin double-curvature concrete arch completed in 1954 in southern France. The dam was 5-feet-thick at the crest and 22-feet-thick at the base. Blanket grouting was performed at the dam-foundation contact, but no grout curtain or drainage was

installed, and no instrumentation other than survey monuments was provided. The dam was founded on gneiss.

The reservoir filled for the first time on December 2, 1959. Although earlier there had been some clear seepage noted on the right abutment and a few cracks had been observed in the concrete apron at the toe of the dam, engineers visiting the site on December 2 did not notice anything unusual. About 9:10 p.m. that evening, the dam tender heard a loud cracking sound, about 1 mile downstream of the dam. The sudden failure sent a flood wave down the river causing destruction along a 7 mile course to the Mediterranean Sea. The number of deaths resulting from the failure was reported to be 421.

The failure was attributed to sliding of a large block of rock in the left abutment of the dam formed by an upstream dipping fault on the downstream side, and a foliation shear on the upstream side. The "mold" left by removal of the block could be clearly seen following the failure. Large uplift pressures were needed on the upstream shear in order to explain the failure. Experiments suggested that the arch thrust acting parallel to the foliation decreased the permeability perpendicular to the foliation to the point where large uplift pressures could have built up behind a sort of underground dam. The uplift forces in combination with the dam thrust were sufficient to cause the block to slide, taking the dam with it (Anderson et al 1998).
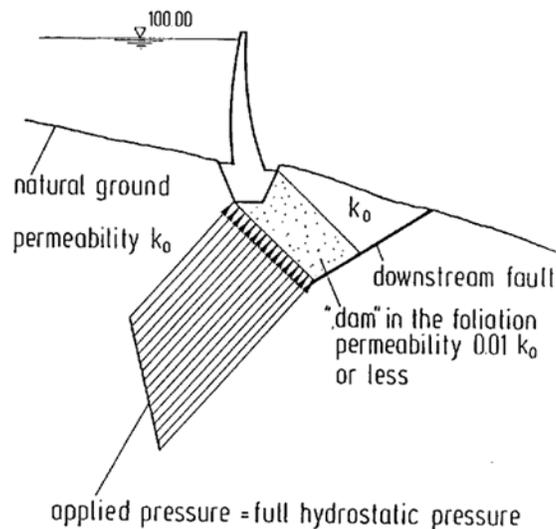
The event tree was likely:

1) Upstream dipping fault and downstream dipping foliation shear formed left abutment block.
2) Arch thrust in direction of foliation decreased permeability.
3) Tensile stress at upstream face opened foliation shear.
4) Nearly full uplift developed on foliation.
5) Block slid out on fault (phi = 30˚) and dam went with it.

11-7.3.1.2 Lessons Learned

Abutment analysis must include 3D analysis of any rock wedges that may be capable of failure under the loads applied by the dam thrust and under uplift forces created by seepage from the reservoir. Geological investigations must be conducted in the abutments to identify all adversely oriented rock discontinuities. Foundations of arch dams should be drained to reduce uplift forces. Instruments should be provided in the abutments to monitor uplift pressure and deflections in the foundation.

11-7.3.2 Experimental Plum Dam

Plum Dam, located in Fujian Province in south-east China, was an experimental cylindrical arch dam with a height of 72 ft. (22 m) and a crest length of about 238 ft. (72.6 m). The dam failed in September 1981 shortly after it was completed in May of the same year. Since the dam was an experimental structure built at a coastline site, its failure caused negligible property damage and no loss of life.

The dam was built as a masonry structure composed of granite blocks in the main body of the dam and included a peripheral joint between the dam and its artificial concrete abutment. The joint surfaces were coated with bitumen and polyvinyl chloride was used to seal the joint.

On the morning of September 18, the dam was inspected and nothing unusual was noticed. At 1:25 pm on the same day a local person had walked across the dam, but 10 minutes later the dam ruptured spectacularly without any warning. The peripheral joint surface showed two sets of frictional traces, one parallel to the dam axis and another inclined toward the downstream at 30°. The traces parallel to the dam axis were light and those toward the downstream were deep scratches at the upper elevations and shallow traces at lower levels. Based on the above observations and detailed inspection of the failed dam, the following scenario was offered as the most probable mode of failure:

1) The body of the dam moved up along the peripheral joint, producing the first set of frictional traces parallel to the axis of the dam.
2) The upward movement in turn caused widening of the horizontal arch spans, stressing the crown to the point of rupture.
3) The sudden failure of the structure was triggered by shearing of the top portion, which did not include any joint.

Up-abutment sliding along bitumen coated joint

Crack

Artificial abutment
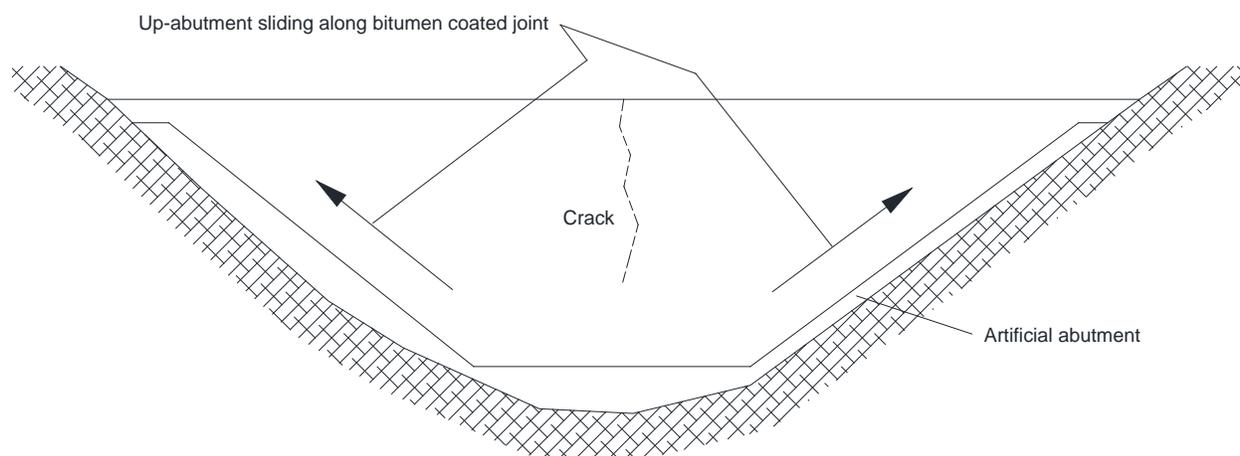
11-7.4 High-Discharge Induced Incidents

11-7.4.1 Failure of Arch Dams

One of the chief causes of dam failure, considering all types of dams, is overtopping or inadequate spillway capacity. However, the number of arch dams that have been damaged or have failed while passing extreme floods is quite small. The International Commission on Large Dams (ICOLD) Bulletin 99 (1995) lists only one arch dam that failed due to overtopping (Alla Sella Zerbino Dam, see Section 11-7.1). One possible explanation for the fact that overtopping is not as significant in arch dams as in other types of dams could be that arch dams are typically built on sound rock foundations.

The chief danger from overtopping an arch dam would be erosion of the abutments or the foundation. Thus, a minor amount of overtopping of an arch dam may not be dangerous as long as the abutments and foundation are sound and the depth of overtopping is not great and does not occur with a long duration. A description of the experience with Gibson dam is notable and is presented here because the dam, although severely overtopped, did not fail.

Gibson Dam. Gibson dam is a concrete arch-gravity dam on the Sun River in Montana which was completed in 1929. It is protected by a "morning-glory spillway" near the left abutment, which is controlled by six 34-ft. by 12-ft. radial gates which were added in 1938 to increase the reservoir capacity. Although the dam did not fail, it was overtopped for 20 hours at a depth of approximately 6.5 feet during passage of a record flood in June of 1964. Some rock was plucked from the abutments but neither the dam nor the abutments suffered significant damage and stability of the dam was never threatened.

11-7.4.2 Damage to Stilling Basins and Plunge-Pools

Plunge-Pools. As the previous section states, only a few arch dams have failed or been damaged by the passage of extreme floods. However, serious threats to arch dams could arise as a result of erosion of the downstream plunge-pool if the erosion were to occur near enough to the dam. Kariba dam in Zimbabwe provides an example of such a threat.

Kariba, completed in 1962, is a 426-foot high arch dam which impounds the world's largest man-made lake. The spillway consists of six orifices (28 x 30 feet), which discharge through the dam and impact in the downstream plunge-pool. The rock is generally regarded to be sound gneiss. When the dam was designed in 1955, two power plants were envisioned and it was estimated that the spillway would discharge only about once in five years. However, the second power plant was never built; as a result the spillway has operated more frequently than planned with spill durations of several months. By 1967 the maximum scour depth in the plunge-pool had reached 160 feet and a total volume of more than 500,000 cubic yards of rock was removed and carried downstream by the flow. By 1981 the scour depth had reached almost 200 feet and there was considerable concern about the potential instability of the dam foundation. As a result, some repairs have been made to the plunge-pool and erosion seems to have been abated. However, a prolonged drought in the drainage basin above Kariba has greatly reduced the frequency of spills for the past several years. Currently, the plunge-pool is being monitored annually and necessary repairs are being made including rock bolting and placement of concrete in critical areas. A side issue at Kariba is erosion of the abutments by runoff produced by spray. As much as four inches of water per day falls on some parts of the abutments when the spillway is operating. Gravel has been placed on the abutments in critical areas to prevent serious erosion.

11-7.5 Earthquake Induced Damage

Concrete arch dams have an excellent record of performance with respect to earthquake motion. No failure has ever resulted from earthquake damage to an arch dam. It must be realized however, that very few major earthquakes have occurred close to an arch dam. Major earthquakes on the order of the maximum credible earthquake are very rare events, and in most cases the MCE for a given dam site represents an unprecedented loading condition.

Among some 43 arch dams in 14 countries that are known to have been subjected to significant earthquake excitation (Serafim, 1987), only four have experienced a maximum or a near-maximum earthquake shaking with epicenter close to the dam site. The four arch dams are Pacoima, Lower Crystal Springs, and Gibraltar dams in the United States, and Ambiesta Dam in Italy. Except for Pacoima Dam, which suffered damage during two recent earthquakes, all other 42 dams experienced very little or no damage. Following is a description of the performance of Pacoima Dam.

11-7.5.1 Pacoima Dam

Pacoima Dam is a flood control arch dam located in the San Gabriel Mountains north of Los Angeles. It was constructed in twelve vertical cantilever monoliths that are separated by eleven evenly-spaced contraction joints and interlocked with 12 inch deep beveled, grouted keys. The dam is 10.4 feet thick and 589 foot long at the crest and 99 feet thick at the base. The left abutment is supported by a 60-foot-tall thrust block. Pacoima Dam was not designed for earthquake loads.

The dam was shaken by the 1971 M6.6 San Fernando earthquake (horizontal accelerations due to topographic amplification was 1.25 g on the left abutment), and the 1994 M6.8 Northridge earthquake (accelerations of 0.53 g at the base and 2.0 g at the sidewalls near the crest). The dam survived both events, but the reservoir was down 150 feet in 1971 and 130 feet in 1994. As a result of the 1971 earthquake, a crack formed in the thrust block, a previously grouted contraction joint opened up 0.4 inches, and extensive cracks accompanied by displacements of up to 8 inches vertically and 10 inches horizontally were found in the gunite which covered the left abutment. Three potentially unstable rock blocks were identified in this abutment, one of which underlies the thrust block. Seismic surveys indicated that a part of the San Gabriel mountain block to the left of the dam had been thrust up 4.2 feet vertically and 6.6 feet horizontally in a southwesterly direction. This geographical deformation resulted in an overall narrowing of the canyon that imposed new compressive forces on the dam. The distance between the left and right abutments decreased 0.49 inch and the axis of the dam rotated 30 seconds clockwise relative to the baseline. The entire structure tilted downward from the crest of the right abutment 0.68 inches relative to the left abutment. An extensive seismic instrumentation system was installed and the upper rock mass of the left abutment was secured to more competent rock below through the use of 35 rock anchors.

Following the 1994 earthquake, permanent vertical offsets (up to 2 inches) appeared along most of the vertical joints at the crest of the dam, with the elevation of each block dropping from left to right. The contraction joint between the dam and thrust block opened and remained open 2 inches at the crest, decreasing to 1/4 of an inch at the bottom of the joint (60 feet below the crest), at which point a large diagonal crack extended down the thrust block to meet the foundation rock (see figure below). Apparently, the diagonal crack and contraction joint opening were caused by movements of two rock masses on the left abutment: Rock Mass A, and Rock Mass B. Rock Mass A and its adjacent Rock Mass B which is supporting the thrust block, are underlain by a slip plane 1 and are known to have marginal factors of safety against sliding. Survey measurements made after the earthquake indicated that Rock Mass B slipped about 2-3 inches horizontally and 2 inches down, thereby accounting for opening in the contraction joint between the dam and thrust block, while Rock Mass A moved 16-19 inches horizontally and up to 14 inches down. During the 1971 event, Rock Mass A moved 50 percent less and the

movement of Rock Mass B was slight but enough to open up the same joint by 3/8 of an inch. The 35 tendons installed to secure the thrust block after the 1971 earthquake may have played a significant role in limiting the movement of Rock Mass B during the Northridge earthquake.
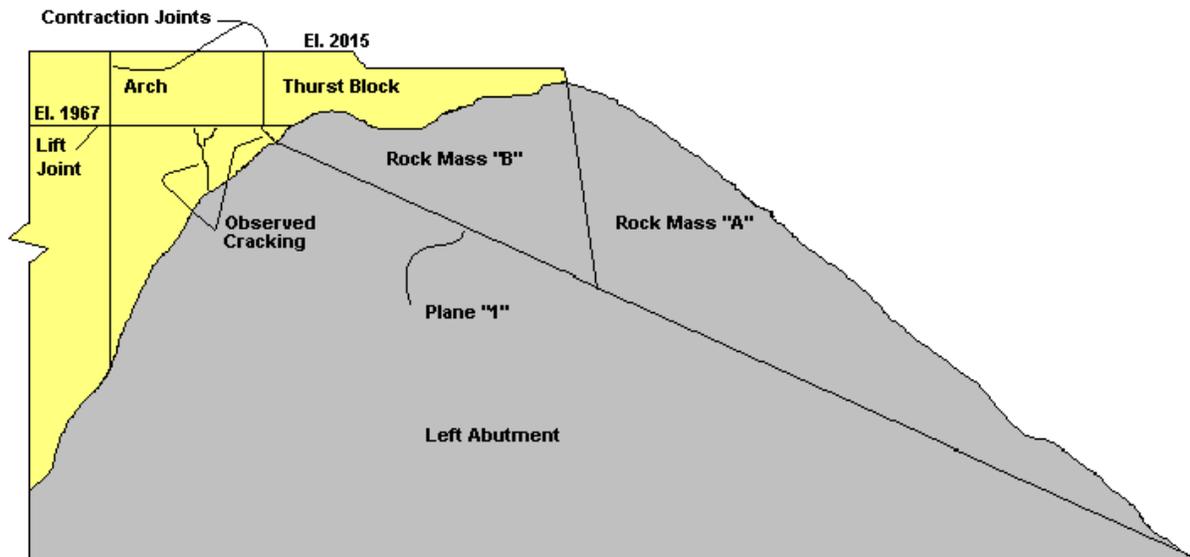
11-7.5.2 Reclamation Shake Table Tests

The U.S. Department of the Interior, Bureau of Reclamation (Reclamation), conducted shake table tests on 1/150-scale medium-thick arch dams. The dams had different nonlinearities: monolithic, one vertical contraction joint along the crown cantilever, one horizontal unbonded mid-height lift surface, 17 vertical contraction joints, and 17 vertical contraction joints with 2 horizontal unbonded lift surfaces.

Although the materials used for scale laboratory models cannot match the material properties of an actual dam (e.g., concrete, water, or foundation rock), these tests provide a greater understanding of the failure mechanisms or arch dams under seismic loading. Note that in every case, cracking developed in the dam approximately parallel to the valley wall. Vertical cracking also occurred. These cracks then formed free monoliths capable of independent movement (see next page).

MONOLITHIC MODEL

HORIZONTAL JOINT
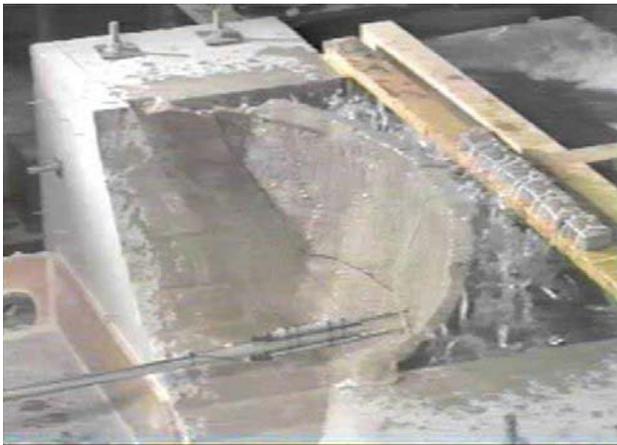
VERTICAL JOINT

Initial Crack   Final Failure

INITIAL CRACKS AND FINAL FAILURE PHOTOGRAPHS.

REFERENCES

Anderson, C., Mohorovic, C., Mogck, L., Cohen, B., and Scott, G. (1998). "Concrete Dams Case Histories of Failures and Nonfailures with Back Calculations" DSO-98-05

Babb, A. O. And T. W. Mermel (1968). Catalog of Dam Disasters - Failures and Accidents, PB 179 243, U.S. Bureau of Reclamation, Washington, D.C.

Bathe, K. J., and Wilson, E. L. (1976). "Numerical Methods in Finite Element Analysis," Prentice-Hall, Englewood Cliffs, NJ.

Bieniawski, Z. T. (1979). "The Geomechanics Classification in Rock Engineering Application", Proceedings of 4th International Congress on Rock Mechanics, ISRM, Montreux, Balkema, Rotterdam, Vol. 2. 11-167

Bieniawski, Z. T. (1990). "Tunnel Design by Rock Mass Classifications," Technical Report GL-79-19, U.S. Army Corps of Engineers, Waterways Experiment Station, Vicksburg, MS.

Charlwood, R. G., Solymar Z. V. and Curtis D. D. (1995). "A Review of Alkali Aggregate Reactions in Hydroelectric Plants and Dams", Proceedings of the International Conference on Alkali Aggregate Reactions in Hydroelectric Plants and Dams, Fredericton, Canada 129.

County of Los Angeles, (1994). Report on Initial assessment of the effects of the January 17, 1994, Northridge/San Fernando earthquake on Pacoima Dam, Phase 1. Prepared by Morrison Knudsen Corporation, April. 11-16.

Galera, J. M., Alvarez, M., and Bieniawski, Z. T. (2007), "Evaluation of the Deformation Modulus of Rock Masses using RMR, Comparison with Dilatometer Tests," Proceedings of the ISRM Workshop W1, Madrid, Spain, Jul. 6-7, 2007. Taylor & Francis, Madrid pp. 71-77.

Hendron, A. J. (1968). "Mechanical Properties of Rock," Pp 21 to 41, Rock Mechanics in Engineering Practice, Stagg, K. G., and Zienkiewicz, O. C., (Ed.), John Wiley & Sons, N.Y.

Hendron, A. J., and Patton, F. D. (1985). "The Vajont Slide, a Geotechnical Analysis Based on New Geologic Observations of the Failure Surface," U.S. Army Corps of Engineers, Waterways Experiment Station, Vicksburg, MS.

ICOLD (1995). Dam Failures, Statistical Analysis, Bulletin 99, International Commission on Large Dams, Paris, France.

Kirsten, H. A. D. (1982). "A Classification System for Excavation in Natural Materials," The Civil Engineer in South Africa, July.

Mason, P. J. (1984). "Erosion of Plunge Pools Downstream of Dams Due to the Action of Free-Trajectory Jets, Paper 8734, Proceedings of Inst. Civ. Engrs, Part 1, Pp 523-537, London.

Mason, P. J. (1985). "Free Jet Scour Below Dams and Flip Buckets," ASCE Journal of Hydraulic Engineering, Vol. 111, No. 2, February, New York, New York.

Raphael, J. M. (1984). "Tensile Strength of Concrete", ACI Journal, March-April

Bureau of Reclamation (2006). "Investigation of the Failure Modes of Concrete Dams Physical Model Tests", Report DSO-06-03

Sarkaria, G. S. (1997). "Lessons from Serious Incidents at Seven Arch Dams" Proceedings of the 1997 Annual Conference of the Association of State Dam Safety Officials.

Serafim, J. L. (1987). "A Note on the Earthquake Performance of Arch Dams," Proceedings of China-US Workshop on Earthquake Behavior of Arch Dams, Beijing, China.

U.S. Army Corps of Engineers (1996). Ice Engineering, EM-1110-2-1612, Headquarters, Department of the Army, Office of the Chief of Engineers, Washington D.C.

U.S. Army Corps of Engineers (1994). "Rock Foundations," Engineer Manual EM 1110-2-2908, US Army Corps of Engineers, Washington, D.C.

Westergaard, H. M. (1933). "Water pressures on Dams During Earthquakes," Transactions, American Society of Civil Engineers, Vol 98.

Zienkiewicz, O. C., (1971). "The Finite Element Method in Engineering Science," 2nd ed., McGraw-Hill, New York.

APPENDIX 11A

11A FOUNDATION ROCK ERODIBILITY

This appendix presents an approach to estimate erosion of rock downstream of arch dams. The methodology is based on the Erodibility Index Method (Annandale 1995) and principally focuses on erosion caused by plunging jets. More detailed information elaborating on the material provided in this chapter are found in Annandale (2006).

Note: For this appendix, all units are metric.

11A-1 EROSION PREDICTION CONCEPT

The approach to assessing erosion of rock is based on comparing the erosive capacity of flowing water and the ability of rock to resist erosion. If the erosive capacity of flowing water exceeds the erosion resistance of the rock, erosion will occur. Alternatively, if the erosive capacity of the flowing water is less than the erosion resistance offered by rock erosion will not occur.

It is therefore necessary to have available an erosion threshold relating the ability of rock to resist erosion to the erosive capacity of flowing water. Such a threshold is schematically shown in Figure 11A-1. The erosion threshold graph relates the Erodibility Index (a geomechanical index quantifying the relative ability of rock to resist erosion) to stream power (a hydraulic variable used to quantify the erosive capacity of flowing water).
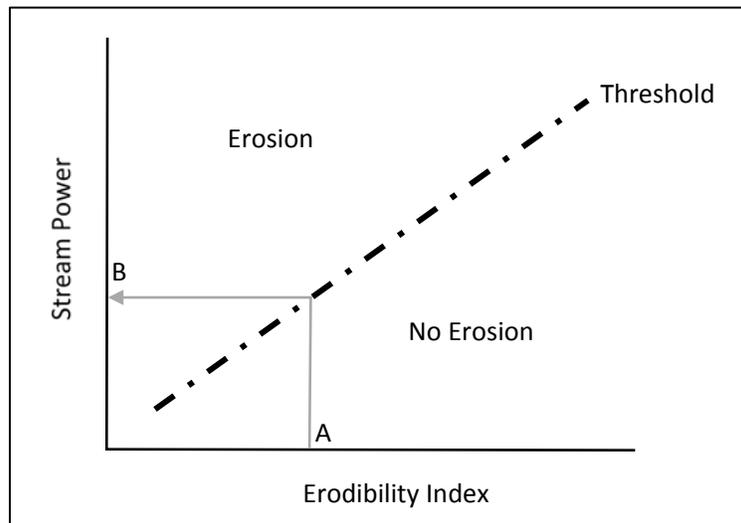
Figure 11A-1

If the magnitudes of the Erodibility Index of the rock and the stream power of flowing water are known for a certain situation it is possible to determine whether the rock will erode. This is done by plotting the point relating the Erodibility Index and the stream power on the graph. If the point plots above the erosion threshold line it is concluded that erosion will occur. Alternatively, if the point plots below the threshold erosion is deemed not to occur.

The above procedure only indicates whether rock will erode or not. It does not indicate the extent of scour; i.e. how deep a scour hole will advance. A special procedure has been developed to accomplish this goal, using the same erosion threshold relationship (Annandale 2006). This is done by using the erosion threshold to convert the Erodibility Index to threshold stream power. For example, if the Erodibility Index of a certain rock layer is known (A in Figure 11A-1), moving vertically towards the threshold line and then horizontally to the ordinate determines, B, the magnitude of the threshold Stream Power that the rock can resist.

By quantifying the Erodibility Indices of a geologic formation as a function of depth below the surface makes it possible to also spatially quantify the stream power that the rock can resist as a function of depth below the surface. A graph relating the stream power that the rock can resist to elevation below the ground surface can therefore be prepared (top right image in Figure 11A-2).

Completing the analysis requires quantifying the change in the erosive capacity of flowing water as a function of depth below the water surface. Once known, the variation in stream power of the flowing water can also be plotted on a graph as a function of elevation (top left image in Figure 11A-2).
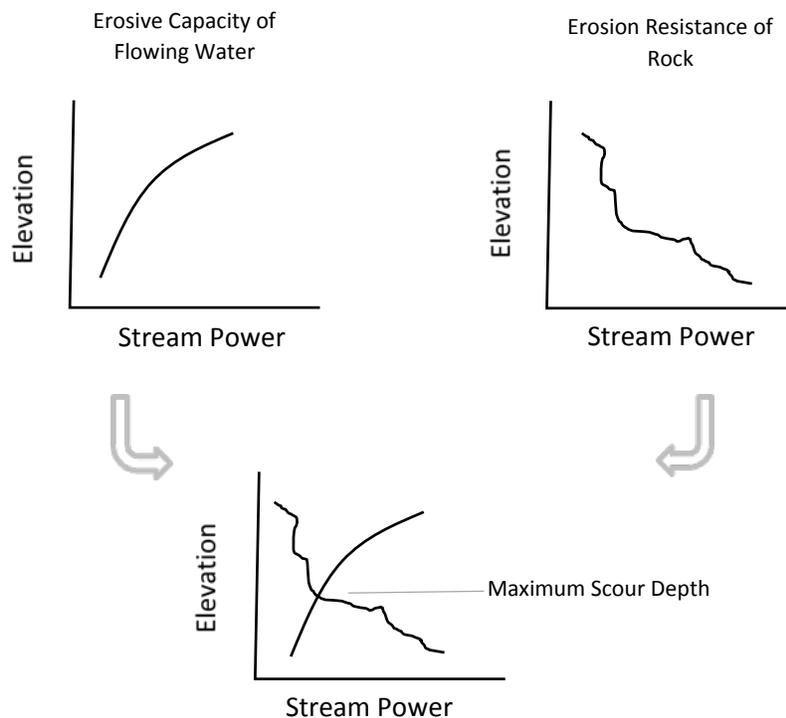
Figure 11A-2 – Adapted from Annandale (2006).

Plotting the two relationships thus developed on one graph, as shown at the bottom of Figure 11A-2, allows quantification of the maximum scour depth. The maximum scour occurs where the curve representing the stream power of the flowing water crosses the curve representing the erosion resistance of the rock (i.e. its threshold stream power). At that location the stream power of the water equals the erosion threshold of the rock. The maximum erosion depth has therefore been reached.

Experience with this approach shows that it is extremely important to understand and represent the spatial distribution of geologic conditions below the ground surface when conducting an erosion analysis. Case studies by Rock (2015) found that correlation between observed and calculated scour depths was extremely poor when geologic data was lacking. Using "average" geologic properties to represent the subsurface as a whole in such cases produce unsatisfactory results. Cases where geologic conditions were better defined, making it possible to calculate the spatial distribution of the rock's resistance to erosion produced satisfactory results. It is therefore emphasized that enough geologic information should be made available, allowing estimation of the spatial distribution of the threshold stream power of the rock as a function of elevation below the ground surface.

11A-2 EROSION THRESHOLD ROSION

Annandale (1995) developed an erosion threshold relating the Erodibility Index of earth materials, K(-)[1], to the stream power of flowing water (Figure 11A-3). The graph contains two types of events, those presenting scour and those presenting no scour[2]. The dashed line separating the two sets of data is the erosion threshold, P_t (kW/m^2), which can also be calculated as:

$$P_t = K^{0.75} \qquad \qquad (11A-1)$$

11A-3 ERODIBILITY INDEX

The Erodibility Index, which is a function of material strength, block size, discontinuity conditions and rock orientation, is used to quantify the relative ability of rock to resist erosion. The resistance to erosion increases with increasing magnitude of the value of the Erodibility Index, K, defined as (Annandale 1995),

$$K = M_s \cdot K_b \cdot K_d \cdot J_s \qquad \qquad (11A-2)$$

Where M_s = mass strength number; K_b = block size number; K_d = discontinuity/bond shear strength number; and J_s = relative ground structure number.

Rock core log data obtained from standard engineering geologic investigations contain the information used to quantify the Erodibility Index.

---

[1] Nomenclature fore dimensionless values.
[2] The terms "scour" and "erosion" are used interchangeably, conveying the same meaning.
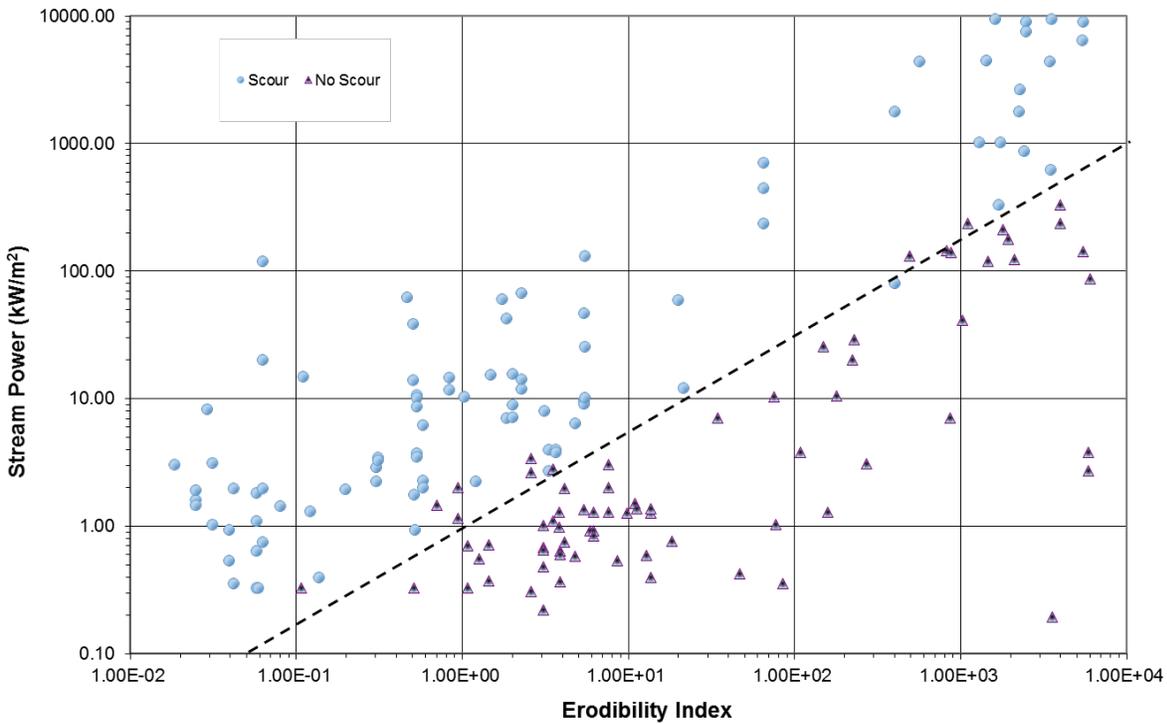
Figure 11A-3 – Adapted from Annandale (1995) with additional data added.

11A-3.1 Mass Strength Number

The mass strength number is a function of the Unconfined Compressive Strength (UCS) of the rock, determined by either using standard field descriptions shown in Table 11A-1 or as shown below,

$$M_s = C_r \cdot 0.78 \cdot UCS^{1.05} \text{ when } UCS \leq 10MPa \qquad (11A\text{-}3)$$

$$M_s = C_r \cdot UCS \text{ when } UCS > 10MPa \qquad (11A\text{-}4)$$

C_r is the coefficient of relative density defined in terms of acceleration of gravity (g in m/s^2) and the mass density of the rock (ρ_r in kg/m^3). The numeric term in the denominator normalizes C_r to a reference weight of rock (N/m^3).

$$C_r = \frac{g \cdot \rho_r}{27 \cdot 10^3} \qquad (11A\text{-}5)$$

11A-4

Table 11A-1 Mass Strength Number for Rock (Kirsten, 1982).

Hardness	Identification in Profile	Unconfined Compressive Strength (MPa)	Mass Strength Number (M$_s$)
Very Soft Rock	Material crumbles under firm (moderate) blows with sharp end of geological pick and can be peeled off with a knife. Is too hard to cut tri-axial sample by hand.	Less than 1.7 1.7 – 3.3	0.87 1.86
Soft Rock	Can just be scraped and peeled with a knife; indentations 1mm to 3mm show in the specimen with firm (moderate) blows of the pick point	3.3 – 6.6 6.6 – 13.2	3.95 8.39
Hard Rock	Cannot be scraped or peeled with a knife; handheld specimen can be broken with hammer end of geological pick with a single firm (moderate) blow.	13.2 – 26.4	17.7
Very Hard Rock	Hand-held specimen breaks with hammer end of pick under more than one blow.	26.4 – 53.0 53.0 – 106.0	35.0 70.0
Extremely Hard Rock	Specimen requires many blows with geological pick to break through intact material.	Larger then 212.0	280

11A-3.2 Block Size Number

The block size number, K_b, is a function of joint spacing and the number of joint sets in a rock mass, calculated as shown in Equation 11A-6. Joint spacing is estimated based on Rock Quality Designation (RQD) and the number of joint sets, established from Kirsten's (1982) joint set number (J_n) (Table 11A-2). More intact rock, with fewer joint sets and high values of *RQD*, represents larger rock blocks, which are more difficult to remove by flowing water.

$$K_b = \frac{RQD}{J_n} \qquad (11A-6)$$

With $0 \leq K_b \leq 100$.

Table 11A-2 – Joint Set Number (Kirsten, 1982).

Number of Joint Sets	Joint Set Number (J_n)
Intact, no or few joints / fissures	1.00
One joint / fissure set	1.22
One joint / fissure set plus random	1.50
Two joint / fissure sets	1.83
Two joint / fissure sets plus random	2.24
Three joint / fissure sets	2.73
Three joint / fissure sets plus random	3.34
Four joint / fissure sets	4.09
Multiple joint / fissure sets	5.00

11A-3.3 Discontinuity / Bond Shear Strength Number

The discontinuity/bond shear strength number, K_d, represents the relative resistance offered by friction in rock discontinuities. It is calculated from the joint roughness number (J_r) and joint alteration number (J_a), i.e.

$$K_d = \frac{J_r}{J_a} \qquad\qquad (11A-7)$$

Joint roughness contributes to rock stability due to the higher frictional resistance. Joint infill or alteration detracts from the resistance. Table 11A-3 offers joint roughness numbers and Table 11A-4 joint alternation numbers.

Table 11A-3 Joint Roughness Number (Kirsten, 1982).

Joint Separation	Condition of Joint	Joint Roughness Number (J_r)
Joints / fissures tight or closing during excavation	Stepped joints / fissures	4.0
	Rough or irregular, undulating	3.0
	Smooth undulating	2.0
	Slickensided undulating	1.5
	Rough or irregular, planar	1.5
	Smooth planar	1.0
	Slickensided planar	0.5
Joints / fissures open and remain open during excavation	Joints/fissures either open or containing relatively soft gouge of sufficient thickness to prevent joint/ fissure wall contact upon excavation.	1.0
	Shattered or micro-shattered clays	1.0

Table 11A-4 Joint Alteration Number (Kirsten, 1982).

Description of Gouge	Joint Alteration Number (J_a) for Joint Separation (mm)		
	1.0	1.0 – 5.0	5.0
Tightly healed, hard, non-softening impermeable filling	0.75	-	-
Unaltered joint walls, surface staining only	1.0	-	-
Slightly altered, non-softening, non-cohesive rock mineral or crushed rock filling	2.0	2.0	4.0
Non-softening, slightly clayey non-cohesive rock mineral or crushed rock filling	3.0	6.0	10.0
Non-softening, strongly over-consolidated clay mineral filling, with or without crushed rock	3.0	6.0**	13.0
Softening or low friction clay mineral coatings and small quantities of swelling clays	4.0	8.0	13.0
Softening moderately over-consolidated clay mineral filling, with or without crushed rock	4.0	8.0**	13.0
Shattered or micro-shattered (swelling) clay gouge, with or without crushed rock	5.0	10.0**	18.0

** Also applies when crushed rock occurs in clay gouge without rock wall contact.

The discontinuity/bond shear strength number can also be expressed in terms of the residual friction angle, κ, as follows (Annandale 2006).

$$K_d = \tan(\kappa) \qquad (11\text{A-}8)$$

(a)   (b)
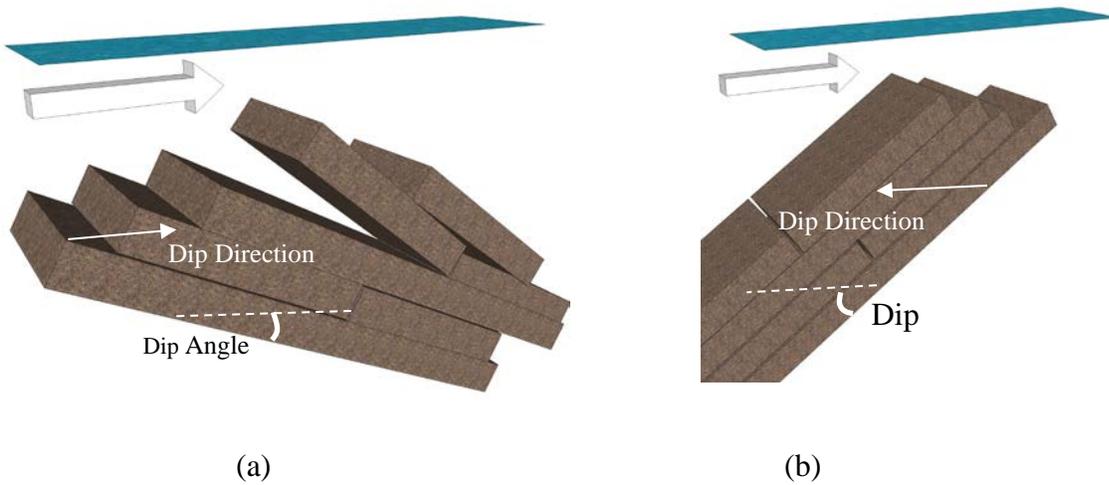
Figure 11A-4 – Adapted from Annandale (1995).

(a)   (b)
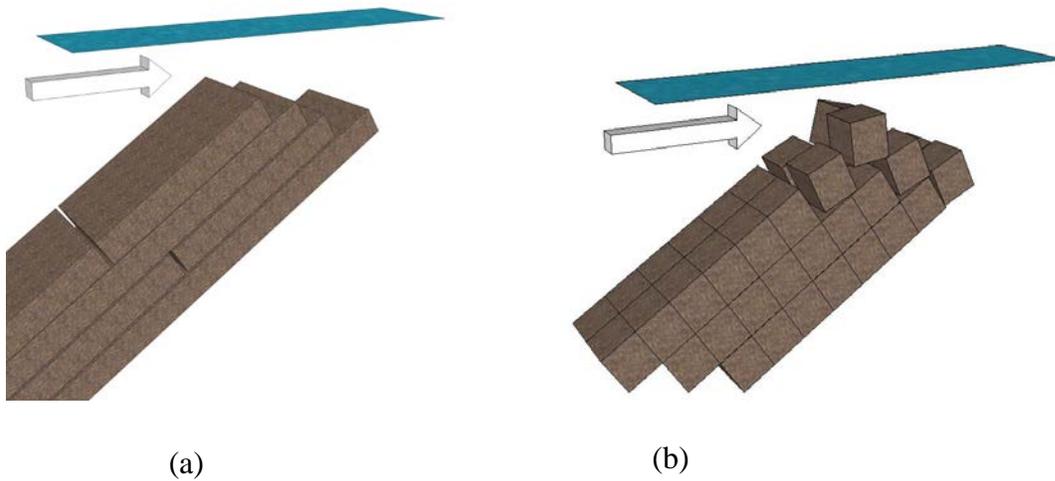
Figure 11A-5 – Adapted from Annandale (1995).

11A-3.4 Relative Ground Structure Number

The relative ground structure number is a function of the orientation of least favorable discontinuities within the rock, that is, discontinuities that are most easily eroded due to their orientation relative to flow direction, and the shape of the material units (Figures 11A-4 and 11A-5).

Figure 11A-4 (a) illustrates that rock slabs can be lifted by flowing water from left to right in the figure when rock is dipped in the direction of flow, but is more resistant to erosion when dipped against the direction of flow (Figure 11A-4(b)).

Figure 11A-5 (a) shows that elongated slabs are more resistant to erosion by flowing water, and that equisided blocks are less resistant (Figure 11A-5 (b)). The relative ground structure number representing the relative influence of block shape and orientation relative to flow direction can be quantified from Table 11A-5.

11A-4 CONVERSION OF THE ERODIBILITY INDEX TO THRESHOLD STREAM POWER

With the Erodibility Index, K, known for each distinct geologic stratum erosion thresholds can be assigned and expressed in terms of stream power using the concept explained in Figure 11A-1. As already indicated, <u>it cannot be emphasized strongly enough that average geologic values should not be used to characterize the erosion resistance of a rock formation</u> (Annandale 2006; Rock 2015; Rock et al. 2016). Adequate geologic information should be made available to quantify the spatial distribution of rock's erosion resistance.

Table 11A-5 Relative Ground Structure Number (Kirsten, 1982).

Dip Direction of Closer Spaced Joint Set relative to Flow Direction (degrees)	Dip Angle of Closer Spaced Joint Set relative to Flow Direction (degrees)	Ratio of Joint Spacing[1], r			
		1:1	1:2	1:4	1:8[2]
180 / 0	90	1.14	1.20	1.24	1.26
In Direction of Flow	89	0.78	0.71	0.65	0.61
	85	0.73	0.66	0.61	0.57
	80	0.67	0.60	0.55	0.52
	70	0.56	0.50	0.46	0.43
	60	0.50	0.46	0.42	0.40
	50	0.49	0.46	0.43	0.41
	40	0.53	0.49	0.46	0.45
	30	0.63	0.59	0.55	0.53
	20	0.84	0.77	0.71	0.67
	10	1.25	1.10	0.98	0.90
	5	1.39	1.23	1.09	1.01
	1	1.50	1.33	1.19	1.10
0 / 180	0	1.14	1.09	1.05	1.02
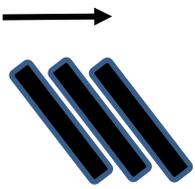
Continued

Dip Direction of Closer Spaced Joint Set relative to Flow Direction (degrees)	Dip Angle of Closer Spaced Joint Set relative to Flow Direction (degrees)	Ratio of Joint Spacing[1], r			
		1:1	1:2	1:4	1:8[2]
Against Direction of Flow	-1	0.78	0.85	0.90	0.94
	-5	0.73	0.79	0.84	0.88
	-10	0.67	0.72	0.78	0.81
	-20	0.56	0.62	0.66	0.69
	-30	0.50	0.55	0.58	0.60
	-40	0.49	0.52	0.55	0.57
	-50	0.53	0.56	0.59	0.61
	-60	0.63	0.68	0.71	0.73
	-70	0.84	0.91	0.97	1.01
	-80	1.25	1.41	1.53	1.61
	-85	1.39	1.55	1.69	1.77
	-89	1.50	1.68	1.82	1.91
180 / 0	-90	1.14	1.20	1.24	1.26
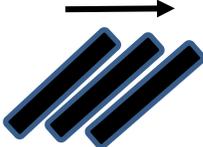
[1]For intact material use $J_s = 1.0$.

[2]For values of r greater than 8 use J_s as for r = 8.

11A-5 EROSIVE CAPACITY OF FLOWING WATER

The flow conditions of interest when executing erosion analysis of rock at arch dams are generally represented by plunging jets originating from flows over dam crests (nappe flows), from flip buckets (ski jumps) and from orifices releasing water under pressure (valves and gates). The procedure for calculating the erosive capacity of plunging jets entails quantifying the stream power at the tailwater surface and how it changes below the water surface. When using the Erodibility Index Method (Annandale 1995, 2006) stream power is quantified in terms of kW/m^2, most effectively achieved using SI Units. It is strongly recommended to perform hydraulic calculations using SI Units to prevent unnecessary conversion error. The approach in the following paragraphs is therefore based on SI Units.

The stream power of a plunging jet, P_{jet} (kW/m^2), at the tailwater surface is expressed as (Annandale 2006)

$$P_{jet} = \frac{\gamma \cdot Q \cdot H}{A_j} \qquad (11A\text{-}9)$$

Where γ = specific weight of water (9.807kN/m^3); Q = total discharge of the plunging jet (m^3/s) H = energy head (m); A_j = footprint area of the jet on the tailwater surface (m^2).

11A-5.1 Jet Geometry

In what follows ways to calculate the jet characteristics for each of the three types of jets are first presented. Thereafter, methods to quantify energy losses as the jets plunge through the air and below the tailwater elevation (i.e. within the plunge pool) are presented.

11A-5.1.1 Nappe Jets

Figure 11A-6 illustrates the main features of a free-falling nappe jet into a plunge pool. The jet flows over the crest of the spillway of the dam with issuance velocity (at the point of jet issuance shown in the figure) $V_i = 2\sqrt{gh}$ (m/s), issuance jet thickness $B_i = q/V_i$ (m), and $q = h^{3/2} \cdot C_d =$ specific flow (m²/s)[3] (Castillo et al., 2014; Castillo, 2015). Where h = energy head (m) at the crest of the weir; C_d = discharge coefficient = 2.1 (m$^{1/2}$/s) for three-dimensional flow at arch dams and 1.7 (m$^{1/2}$/s) for two-dimensional flow over flat topped gravity dams (Castillo and Carrillo, 2016).

The core of the jet reduces in thickness due to the effects of gravity, while the outer jet dimension increases due to air entrainment. Eventually the air entrainment is so large that it leads to complete jet breakup; a condition known as a fully developed jet. This occurs when the jet breakup length, L_{b_nappe}, is shorter than the total jet length, L_j.

For plunging nappe jets, as shown in Figure 11A-6, the jet length, L_j, is approximately equal to the hydraulic head, H. Where the jet plunges onto the tailwater surface (plunge pool water surface) the thickness of the jet has increased to B_j and the jet velocity equals $V_j = \sqrt{2gH}$. The jet core no longer exists from the point where complete jet breakup occurs (Ervine and Falvey, 1987).

---

[3] Note that the issuance location is $h_o = 2h$ below the reservoir water surface.
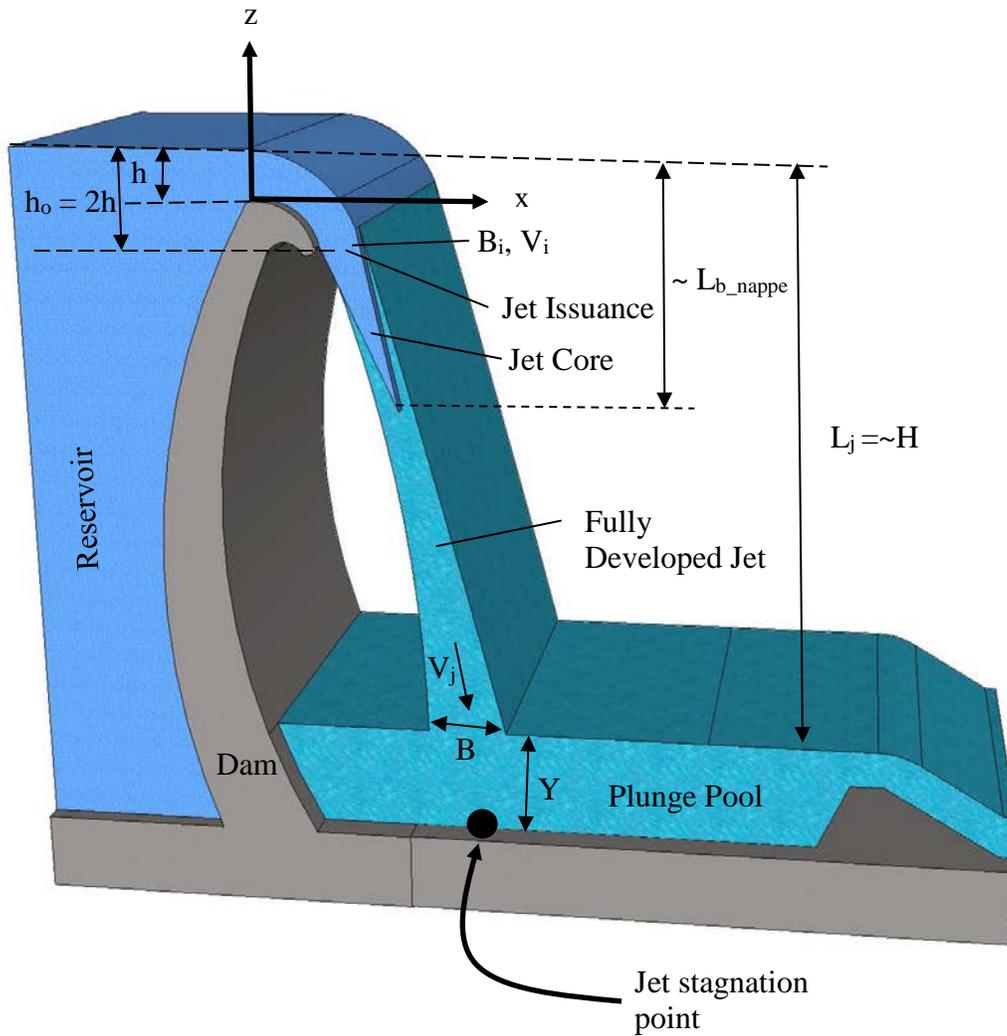
Figure 11A-6 – Adapted from Castillo et al. (2015).

For nappe flow the impingement jet thickness, B_j, can be calculated using the following equation (Castillo et al. 2014; Castillo 2015):

$$B_j = B_g + 2 \cdot \xi = \frac{q}{\sqrt{2 \cdot g \cdot H}} + 4 \cdot \varphi \cdot \sqrt{h} \cdot \left(\sqrt{2 \cdot H} - 2 \cdot \sqrt{h} \right) \qquad (11A\text{-}10)$$

Where B_g = thickness of the jet as affected by gravity (m); ξ = the lateral spread of the jet due to turbulence (m); $\varphi = K_\varphi \cdot T_u$, with T_u = issuance turbulence intensity (-) and K_φ = an experimental parameter use 1.24 (-) for the three-dimensional nappe flow over arch dams with inclined (ogee) crests, 1.20 (-) for two-dimensional flow over flat non-spillway portion of arch dams (as overtopping occurs when flows exceed the spillway design flow), and 1.14 (-) for circular jets (Castillo et al. 2016). Typical values of the issuance turbulence intensity are shown in Table 11A-6.

The breakup length of nappe jets L_{b_nappe} (m) along the jet is quantified as (Castillo 2016)

$$L_{b\_nappe} = \Gamma \cdot \frac{C_d^{0.82} h^{0.73}}{2g^{0.68} \varphi^{0.82}}$$ (11A-11)

Where $\Gamma = 0.85$ in the case of three-dimensional flow over an arch dam (inclined ogee crest) and 0.95 for two-dimensional flow over the flat-topped portion of an arch dam when flows exceed the spillway capacity and overtops the dam. The length calculated with Equation 11A-11 is along the jet. As an approximation, for nappe jets, the breakup length may be assumed to equal the vertical distance as shown in Figure 11A-6.

Table 11A-6 Typical Values of Issuance Turbulence Intensity (Bollaert, 2002; Castillo and Carillo, 2016).

Type of Outlet Structure	Turbulence Intensity, T_u
Three dimensional flow over ogee spillways of arch dams	0.012
Two dimensional flow over flat topped non-spillway portion of arch dams	0.013
Flip Buckets (Ski Jumps)	0.03-0.05
Valves (Release of pressurized flow leading to circular or semi-circular jets)	0.03-0.08

11A-5.1.2 Ski Jump Jets

The geometry of a typical ski jump is shown in Figure 11A-7. Two coordinate systems are shown in the figure, xz and $x'z'$. This is necessary to show because of the conventions used by Pfister et al. (2014) who provides equations for calculating the geometry of ski jump jets. The equations provided in this section, however, references the $x'z'$ coordinate system, with the origin as shown in Figure 11A-7.

The chute upstream of a ski jump has a bottom angle, φ, relative to the horizontal, with typical prototype values between almost horizontal for bottom outlets to as high as 50° on some dams (Pfister et al., 2014). The approach flow to the ski jump is described in terms of its black-water depth, h_o, and the Froude number, $Fr_o = V_o / \sqrt{g \cdot h_o}$, both defined immediately upstream of the ski jump. V_o = average approach flow velocity and g = acceleration due to gravity.

The angle, α, is the physical take-off angle, typically limited to no more than 30° (USBR, 1987). However, the actual take-off angle, known as the virtual take-off angle (Pfister et al., 2014), differs from the physical takeoff angle and are calculated as follows for the upper take-off angle, α_U, and lower take-off angle, α_L, relative to the $x'z'$ coordinate system (horizontal) (Pfister et al., 2016).
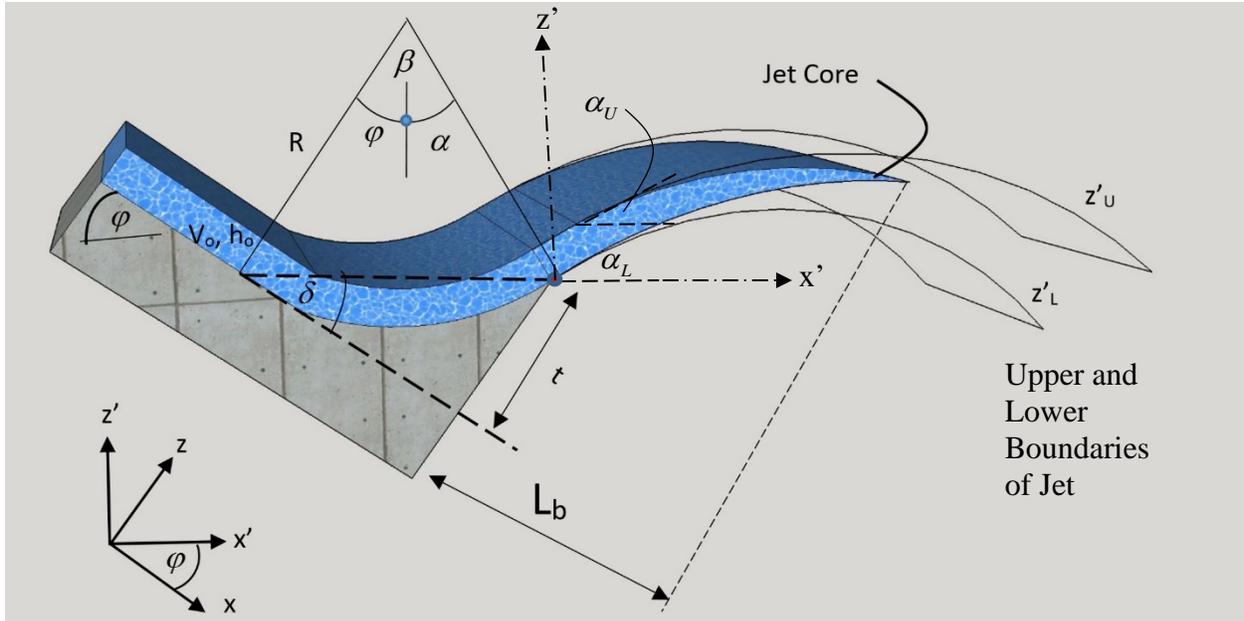
Figure 11A-7 – Adapted from Pfister et al. 2014

$$\alpha_U = \arctan(0.874 \cdot \Lambda - 0.031) \qquad (11A\text{-}12)$$

and

$$\alpha_L = \arctan(0.875 \cdot \Lambda - 0.080) \qquad (11A\text{-}13)$$

where

$$\Lambda = \tan(\alpha) \cdot \left(1 - \frac{h_o}{R}\right)^{1/3} \qquad (11A\text{-}14)$$

and

R = radius of the ski-jump; equation applies for $-0.32 \le \Lambda \le 0.84$ and $0.027 \le h_o/R \le 0.950$.

The breakup length of the jet, i.e. the length of the core of the jet measured along the x-axis is expressed as (Pfister et al., 2014):

$$L_{b\_flip} = 76 \cdot \phi \cdot h_o \qquad (11A\text{-}15)$$

if

$$0.05 \le \phi \le 0.13 \qquad (11A\text{-}16)$$

where

11A-14

$$\phi = \frac{(1 + \sin \varphi)}{Fr_o \cdot (1 + \tan \delta)^4} \qquad \text{(11A-17)}$$

and

$$12^o \le \varphi \le 30^o \qquad \text{(11A-18)}$$

$$\delta = \arctan\left(\frac{1 - \cos(\beta)}{\sin(\beta)}\right) \qquad \text{(11A-19)}$$

Equation 11A-15 can be written in terms of the $x'z'$ coordinate system as,

$$L_{b\_flip} = \frac{76 \cdot h_o \cdot (1 + \sin \varphi)}{Fr_o \cdot (1 + \tan \delta)^4} \cdot \frac{1}{\cos(\varphi)} \qquad \text{(11A-20)}$$

The trajectories of the upper and lower boundaries of the plunging jet, which can be used to estimate the total length of the jet, L_j and its thickness, B_j, at the elevation of the tailwater surface (plunge pool surface) (to quantify the footprint area, A_j, in Equation 11A-9 are calculated as follows (developed from Pfister et al. 2014):

$$z'_L = \frac{\left(2X'_L - \left(X'_L\right)^2\right) \cdot h_o \cdot F_o^2 \cdot \left(\sin(\alpha_L)\right)^2}{2} \qquad \text{(11A-21)}$$

where

$$X'_L = \frac{2x'}{h_o \cdot F_o^2 \cdot \sin(2\alpha_L)} \qquad \text{(11A-22)}$$

and

$$z'_U = \frac{\left(2X'_U - \left(X'_U\right)^2\right) \cdot h_o \cdot F_o^2 \cdot \left(\sin(\alpha_U)\right)^2}{2} + h_o \cdot \frac{\cos(\varphi)}{\cos(\alpha + \varphi)} \qquad \text{(11A-23)}$$

where

$$X'_U = \left(\frac{2 \cdot \left(x' + h_o \cdot \cos(90^o - \varphi)\right)}{h_o \cdot F_o^2 \cdot \sin(2\alpha_U)}\right) \qquad \text{(11A-24)}$$

11A-5.1.3 Circular Jets

A circular jet behaves in a similar manner as other jets with the core reducing in diameter, while the outer diameter of the jet continues to increase due to air entrainment. The issuance conditions for circular jets are shown in Figure 11A-8. The issuance diameter is D_i (m), the issuance velocity V_i (m/s) and the issuance Froude number is $Fr_i = V_i / \sqrt{2gD_i}$.

The trajectory of a circular jet, along its center line, can be calculated as (Wahl et al. 2008),

$$z = x \cdot \tan\theta - \frac{x^2}{4 \cdot h_v \cdot (\cos\theta)^2}$$ (11A-25)

where $h_v = V_i^2/2g$ = kinetic energy head (m). The length of the jet trajectory, L_j (m), can be determined from the calculated trajectory. With this known the outer dimension of a circular jet, D_{out} , at the point of impact can be calculated as (Ervine et al. 1997)

$$D_{out} = D_i + 2 \cdot 0.38 \cdot (T_u \cdot L_j)$$ (11A-26)

For circular jets the breakup length is (Ervine et al. 1997),

$$L_{b\_circular} = \frac{1.05 \cdot D_i \cdot Fr_i^2}{\left(1.14 \cdot T_u \cdot Fr_i^2\right)^{0.82}}$$ (11A-27)
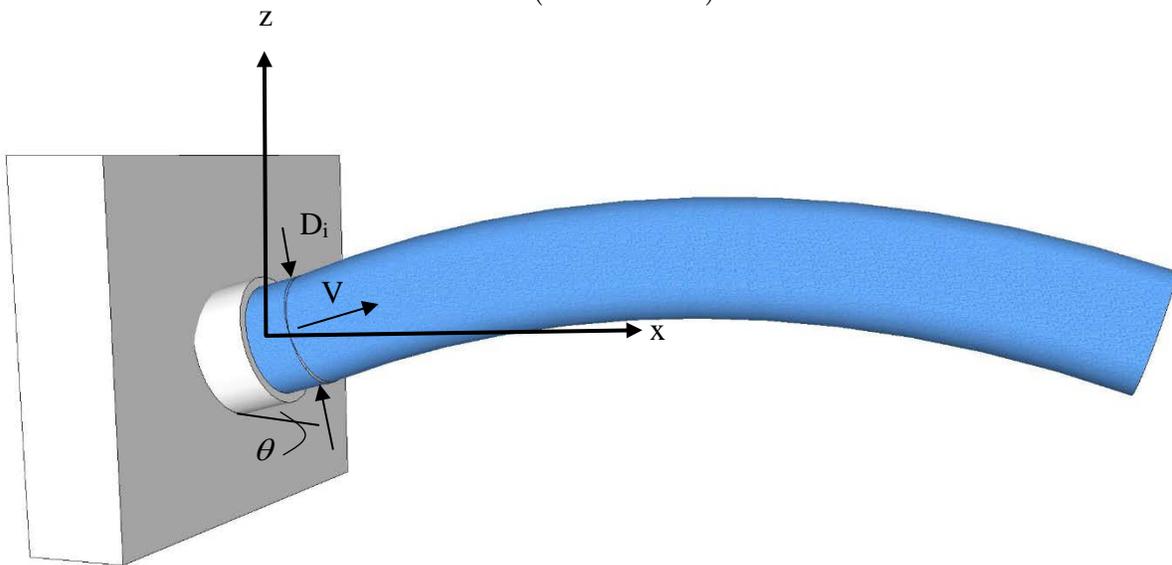
Figure 11A-8

11A-6 PLUNGE POOL

To calculate the unit stream power at the tailwater surface elevation (plunge pool surface) using Equation 11A-9, i.e.;

$$P_{jet} = \frac{\gamma \cdot Q \cdot H}{A_j}$$

requires quantifying the magnitude of the footprint area of the jet on the water surface, which for rectangular nappe and ski jump jets is calculated as,

$$A_j = B_j \cdot W \qquad (11A\text{-}28)$$

where W = the width of the jet at the water surface[4].

For nappe flow, B_j, is calculated using Equation 11A-10 and for a ski jump the thickness of the jet is calculated as the difference between the upper (z_U) and lower (z_L) boundaries of the jet at the elevation of the tailwater surface (plunge pool surface), determined using Equations 11A-12 through 11A-24.

For circular jets,

$$A_j = \frac{\pi \cdot D_{out}^2}{4} \qquad (11A\text{-}29)$$

where D_{out} is calculated with Equation 11A-26.

Quantification of the stream power of the jet, P, as a function of depth, Y, below the tailwater surface (plunge pool water surface) is based on the changes in the mean dynamic pressure and the fluctuating dynamic pressure below the plunge pool water surface, expressed as (Annandale, 2006):

$$P_{total} = C_p \cdot P_{jet} + F \cdot C_p^{'} \cdot P_{jet} \qquad (11A\text{-}30)$$

Where C_p = mean dynamic pressure coefficient; C'_p = fluctuating dynamic pressure coefficient; F= factor allowing for the effect of jet breakup on the fluctuating dynamic pressure; $F = 1$ for nappe and ski-jump jets (the effect of jet breakup is already included in the approach used to quantify fluctuating dynamic pressure for nappe and ski-jump jets). For circular jets the values of the fluctuating dynamic pressure coefficient, C'_p, and the reduction coefficient, F, are determined using Equations 11A-34 and 11A-35 and shown in Figures 11A-11 and 11A-12.

---

[4] In the case of arch dams, it is necessary to account for the convergence of flow due to the curvature of the dam by estimating W at the tailwater surface.

The degree of jet breakup determines the values of the mean and fluctuating dynamic pressure coefficients. The magnitudes of the coefficients are partly determined by energy loss through the air and energy loss as the jet flows through the water below its surface. Energy loss through the air occurs when blobs of water develop due to jet breakup and their fall velocity is affected by air resistance. The degree of jet breakup is determined by the jet breakup ratio[5] L_j/L_b.

Figures 11A-9 and 11A-10 provide dynamic and fluctuating pressure coefficient values for rectangular nappe jet flows of various breakup length ratios L_j/L_b (Castillo et al. 2016)[6], which are also applicable for circular jets when $L_j/L_b \leq 0.5$ (Ervine et al. 1997; Castillo et al. 2016). Of course, for circular jets the variable Bj on the abscissa is replaced by D_{out}.

Dynamic pressure coefficient values specifically for ski-jump jets have not yet been determined. Until such values have been established Figures 11A-9 and 11A-10 may be used to provide guidance. While acknowledging that these values may not be representative of actual conditions it may be deemed a reasonable assumption as ski-jump jets are usually rectangular.

For shallow pools ($Y/B_j \leq 5.5$) the dynamic pressure coefficient assumes constant values as depicted in Table 11A-7.

For deep pools ($Y/B_j > 5.5$), the dynamic pressure coefficient is expressed as

$$C_p = a \cdot \exp\left(-b \cdot Y/B_j\right) \tag{11A-31}$$

with values for the coefficients a and b found in Table 11A-8.

The fluctuating dynamic pressure coefficients for undeveloped and developed rectangular jets (Figure 11A-10) can be calculated with the following equations.

For $0 \leq Y/B_j \leq 14$,

$$C_p^{`} = a \cdot \left(\frac{Y}{B_j}\right)^3 + b \cdot \left(\frac{Y}{B_j}\right)^2 + c \cdot \left(\frac{Y}{B_j}\right) + d \tag{11A-32}$$

With the values of the coefficients a, b, c and d found in Table 11A-9.

---

[5] The breakup lengths L_{b_nappe} for nappe flow, L_{b_flip} for ski jump jets, and $L_{b\_circular}$ for circular jets are equated to L_b as appropriate.

[6] This implies that the curves $L_j/L_b \leq 0.85$ for the average dynamic pressure coefficient and $H/L_b \leq 0.80$ for the fluctuating dynamic pressure coefficient may be used for circular, intact jets. Relationships for fully developed round jets as affected by jet breakup length are not currently available.

And for $Y/B_j > 14$,

$$C_p' = a \cdot e^{-b \cdot (Y/B_j)}$$

(11A-33)

With coefficient values a and b found in Table 11A-10.
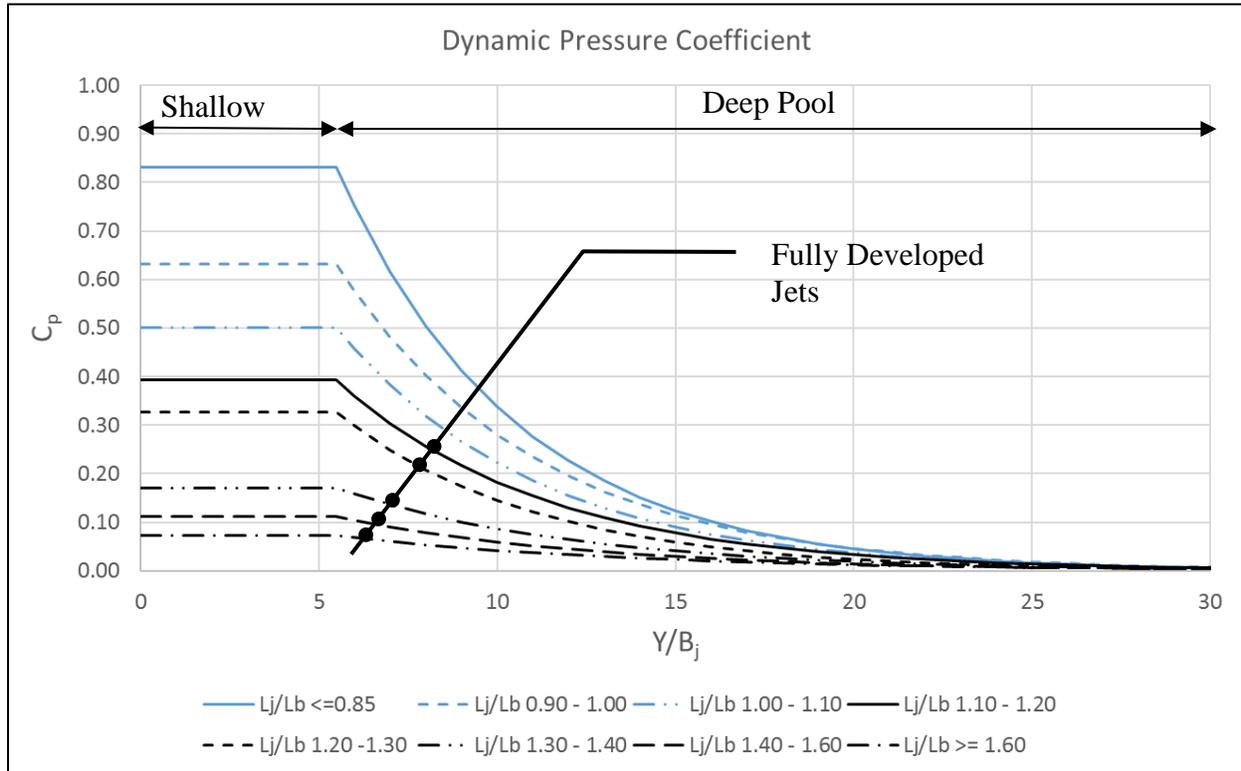
Figure 11A-9 – Adapted from Castillo et al., 2015.

For undeveloped circular jets the fluctuating dynamic pressure coefficient may be estimated using Equation 11A-34 and Figure 11A-11. Bollaert (2002) developed an equation (Equation 11A-34) that is intended to quantify the fluctuating dynamic pressure coefficient for circular jets as a function of the issuance turbulence intensity (see Table 11A-6 for guidance in selecting turbulence intensity).
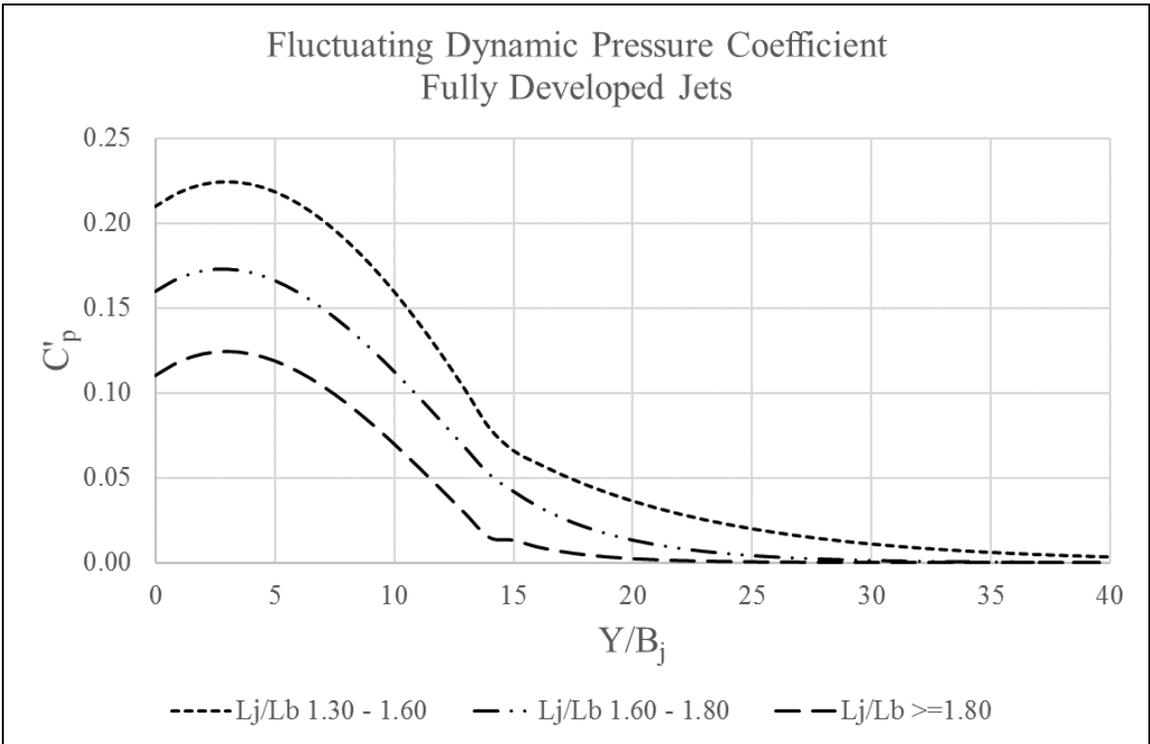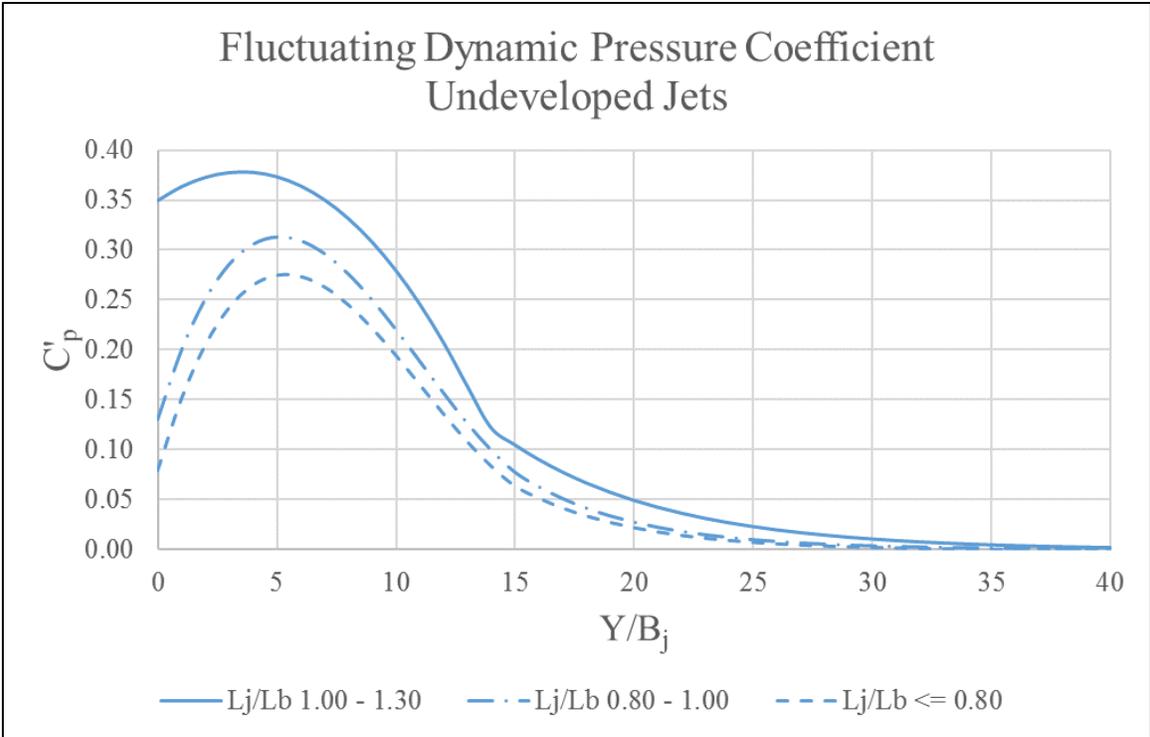
Figure 11A-10 – Adapted from Castillo et al., 2015.

Table 11A-7 Dynamic Press Coefficients for Shallow Pools ($Y/B_j \leq 5.5$) (Castillo et al., 2015).

L_j / L_b	C_p
≤ 0.85	0.83
0.90-1.00	0.63
1.00-1.10	0.50
1.10-1.20	0.39
1.20-1.30	0.33
1.30-1.40	0.14
1.40-1.60	0.11
≥ 1.60	0.07

Table 11A-8 Variable *a* and *b* for Calculating the Dynamic Pressure Coefficient for Deep Pools ($Y/B_j > 5.5$) Using Equation 11-2-4.31 (Castillo et al., 2015).

L_j / L_b	a	b
≤ 0.85	2.50	0.20
0.90-1.00	1,70	0.18
1.00-1.10	1.35	0.18
1.10-1.20	1.00	0.17
1.20-1.30	0.88	0.18
1.30-1.40	0.39	0.15
1.40-1.60	0.24	0.14
≥ 1.60	0.14	0.12

Table 11A-9 Variables $a, b, c,$ and d for Calculating the Fluctuating Pressure Coefficient Using Equation 11A-32 (Castillo et al., 2015).

L_j/L_b	$0 \leq Y/B_j \leq 14$			
	a	b	c	d
≤ 0.80	0.00030	-0.01000	0.0815	0.08
0.80 – 1.00	0.00030	-0.01000	0.0790	0.13
1.00 – 1.30	-0.00001	-0.00220	0.0160	0.35
1.30 – 1.60	0.00003	-0.00180	0.0100	0.21
1.60 – 1.80	0.00005	-0.00195	0.0098	0.16
≥ 1.80	0.00005	-0.00190	0.0100	0.11

Table 11A-10 Variables a and b for Calculating the Fluctuating Dynamic Pressure Coefficient Using Equation 11A-33 (Castillo et al. 2015).

L_j/L_b	Y/B$_j$ > 14	
	a	b
≤ 0.80	1.50	0.21
$0.80 - 1.00$	1.80	0.21
$1.00 - 1.30$	1.00	0.15
$1.30 - 1.60$	0.40	0.12
$1.60 - 1.80$	1.33	0.23
≥ 1.80	2.50	0.35

Table 11A-11 Coefficient Values for Calculating the Fluctuating Dynamic Pressure Coefficient for Circular Jets (Bollaert, 2002).

T_u	a$_1$	a$_2$	a$_3$	a$_4$	Type of Jet
< 0.01	0.00220	-0.0079	0.0716	0.00	Compact
$0.01 - 0.03$	0.00215	-0.0079	0.0716	0.050	Low Turbulence
$0.03 - 0.05$	0.00215	-0.0079	0.0716	0.100	Moderate Turbulence
> 0.05	0.00215	-0.0079	0.0716	0.150	High Turbulence

$$C_p' = a_1 \cdot \left(\frac{Y}{D_{out}} \right)^3 + a_2 \cdot \left(\frac{Y}{D_{out}} \right)^2 + a_3 \cdot \left(\frac{Y}{D_{out}} \right) + a_4 \qquad (11A\text{-}34)$$

For $Y/D_{out} \leq 20$

For higher values of dimensionless depth, the C_p' value that corresponds to a ratio of 20 should be used as an interim rule until more information is available on its value beyond this depth. The relationships between the issuance turbulence intensity, T_u, and the dimensionless coefficients a are presented in Table 11A-11.
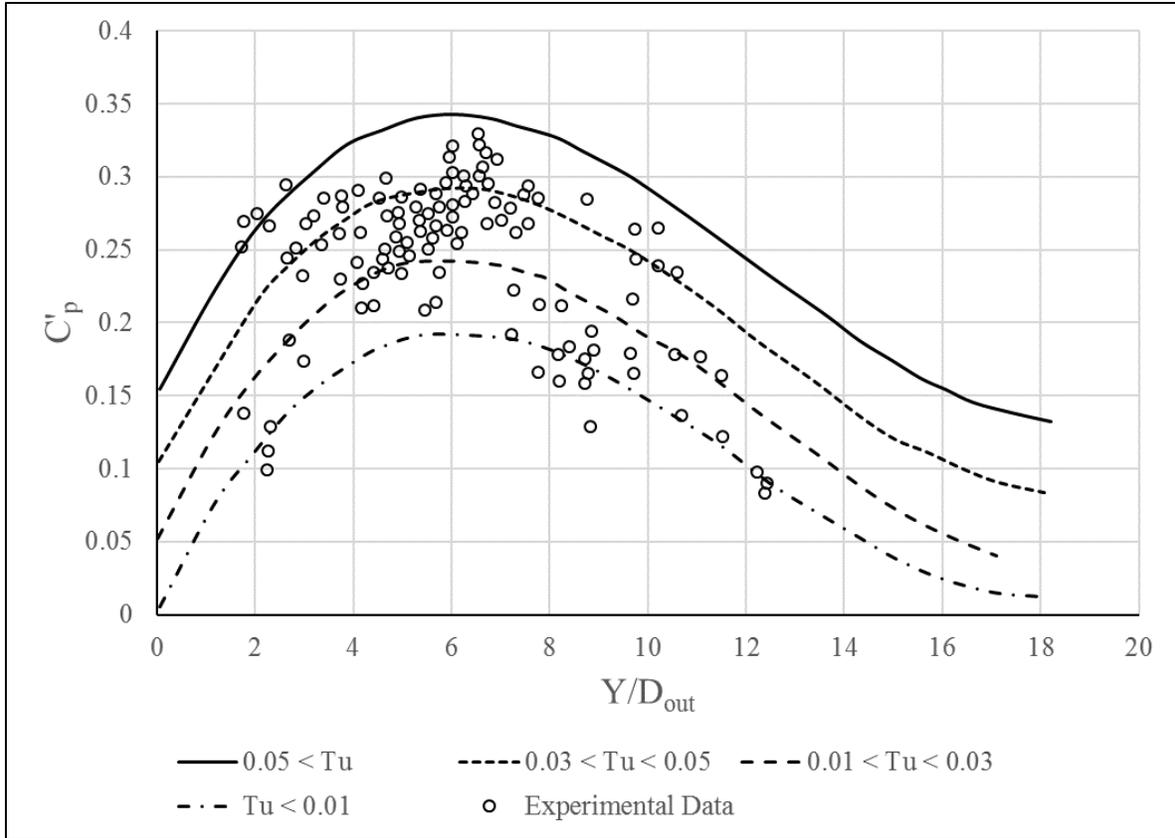
Figure 11A-11 – Adapted from Bollaert (2002).

The effect of jet breakup on the fluctuating dynamic pressure for circular jets can be determined using Equation (11A-35) and Figure 11A-12 (Annandale, 2006).

$$F = 0.607 \cdot \left(\frac{L}{L_{b\_circular}} \right)^3 - 2.179 \cdot \left(\frac{L}{L_{b\_circular}} \right)^2 + 1.622 \cdot \left(\frac{L}{L_{b\_circular}} \right) + 0.658 \quad (11A\text{-}35)$$

For $L/L_{b\_cirular} < 1.85$

and $F = 0.05$ otherwise.

Once the value of F is known, the total dynamic pressure for circular jets is calculated with Equation 11A-30, i.e.

$$P_{total} = C_p \cdot P_{jet} + F \cdot C_p^{'} \cdot P_{jet}$$
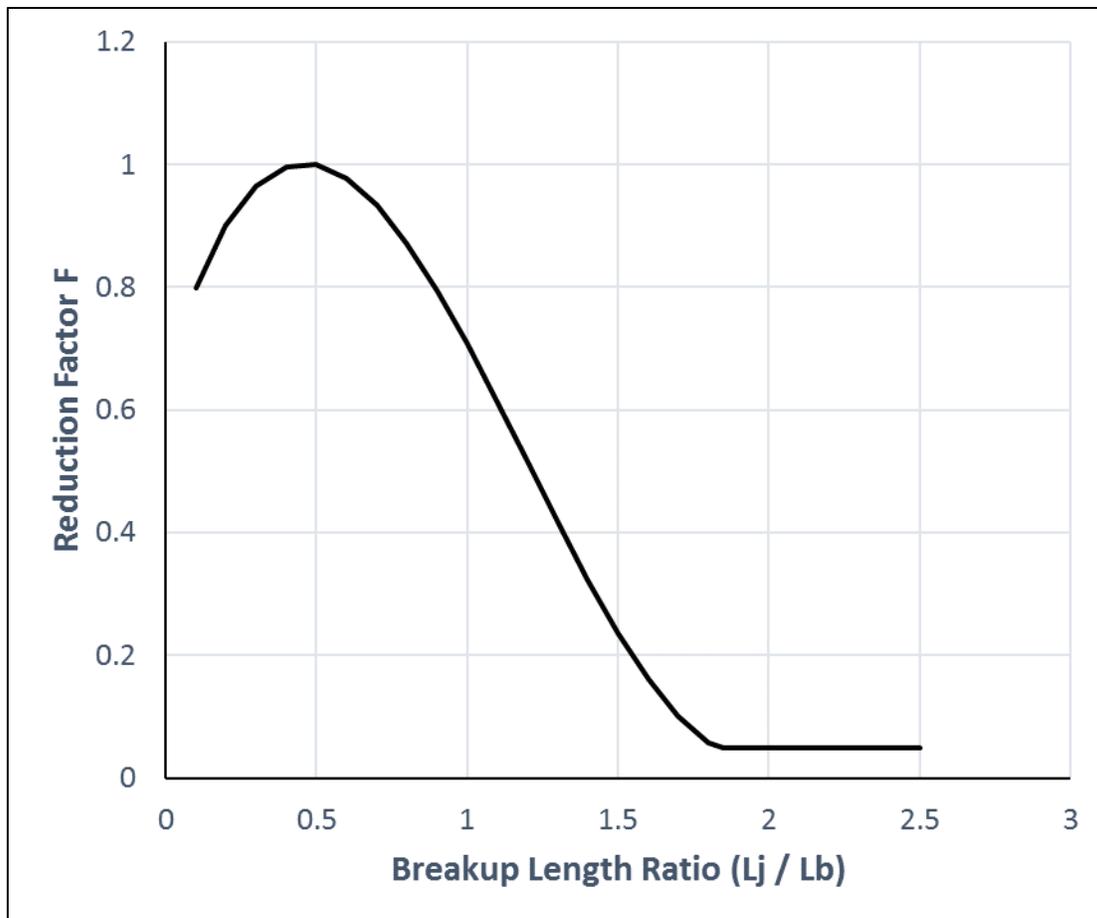
Figure 11A-12 – Adapted from Annandale (2006).

11A-7 RATE OF EROSION

Robust techniques to predict the rate of erosion of rock remains elusive. Bollaert (2002) has developed a procedure to calculate the rate of erosion of rock but the principal parameter required to make such calculations cannot be measured as no laboratories currently exist that can quantify site specific values of the relevant coefficient. Rock et al. (2016) illustrated that it may be possible to quantify the rate of rock erosion by using a total energy approach with the Erodibility Index Method, but this concept still requires further development to determine if it is viable in practice.

11A-8 COMPLEX FLOW CONDITIONS

When investigating projects with complex flow conditions preventing analytical quantification of stream power it may be necessary to use physical hydraulic model studies or computational fluid mechanics software. For example, complex flow conditions may exist when floods overtop dams and flow onto rock abutments, or in cases where flows are released under pressure downstream along a dam foundation, forming wall jets.

Physical model studies should be executed in a manner minimizing scale effects, while care should be taken to ensure that computational fluid dynamics results are realistic. Computational fluid dynamics software displays results in three-dimensional images providing the appearance of reality, although they may be faulty.

Practitioners should therefore demonstrate that the estimates of stream power are defensible when using physical hydraulic model studies or computational fluid dynamics software. Demonstrating the defensibility of results is an engineering decision making process requiring experience and expertise. A view on the process of engineering decision making that may be used as guidance is presented in Annandale (2006), Chapter 2.

Using either of the two modeling approaches requires quantification of stream power, P (watts/m^2), along the flow boundary, which can be accomplished using (Annandale, 2006),

$$P = 7.853 \cdot \rho \cdot \left(\sqrt{\frac{\tau}{\rho}} \right)^3 \qquad (11A-36)$$

Where ρ = density of water (1,000kg/m^3); τ = shear stress along the bed (Pa).

When using physical hydraulic model studies the shear stress may be quantified by measuring fluctuating dynamic pressures along the bed at an appropriate frequency[7], and quantifying shear stress as (Emmerling, 1973),

$$\tau = \frac{p'}{3} \qquad (11A-37)$$

Where p' = the root mean square of the fluctuating dynamic pressures (Pa), expressed as,

$$p' = \sqrt{\frac{\sum_{i=1}^{N} (p_i - p_m)^2}{N}} \qquad (11A-38)$$

Where p_i = pressure at time i (Pa); p_m = mean measured pressure (Pa); N = number of pressure measurements.

11A-9 ABUTMENT SCOUR

The stability of rock abutments subject to overtopping flow downstream of dams can be assessed using a block theory framework. The behavior of rock slopes, and specifically the stability of individual rock blocks, is highly influenced by the 3D orientations of discontinuities within the rock mass. In such scenarios, empirical representation of the rock mass using the Erodibility

---

[7] Measuring frequencies on the order of 100 Hz to 200 Hz may be appropriate, but needs to be assessed for each study.

Index may not be appropriate for the evaluation of scour potential, particularly for the case of large rock wedges forming portions of the abutments (Figure 11A-13).
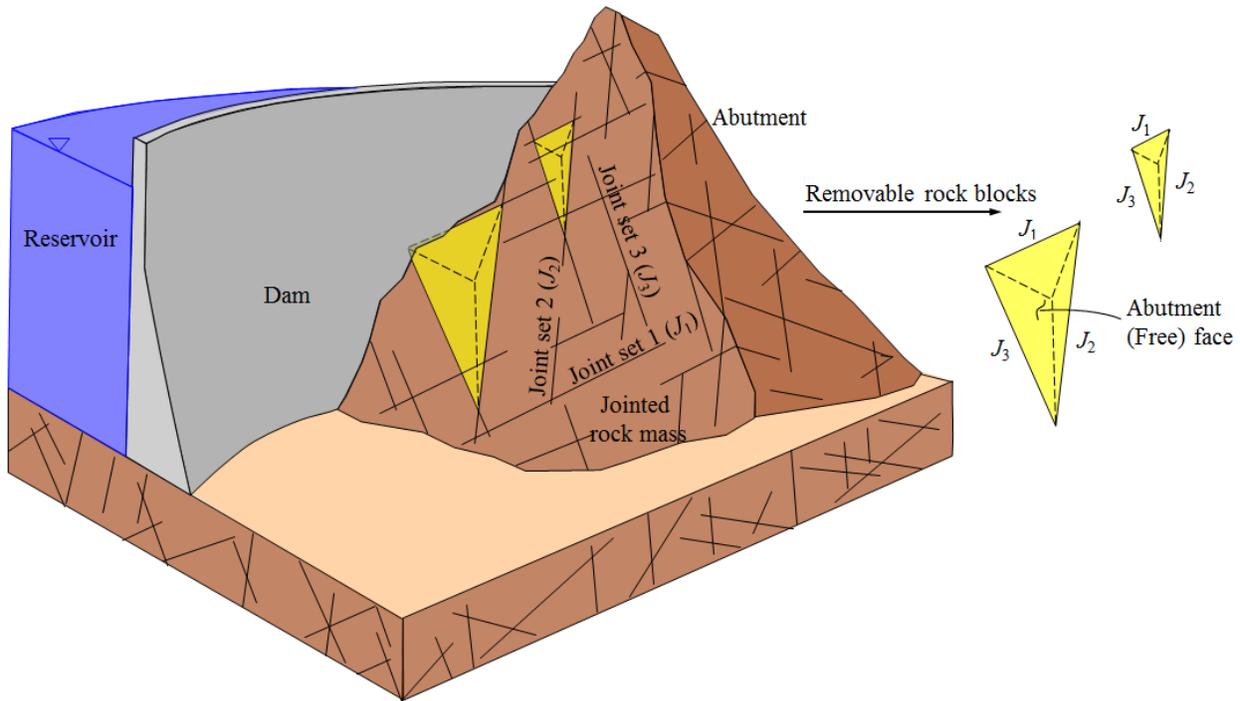
Figure 11A-13 - Schematic for removable dam abutment rock blocks.

Analysis of abutment blocks under hydraulic loading from overtopping has received little attention despite the potential for significant influence on dam and foundation stability. Block theory provides an analytical methodology for assessing removability, kinematics and stability of 3D rock blocks within a rock mass (Goodman and Shi, 1985). George (2015) developed rock mass erodibility concepts based on block theory and demonstrated using both laboratory and prototype rock spillway channels that erodibility thresholds of 3D blocks can be reasonably well predicted with this approach (George and Sitar, 2016). Application of this method to rock abutments is presented herein.

To determine whether a 3D rock block exceeds an erodibility threshold using block theory it is necessary to consider three characteristics: removability, kinematics and its stability within the rock mass; discussed in what follows.

11A-9.1 Block Theory Framework: Removability

A rock mass may be characterized by multiple joint sets that divide the rock mass into several discrete blocks. For a given number of joint sets, a corresponding number of different block shapes exist, some of which are removable from the rock mass when exposed by a free surface. For the case of dam overtopping, the abutment slopes form the free surfaces. Removable blocks are of principal interest for erodibility analysis as these are blocks that can become unstable when subject to hydraulic loading.

While block theory analysis is general for any number of joint sets and free surfaces, tetrahedral blocks (formed by three joint sets and a single free face) are the most common removable block geometry (Hatzor, 1992). Accordingly, these blocks are the focus of this framework.

For a rock mass containing three separate joint sets (J_1, J_2 and J_3), eight possible block shapes exist, only one of which is removable for a given free surface. This does not mean only one block is removable but rather many blocks can be removable if they are of that particular geometry. Each block shape is termed a "joint pyramid (JP)" and is identified by a unique three number binary code with each number indicating whether the block is above or below the corresponding joint plane. A "0" indicates the block lies in the upper half-space above the joint plane while a "1" indicates the block lies in the lower half-space below the joint plane. For example, a block with JP code 010 would indicate the block is above J_1, below J_2, and above J_3.

Using stereographic projection (Goodman, 1976), the great circle corresponding to each joint set can be plotted thus subdividing the stereonet into regions corresponding to each JP (Figure 11A-14). For an upper hemisphere stereonet, the space inside the great circle for a particular planar surface represents the area above that plane, while the space outside the great circle represents the area below that plane.
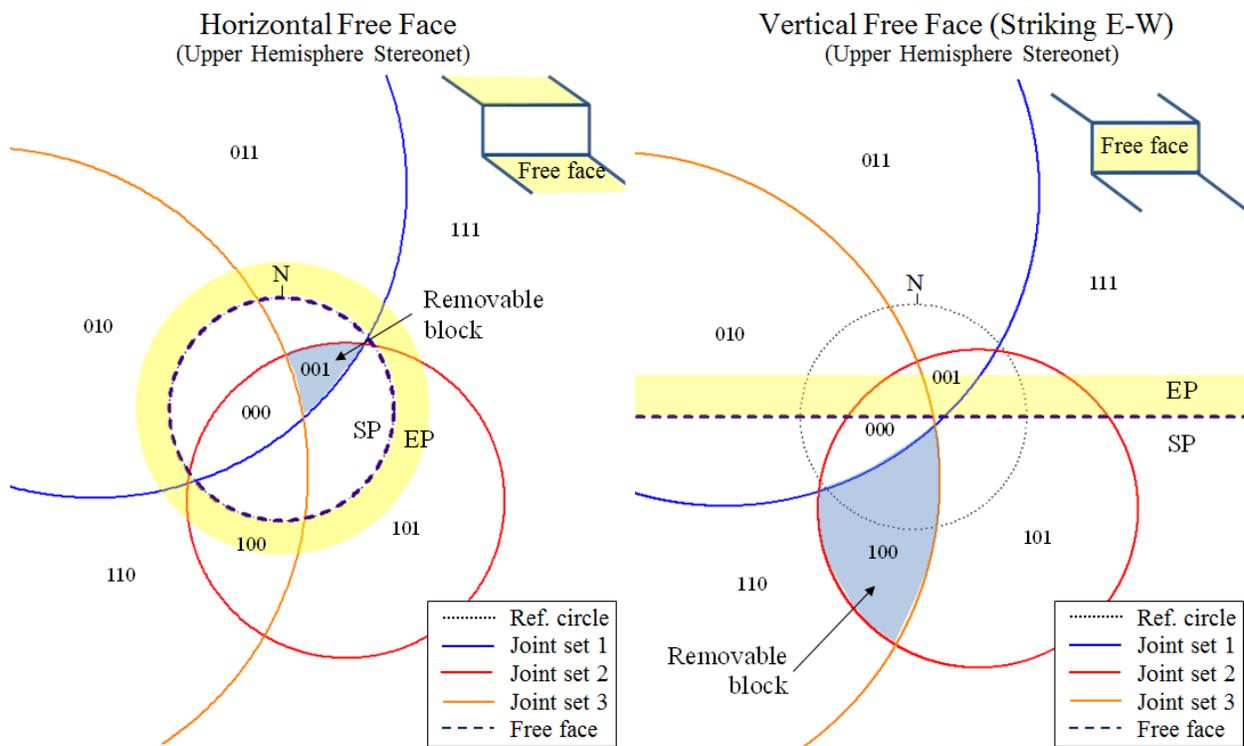
Figure 11A-14 - Upper hemisphere, equal angle stereonets showing JP codes and removable blocks for horizontal free face (left) and vertical free face striking East-West (right) (George, 2015).

According to Shi's theorem (Goodman and Shi, 1985), to be removable the JP region for a particular block must be finite and plot completely within the "space pyramid (SP)" as defined by the free face. This ensures the block is finite and can move into the opening from the rock

mass. For erodibility assessment, the free face is the rock/water or rock/air interface (assumed to be planar over the region of interest) that divides the SP (the region into which a removable block moves) from the "excavation pyramid (EP)" (the region where the block resides). In Figure 11A-14, JP 001 is a removable block from a horizontal free face, while JP 100 is a removable block from a vertical face striking East-West. (JP 000 on the horizontal face, for example, is not a removable block because it does not completely plot within the SP).

In many cases, more than three joint sets exist within a rock mass such that a large number of possible joint combinations must be examined. In these scenarios, multiple combinations of three joint sets should be analyzed to find removable tetrahedral blocks in all cases. For example, if the total number of joint sets is four the following sets should be analyzed with the free surface to yield four removable blocks: (J_1, J_2, J_3), (J_1, J_2, J_4), (J_1, J_3, J_4) and (J_2, J_3, J_4).

Once the characteristics of potentially removable blocks have been identified, as in Figure 11A-14, field identification of removable blocks on abutment slopes can proceed by detailed geologic mapping of joint traces on the abutment surface. High resolution remote sensing technologies, such as LiDAR and photogrammetry, can facilitate mapping locations were access is difficult as well as rapid characterization of joint orientations and persistence using automatic joint detection software, e.g., SplitFX (Split Engineering, 2015).

11A-9.2 Block Theory Framework: Kinematics

Whether a potentially removable block identified in Figure 11.2.4.14 is actually removable is determined by its kinematics. Scour of a removable block from the rock mass is subject to several kinematic constraints. This is a function of 3D block geometry and orientation of the resultant vector of active forces applied to the block. Subsequently, a number of kinematic failure modes exist (Figure 11A-15). These include: 1) pure translational modes, such as lifting and sliding (1-plane or 2-plane), 2) pure rotational modes, such as rotation about an edge or a corner, or 3) some combination of translation and rotation, such as slumping or torsional sliding.
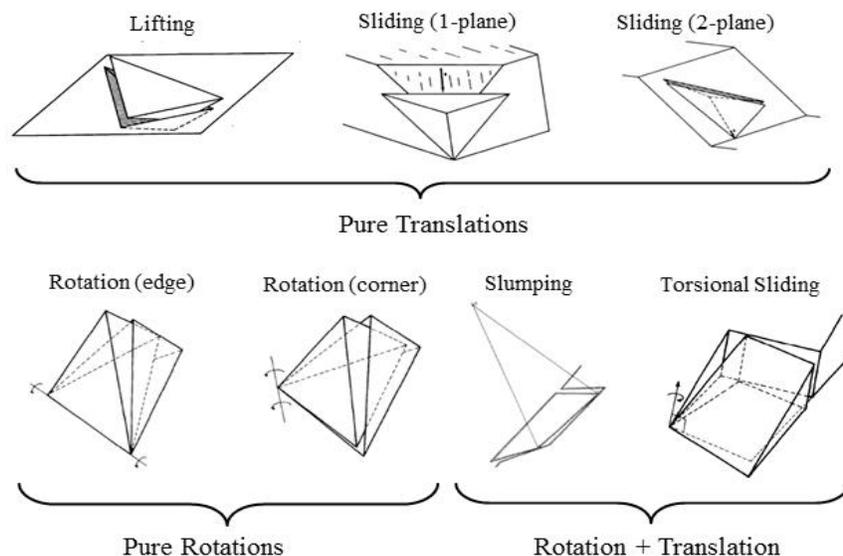
Figure 11A-15 - Kinematic block failure modes (Goodman, 1995).

For erodibility assessment, from a practical point of view, only pure translational kinematic modes are considered. A study by Mauldon (1990) indicated the probability that a tetrahedral block is both removable and rotatable is fairly low (approximately 16 percent) and, even in the case that both are true, the critical mode will almost always be one of the translations unless the friction angle of the rock joint is very high.

Criteria were developed by Goodman and Shi (1985) for assessing plausible kinematic failure modes for pure block translations. For tetrahedral blocks, there are seven translational failure modes (lifting, sliding on J_1 sliding of J_2, sliding on J_3, simultaneous sliding on J_1 and J_2, simultaneous sliding on J_1 and J_3, and simultaneous sliding on J_2 and J_3). For block movement to be feasible in one of these modes, all kinematic criteria for that mode must be satisfied. A general schematic of a removable block is shown in Figure 11A-16.
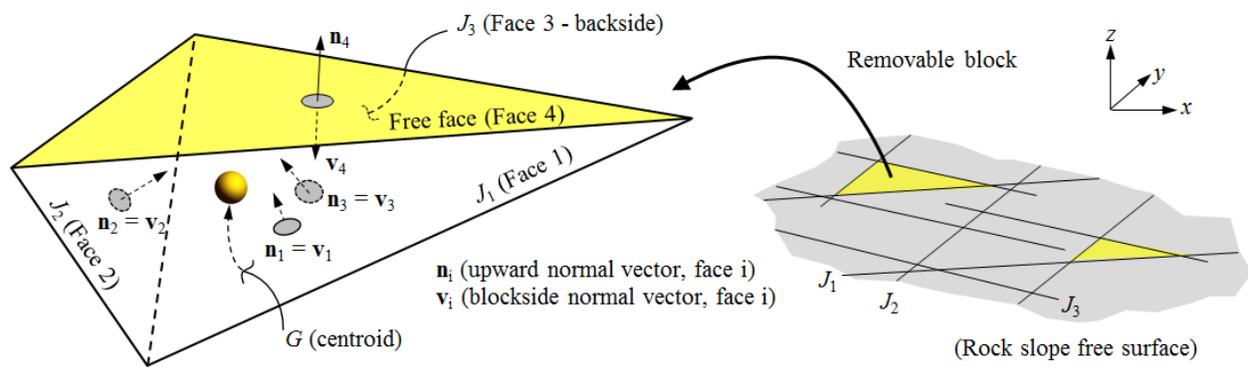
Figure 11A-16 - Removable block schematic (George, 2015).

Lifting

For pure translation modes, lifting of a block is kinematically feasible when:

$$\mathbf{s} \cdot \mathbf{n}_i > 0, \quad \text{for all I} \qquad (11A\text{-}39)$$

where $\mathbf{s}$ = direction of block movement (equal to the direction of the active resultant force vector ($\mathbf{R}$) for lifting), and $\mathbf{n}_i$ = block-side normal vector for i^{th} joint plane. In this section, **bold** font signifies a vector/matrix quantity.

This condition ensures the block moves away (lifts) from each of the bounding joint planes. The block-side normal may be calculated by Equation 11-2.2.

Sliding

Evaluation of block sliding is covered rigorously in Section 11-2.3 of this chapter.

Rotation

The evaluation of rotation requires knowledge of not only force magnitude and direction, but also the distribution of stress on each face of the block. This is typically a nonlinear finite element exercise (see Section 11-2.3, Fig 11-2.17).

11A-9.3 Block Theory Framework: Scour Application

Application of block theory to rock scour evaluation occurs through modification of the active resultant force vector (**R**) which accounts for the hydraulic load applied to a rock block due to impact from an overtopping jet. Joints bounding the block allow transmission of hydrodynamic pressures to the faces on the underside of the block, potentially leading to scour. The magnitude and orientation of **R** ultimately influences the dominant block kinematic failure mode and stability, however, block removability and kinematic constraints are unaltered. The latter two are purely related to 3D block and rock mass geometry and thus independent of any type of applied forces.

The active resultant force vector (**R**) represents a vector sum of all active forces acting on the block. For rock scour purposes, these are predominantly the hydraulic pressure (P_b) applied normal to the block faces and the self-weight of the block due to gravity ($\mathbf{W}_b$). This can be expressed as:

$$\mathbf{R} = \sum_i^n S_{bi} \cdot \mathbf{n}_i + \mathbf{W}_b \qquad\qquad (11\text{A-}40)$$

where: S_{bi} = integral of the hydraulic pressure (P_{bi}) acting over ith block face (either defined by joint planes or the free face), n = total number of block faces, and $\mathbf{n}_i$ is the normal vector to the ith face.

Very little information is available for hydrodynamic pressures within rock joints induced by overtopping jets impacting dam abutments. For simplicity, a uniform distribution of hydrodynamic pressure over the block faces is assumed, such that the above equation may be written:

$$\mathbf{R} = \sum_i^n P_{bi} \cdot A_i \cdot \mathbf{n_i} + \mathbf{W_b} = \sum_i^n \frac{1}{2} \cdot \rho \cdot \left(\mathbf{V_j} \cdot \mathbf{n_4}\right)^2 \cdot C_{ti} \cdot A_i \cdot \mathbf{n_i} + \mathbf{W_b} \qquad 11\text{A-}41$$

where A_i = area over which pressure is distributed on the ith block face, ρ = density of water, $\mathbf{V}_j$ = jet flow velocity vector at impact (for most overtopping scenarios this can simply be assumed to act in the vertical direction = (0 0 $-V_j$), $\mathbf{n}_4$ = block-side normal vector for the rock free surface, and C_{ti} = total dynamic pressure coefficient on the ith face. Note the quantity $\mathbf{V}_j \cdot \mathbf{n_4}$ yields the jet impact velocity normal to the rock slope. As the bounding joints for the block are assumed to be filled completely with water and that water will be flowing over the surface of the block, $\mathbf{W}_b$ represents the submerged weight of the block.

Should more detailed knowledge of distribution of hydrostatic water pressures surrounding the block be available, this may be implemented in Equation 11A-40. In such cases, the total weight of the block should be used for $\mathbf{W}_b$.

The total dynamic pressure coefficient is defined as:

$$C_t = X \cdot C_p + C_p' \qquad\qquad (11\text{A-}42)$$

where C_p = average dynamic pressure coefficient, C'_p = fluctuating dynamic pressure coefficient (note for circular jets an additional reduction factor to account for jet-break up determined from

Equation 11A-35 is applied to C'_p), and $X =$ factor depending on whether the block face is exposed to the surface or within the rock mass. The factor $X = 1$ for direct jet impact on the surface of the block, while for block faces within the rock mass, $X = 0.35$. Research by Federspiel et al. (2011) and later by Duarte (2014) suggests the average dynamic pressure within the joints surrounding a rock block is reduced to approximately 15 to 35 percent of the dynamic pressure at the surface when subject to an impinging jet over a joint opening. Accordingly, the upper limit is adopted here. Pressure coefficient values are based on overtopping jet hydraulics described in Section 11A-5.

Guidance on selection of appropriate pressure coefficient values for the block faces is provided in Figure 11A-17. For smaller blocks, where the jet impact area covers the majority of the block, a single value for C_t can be determined on the surface and applied to all faces using Equation 11A-42. For larger blocks, where only a portion of the jet impacts the block, a more detailed approach may be required (i.e., if jet impact conditions vary significantly across the block). The impact location and area of the jet footprint on the block free face is determined using the jet trajectory and jet thickness equations (Equation 11A-25 and Equation 11A-10, respectively). On the block free surface, at the location(s) where the jet impacts the surficial expression of the joint plane(s) bounding the block (e.g., locations A and B, Figure – 11A-17), C_t and $\mathbf{V}_j$ are calculated. For the block face(s) directly connected to the jet impact location(s), the C_t value determined at the surface is applied to the block face within the rock mass using Equation 11A-42. For the block face(s) not connected to the jet impact location(s), an average pressure value from the other block faces within the rock mass can be applied.
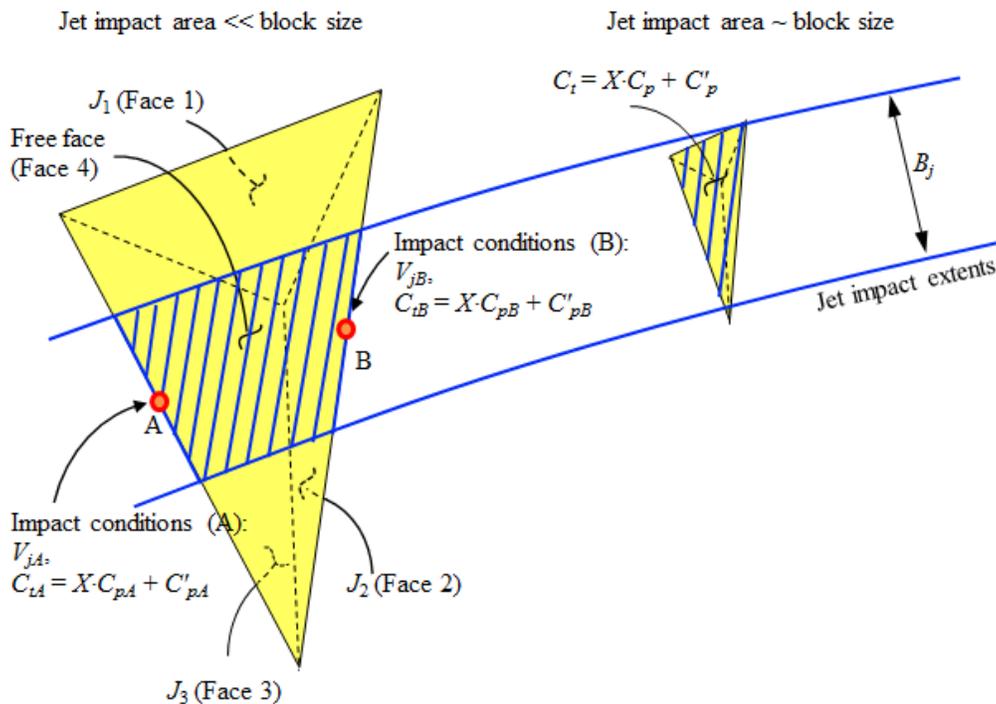

Figure 11A-17 - Loading scenarios for removable blocks subject to block size relative to jet impact area.

Other forces can be incorporated (such as flow shear force, cohesion, dam thrust force onto the block, rock bolt force) through addition of their respective vector quantities to Equation 11A-41. The assumption of uniform pressure distribution is likely conservative as the size of the block becomes large relative to the jet impact area. Similarly, the assumption to implement the submerged block weight may be conservative as well. Accordingly, the proposed procedures likely present a practical upper bound for hydraulic loads until further research can be conducted.

11A-10 ERODIBILITY CALCULATIONS

11A-10.1 Plunge Pool Example – Erodibility Index Method

This example presents a general outline to estimate scour of rock downstream of dams. The equations and approaches used here are specifically for nappe jet flow over an arch dam with an ogee crest. For other flow conditions, i.e. ski jumps and circular jets, the equations used here need to be replaced accordingly.

Consider an arch dam with an ogee crest (reference Figure 11A-6). Table 11A-12 presents dam characteristics, while essential geologic characteristics of the dam foundation are found in Table 11A-13.

Table 11A-12 Essential Dam Characteristics for Analyzing Scour.

Element	Value	Comment
Elevation of Spillway Crest (masl)[8]	1135	
Tailwater Elevation (masl)	1010	
Upstream Energy Head (h) (m)	5	Flow depth just upstream of crest[9]
Total Energy Head (H) (m)	130	1135m+5m-1010m=130m
Turbulence Intensity (T_u) (-)	0.012	Table 11A-6
K_φ (-)	1.24	See explanation of Equation (11A-10)
C_d (m$^{0.5}$/s)	2.1	Discharge coefficient

The erosion resistance of each of the rock layers is determined using the information in Tables 11A-1 to 11A-5 to quantify the numbers required for calculating the Erodibility Index, K, (Equation 11A-2) and the threshold stream power, P_t (Equation 11A-1), as demonstrated in Table 11A-14. The calculation determines that the threshold stream power of the weathered rock is 4 kW/m^2 and that of the fresh rock is 233kW/m^2. If the applied stream power by the flowing water in the plunge pool exceeds these values the rock will erode. When the applied stream power is lower than the threshold stream power of the rock, erosion will cease.

---

[8] masl = meters above sea level

[9] By making this assumption it is assumed that the kinetic energy head upstream of the dam crest is negligible. This may not always be the case and should be incorporated in the quantification of *h* if significant.

Assessment of the value of the relative ground structure number J_s requires explanation. It is reasonable to expect that the flow conditions within the plunge pool can be highly turbulent. It is therefore difficult to express with confidence the dominant flow direction of the water relative to the dip direction and dip of the rock along the boundary of the plunge pool. For this reason, the minimum value of the relative ground structure number is used, which in the case for equisided rock block shapes amounts to 0.49.

Table 11A-13 Relevant Geologic Characteristics.

Variable	Weathered Rock	Fresh Rock
Unconfined Compressive Strength (MPa)	5	50
Weight of Rock (kN/m^3)	24	27
RQD	5	80
Joint Sets	3	3
Discontinuities	Smooth, undulating, tight joints	Smooth, undulating, tight joints
Block shape	Equisided	Equisided
Top Elevation (masl)	1,000	970
Bottom Elevation (masl)	970	900
Dip Direction (degree Azimuth)	180	180
Dip (degree)	80	20

The characteristics of the plunging jet and the dissipation of stream power in the plunge pool require quantification next. The constants required to execute these calculations are

Acceleration of gravity, $g = 9.807$m/s^2

Mass density of water, $\rho = 1,000$kg/m^3

With the total energy head, H, and energy head upstream of the crest, h, known, the characteristics of the plunging jet can be calculated as shown in Tables 11A-15. The result from this table, i.e. the unit stream power of the jet, P_{jet}, at the surface of the tailwater, is used to quantify the dissipation of stream power within the plunge pool.

To quantify the dissipation of stream power as the jet plunges through the air and flows through the plunge pool, Equation 11A-31 and Tables 11A-7 and 11A-8 (or Figure 11A-9) are used to determine the values of the average dynamic pressure coefficient, C_p. Equations 11A-32 and 11A-33, and Tables 11A-9 and 11A-10 (or Figure 11A-10) are used to quantify the fluctuating dynamic pressure coefficient values, C'_p. With these two sets of values known as a function of

depth below the tailwater surface, Equation 11A-30 is used to quantify the dissipation of jet stream power as a function of water depth.

Table 11A-14 Quantification of the Threshold Stream Power of Rock Layers.

| Variable | Rock Type | | Comment |
	Weathered Rock	Fresh Rock	
Ms (-)	**3.76**	**50.00**	**Equations 11A-3, 11A-4 and 11A-5**
RQD (-)	5	80	Core Log Data
Jn (-)	2.73	2.73	Tables 11A-2
Kb (-)	**2**	**29**	**Equation 11A-6**
Jr (-)	2	2	Table 11A-3
Ja (-)	1	1	Table 11A-4
Kd (-)	**2**	**2**	**Equation 11A-7**
Js (-)	**0.49**	**0.49**	**Table 11A-5; also see explanation in text**
K (-)	**7**	**1436**	**Equation 11A-2**
Pt (kW/m²)	**4**	**233**	**Equation 11A-1**

Table 11A-15 Plunging Jet Characteristics.

Element	Value	Comment
Issuance Velocity (m/s)	14.00	$V_i = 2 \cdot \sqrt{g \cdot h}$
Unit Discharge (m²/s)	23.48	$q = h^{3/2} \cdot C_d$
Total Energy Head (m)	130	From Table 11A-12
Issuance Jet Thickness (m)	1.68	$B_i = q/V_i$
φ (-)	0.015	$K_\varphi \cdot T_u$
Jet Footprint Thickness (m)	2.02	Equation (11A-10)
Breakup Length L_{b_nappe} (m)	16.87	Equation (11A-11) with $\Gamma = 0.85$
Jet Length L (m)	130	Assume equal to energy head H
Breakup Length Ratio (-)	7.7	L/L$_b$
Unit Stream Power P_{jet} (kW/m²)	14,489	Equation (11A-9) for unit flow width (1m)

The change in total jet stream power below the plunge pool water surface, P_{total} (using Equations 11A-31 to 11A-33) is shown in Table 11A-16 and in Figure 11A-13. The table and graph also contains the threshold stream power of the rock, P_t, which, when compared to the total jet stream power provides a means of calculating the maximum scour elevation.

The first column in Table 11A-16 contains the water depth below the plunge pool water surface, which is used to calculate the ratio Y/B_j that is required to quantify the dynamic pressure coefficient, C_p, and the fluctuating dynamic pressure coefficient, C'_p. These two values are added in column 5, which is then multiplied with the jet stream power at the plunge pool surface (i.e. 14,489 kW/m^2) to account for energy loss as the jet plunges through the atmosphere and as it discharges through the water in the plunge pool (column 6). Column 7 contains the threshold stream power of the rock, which commences at elevation 1,000masl (the bed elevation of the river). Comparison between the total jet stream power in column 6 and the rock threshold stream power in column 7, performed in column 9, indicates the maximum scour depth is estimated to occur at elevation 970masl. The jet stream power and threshold stream power of the rock are also compared in Figure 11A-13, illustrating the elevation of maximum scour depth.
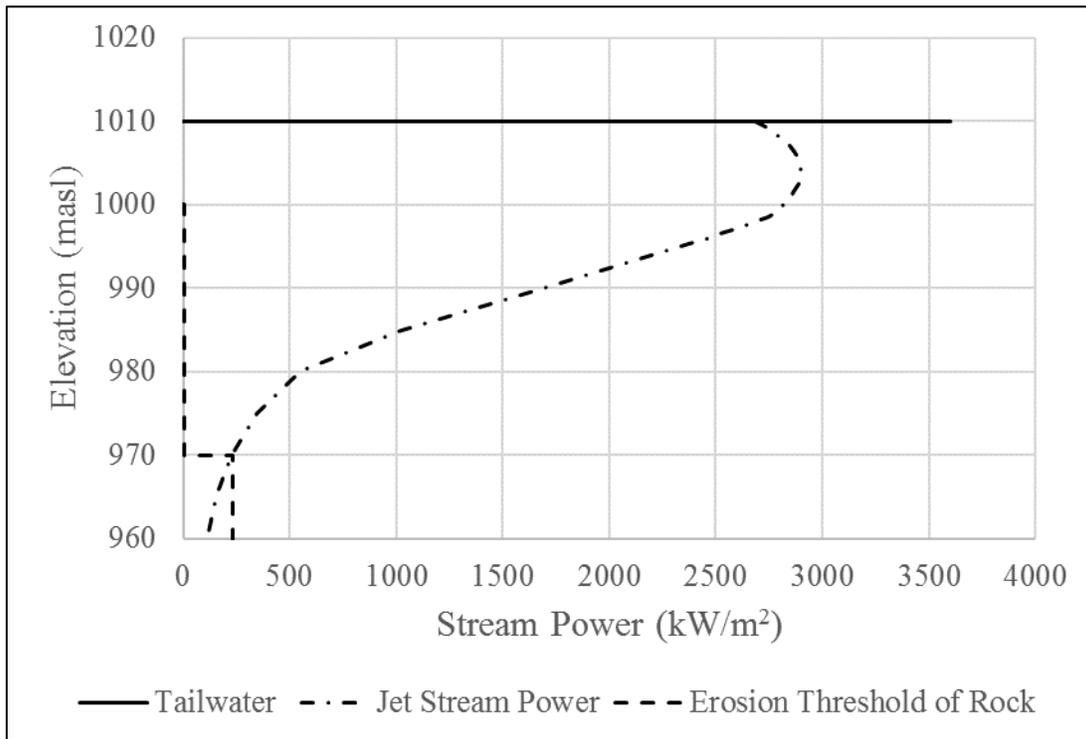
Figure 11A-13

It is noted that the jet stream power just below the water surface (2,688 kW/m^2), calculated in Table 11A-16 and illustrated in Figure 11A-13, is lower than the estimated stream power of the plunging jet at the surface of the plunge pool (14,489 kW/m^2). The reason for this is that the estimated jet stream power at the water surface of the plunge pool does not account for energy loss as the jet plunges through the atmosphere. That energy loss and the loss as it eventually travels through the water in the plunge pool, is accounted for with the dynamic and fluctuating dynamic pressure coefficients, C_p and C'_p (Castillo et al., 2015; Castillo and Carrillo, 2016).

Table 11A-16 Scour Assessment: Total Jet Stream Power Change Below Tailwater Level Compered to Threshold Stream Power of Rock.

Depth below Tailwater Y (m)	Y/Bj	C_p	C'_p	$C_p + C'_p$	SP (kW/m²)	Pt (kW/m²)	Elevation below Tailwater (masl)	Scour (Y/N)
0	0.00	0.071	0.110	0.181	2688		1010.00	
0.5	0.25	0.071	0.112	0.183	2723		1009.50	
1	0.50	0.071	0.114	0.185	2755		1009.00	
1.5	0.74	0.071	0.116	0.187	2783		1008.50	
2	0.99	0.071	0.118	0.189	2808		1008.00	
2.5	1.24	0.071	0.120	0.191	2830		1007.50	
3	1.49	0.071	0.121	0.192	2849		1007.00	
3.5	1.74	0.071	0.122	0.193	2864		1006.50	
4	1.98	0.071	0.123	0.194	2877		1006.00	
4.5	2.23	0.071	0.123	0.194	2887		1005.50	
5	2.48	0.071	0.124	0.195	2894		1005.00	
5.5	2.73	0.071	0.124	0.195	2898		1004.50	
6	2.98	0.071	0.124	0.195	2899		1004.00	
6.5	3.22	0.071	0.124	0.195	2898		1003.50	
7	3.47	0.071	0.124	0.195	2894		1003.00	
7.5	3.72	0.071	0.123	0.194	2888		1002.50	
8	3.97	0.071	0.123	0.194	2879		1002.00	
8.5	4.22	0.071	0.122	0.193	2868		1001.50	
9	4.46	0.071	0.121	0.192	2854		1001.00	
9.5	4.71	0.071	0.120	0.191	2839		1000.50	
10	4.96	0.071	0.119	0.190	2821	4	1000.00	Y
10.5	5.21	0.071	0.118	0.189	2801	4	999.50	Y
11	5.46	0.071	0.116	0.187	2779	4	999.00	Y
11.5	5.70	0.071	0.114	0.185	2749	4	998.50	Y
12	5.95	0.069	0.113	0.181	2692	4	998.00	Y
12.5	6.20	0.067	0.111	0.177	2634	4	997.50	Y
13	6.45	0.065	0.109	0.173	2576	4	997.00	Y
13.5	6.70	0.063	0.107	0.169	2516	4	996.50	Y
14	6.95	0.061	0.105	0.165	2456	4	996.00	Y
14.5	7.19	0.059	0.102	0.161	2395	4	995.50	Y
15	7.44	0.057	0.100	0.157	2333	4	995.00	Y
20	9.92	0.043	0.071	0.114	1687	4	990.00	Y
25	12.40	0.032	0.037	0.069	1021	4	985.00	Y
30	14.88	0.023	0.014	0.037	552	4	980.00	Y
35	17.36	0.017	0.006	0.023	344	4	975.00	Y
40	19.84	0.013	0.002	0.015	228	4	970.00	Y
45	22.32	0.010	0.001	0.011	158	233	965.00	N

Depth below Tailwater Y (m)	Y/Bj	C_p	C'_p	$C_p + C'_p$	SP (kW/m²)	Pt (kW/m²)	Elevation below Tailwater (masl)	Scour (Y/N)
50	24.80	0.007	0.000	0.008	112	233	960.00	N
55	27.28	0.005	0.000	0.005	81	233	955.00	N
60	29.77	0.004	0.000	0.004	60	233	950.00	N
65	32.25	0.003	0.000	0.003	44	233	945.00	N
70	34.73	0.002	0.000	0.002	32	233	940.00	N
75	37.21	0.002	0.000	0.002	24	233	935.00	N
80	39.69	0.001	0.000	0.001	18	233	930.00	N
85	42.17	0.001	0.000	0.001	13	233	925.00	N
90	44.65	0.001	0.000	0.001	10	233	920.00	N
95	47.13	0.000	0.000	0.000	7	233	915.00	N
100	49.61	0.000	0.000	0.000	5	233	910.00	N
105	52.09	0.000	0.000	0.000	4	233	905.00	N
110	54.57	0.000	0.000	0.000	3	233	900.00	N

11A-10.2 Abutment Scour Example

This example presents a general outline to estimate scour of large rock wedges from dam abutments. For simplicity, the dam and overtopping jet characteristics from the previous example are used (Table 11A-13). A schematic showing the dam geometry with respect to the abutment is shown in Figure 11A-19 while geologic parameters are provided in Table 11A-17.
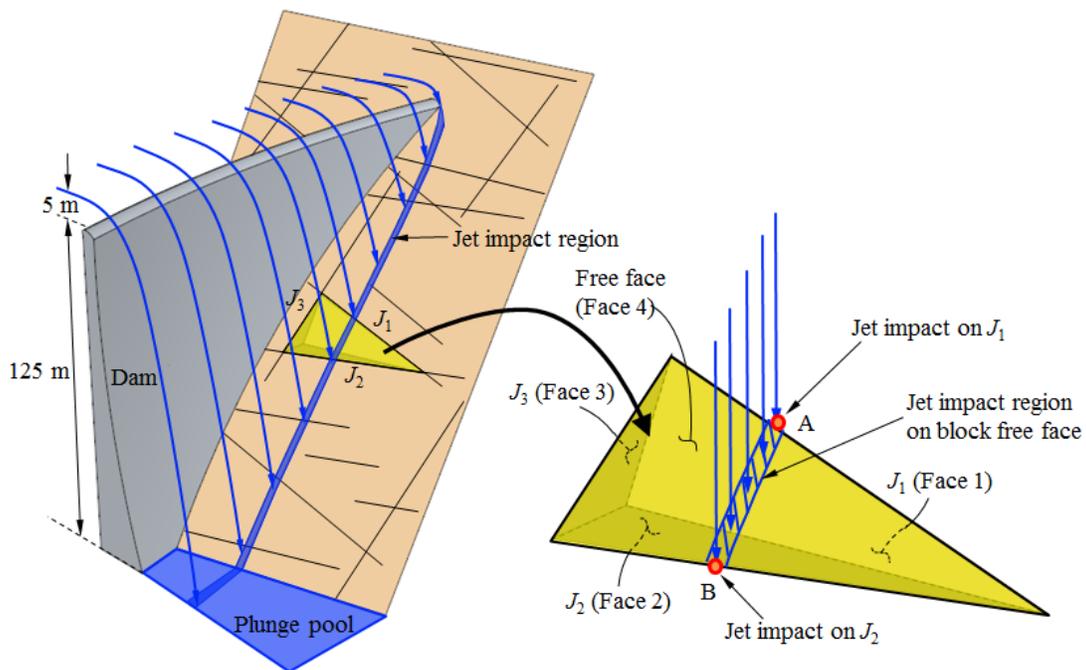

Figure 11A-19 – Schematic of overtopping jet onto removable abutment block.

Table 11A-17 Additional Rock Mass and Block Parameters.

| Variable	Value	Comment
Abutment Dip/Dip Direction (deg.)	45/255	Planar surface fit to abutment slope
Dip/Dip Direction J_1 (deg.)	85/270	
Dip/Dip Direction J_2 (deg.)	20/060	
Dip/Dip Direction J_3 (deg.)	75/355	
Friction Angle J_1 (deg.)	40	
Friction Angle J_2 (deg.)	40	
Friction Angle J_3 (deg.)	40	
Block Face 1 Area A_1 (m^2)	525	Calculated from mapped block
Block Face 2 Area A_2 (m^2)	423	Calculated from mapped block
Block Face 3 Area A_3 (m^2)	182	Calculated from mapped block
Block Face 4 Area A_4 (m^2)	560	Calculated from mapped block
Block Volume V_b (m^3)	2,814	Calculated from mapped block
Rock Density ρ_r (kg/m^3)	2,700	
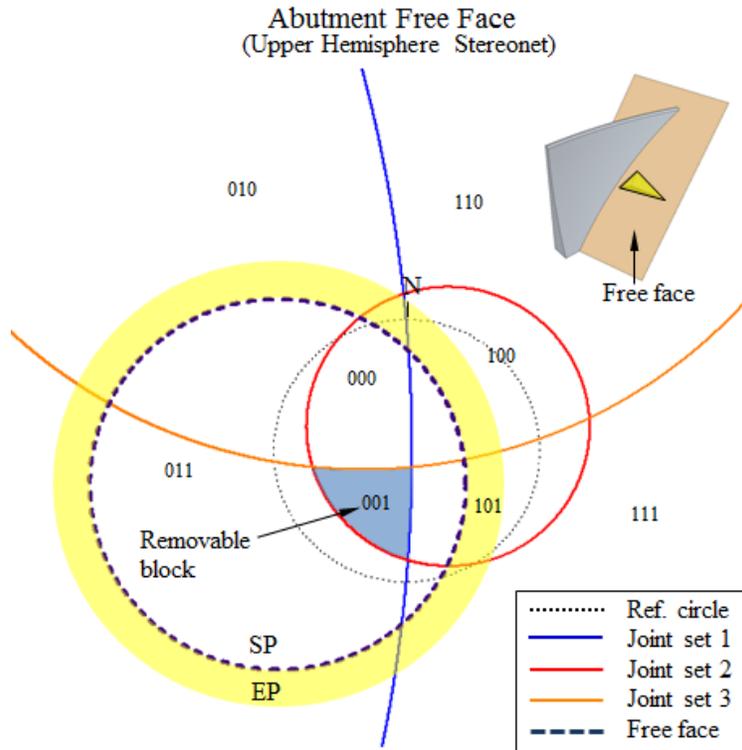
Figure 11A-20 - Upper hemisphere equal angle stereonet showing JP codes and removable block for the dam abutment slope.

A planar surface is fit to the abutment slope with a dip/dip direction (deg.) of 45/255 which represents the free surface from which blocks may be eroded. For more complex slope geometries, multiple surfaces may exist creating additional removable blocks. From stereographic projection, the removable block JP is found based on the orientations of the rock joints and the orientation of the abutment slope (Figure 11A-20). As indicated, JP 001 plots entirely within the SP as defined by the great circle for the abutment slope and is therefore removable. This block type resides above J_1, above J_2 and below J_3,

Removability analysis provides the general geometric shape for removable blocks (as defined by the JP code), but does not point to specific blocks within an outcrop. Accordingly, detailed geologic mapping of joint traces is required to pinpoint the locations of these block types on the abutment. In the schematic shown in Figure 11A-19, a large single block is identified which forms the focus of this example.

The trajectory along the centerline of the overtopping jet is determined using Equation 11A-25 (assuming an issuance angle $\theta = 50$ degree) and the thickness of the jet (B_j) upon impact with the rock abutment is determined using Equation 11A-10. The jet impact region on the abutment and across the removable block is shown in Figure 11A-19. At locations A and B, the jet impacts bounding block joint planes J_1 and J_2, respectively, which allow transmission of hydrodynamic pressures to the underside of the block. Jet impact characteristics are presented in Table 11A-18.

The use of 3D computer drafting software can be helpful tool to plot the location of jet impact as well as determine block size parameters such as the volume and area of faces.

Table 11A-18 Jet Impact Characteristics.

Variable	Value Loc. A	Value Loc. B	Comment
Total Energy Head H (m)	63.7	74.6	Elev. difference from reservoir level to impact elevation
Velocity V_j (m/s)	35.3	38.3	$V_j = \sqrt{2gH}$
Velocity Vector $\mathbf{V}_j$ (m/s)	(0 0 -35.3)	(0 0 -38.3)	Assume only vertical component
Jet Footprint Thickness B_j (m)	1.57	1.64	Equation 11A-10
Jet Footprint Area on Block A_j (m^2)		29.0	Calculate from plot of jet impact region on block surface
Jet Length L (m)	63.7	74.6	Assume equal to energy head H
Breakup Length L_{b_nappe} (m)		16.87	Equation 11A-11 with $\Gamma = 0.85$
Breakup Length Ratio (-)	3.8	4.4	L/L_b
C_p (-)	0.07	0.07	Table 11A-7, Figure 11A-9 for $Y/B_j = 0$
C'_p (-)	0.11	0.11	Equation 11A-32, Figure 11A-10 for $Y/B_j = 0$
C_{t1} Block Face 1 (-)	0.135	-	Equation 11A-42 with $X = 0.35$
C_{t2} Block Face 2 (-)	-	0.135	Equation 11A-42 with $X = 0.35$

Variable	Value Loc. A	Value Loc. B	Comment
C_{t4} Block Face 4 (Free Face) (-)		0.180	Equation 11A-42 with $X = 1$
P_{b1} Block Face 1 (kPa)	42.0	-	$P_{b1} = \frac{1}{2} \cdot \rho \cdot (V_j \cdot \mathbf{v_4})^2 \cdot C_{t1}$ with V_j defined at loc. A
P_{b2} Block Face 2 (kPa)	-	49.2	$P_{b2} = \frac{1}{2} \cdot \rho \cdot (V_j \cdot \mathbf{v_4})^2 \cdot C_{t2}$ with V_j defined at loc. B
P_{b3} Block Face 3 (kPa)		45.6	C
P_{b4} Block Face 4 (Free Face) (kPa)		60.9	$P_{b4} = \frac{1}{2} \cdot \rho \cdot (V_j \cdot \mathbf{v_4})^2 \cdot C_{t4}$ with V_j = avg. of V_j (loc. A) and V_j (loc. B)

From the estimated hydrodynamic pressures on the block faces induced by the overtopping jet, the active resultant force vector (**R**) is calculated. Once **R** is determined, the kinematic criteria for all failure modes are evaluated using Equations 11A-39 to 11A-44 to find the applicable mode. For this example under the given hydraulic loading regime, the kinematic mode is simultaneous sliding on J_2 and J_3. This indicates the block moves away from J_1, while moving into J_2 and J_3. Finally, block stability is evaluated using the corresponding limit equilibrium equation for 2-plane sliding (Equation 11A-47). Doing so yields $F_b = -25,170$ kN indicating the block is stable. Table 11A-19 shows the individual forces comprising **R** and the overall stability results of the block determined by block theory analysis.

Table 11A-19 Active Resultant Force Vector and Block Stability Results.

Element	Value	Comment
Hydrodynamic Force Face 1 (kN)	(-21,960 0 1,918)	$P_{b1} \cdot A_1 \cdot \mathbf{v}_1$
Hydrodynamic Force Face 2 (kN)	(6,158 3,558 19,556)	$P_{b2} \cdot A_2 \cdot \mathbf{v}_2$
Hydrodynamic Force Face 3 (kN)	(697 -7,982 -2,149)	$P_{b3} \cdot A_3 \cdot \mathbf{v}_3$
Hydrodynamic Force Face 4 (kN)	(1,207 323 -1,249)	$P_{b4} \cdot A_j \cdot \mathbf{v}_4$
Block Weight $\mathbf{W}_b$ (kN)	(0 0 -46,913)	Submerged
R (kN)	(-13,899 -4,101 -28,836)	Equation 11A-41
Kinematic Mode	S23	Simultaneous sliding on J_2 and J_3. All kinematic constrains in Equation 11A-44 are satisfied
F_b (kN)	-25,170	Equation 11A-47, block is *stable*

11A-11 REFERENCES

Annandale, G.W., 2006. Scour Technology; Mechanics and Engineering in Practice, McGraw-Hill: New York, 430 p.

Annandale, G.W., 1995, Erodibility: Journal of Hydraulic Research, v. 33, no. 4, p. 471-494.

Bollaert, E.F.R., 2002, Transient water pressures in joints and formation of rock scour due to high-velocity jet impact [PhD Thesis]: Laboratory of Hydraulic Constructions, Ecole Polytechnique Federale de Lausanne, Switzerland. 297 p.

Castillo, L.G. and Carrillo, J.M. 2016. Pressure and Velocity Distributions in Plunge Pools, 2nd International Seminar on Dam Protection Against Overtopping, Fort Collins, Colorado, USA.

Castillo, L.G., Carrillo, J.M. and Blazquez, A. 2015. Plunge pool mean dynamic pressures: A temporal analysis in nappe flow case, J. Hydraul. Res., 53, No. 1, 101-118.

Duarte, R.X.M. (2014). Influence of air entrainment on rock scour development and block stability in plunge pools, Communication No. 59. Ph.D. Dissertation. Laboratory of Hydraulic Constructions. Ecole Polytechnique Federale de Lausanne, Switzerland.

Emmerling, R. 1973. Instantaneous wall pressure under a turbulent boundary layer flow, Max-Planck-Institut fur Stromungsforschung, Rep. No. 9.

Ervine, D.A., Falvey, H.T., and Withers, W. 1997. Pressure Fluctuations on Plunge Pool Floors, Journal of Hydraulic Research, Vol. 35, No. 2, pp. 257 – 279.

Federspiel, M.P.E.A., Bollaert, E.F.R. and Schleiss, A.J. (2011). Dynamic response of a rock block in a plunge pool due to asymmetrical impact of a high-velocity jet. Proc. of the 34th IAHR World Congress, Brisbane, Australia, 2404-2411.

George, M.F. (2015). 3D block erodibility: Dynamics of rock-water interaction in rock scour. Ph.D. Dissertation. University of California - Berkeley.

George, M.F. and Sitar, N. (2016). Prototype measurements of rock block erosion: Implications for dam foundation and spillway erodibility assessment. Proc. of the 59th Annual Meeting of the Assoc. of Environmental & Engineering Geologists (AEG), Kona, HI, USA.

Goodman, R.E. (1976). Methods of geological engineering in discontinuous rocks, St. Paul, MN, West Publishing Company.

Goodman, R.E. (1995). Block theory and its application. Géotechnique, 45(3): 383-423.

Goodman, R.E. and Shi, G. (1985). Block theory and its application to rock engineering, Prentice Hall: Englewood Cliffs, NJ, 338 p.

Hatzor, Y. (1992). Validation of block theory using field case histories. Ph.D. Dissertation. University of California - Berkeley.

Laugier, F., Leturcq, T. and Blancher, B. 2015. Stability of dams during floods: Methods to assess the risk of downstream foundation erodibility due to overflowing above dam crest, Proc. Colloque CFBR: "Fondations des barrages: caractersisation, traitements, surveillance, rehabilitation

Mauldon, M. (1990). Probability aspects of the removability and rotatability of tetrahedral blocks. International Journal of Rock Mechanics and Mining Sciences & Geomechanics Abstracts, 27(4): 303-307.

Pfister, M., Hager, W.H., Boes, R.M., 2016. Discussion: Trajectories and air flow features of ski jump-generated jets. Journal of Hydraulic Research, v. 54, no. 2, pp. 245-247.

Pfister, M., Hager, W.H., Boes, R.M., 2014. Trajectories and air flow features of ski jump-generated jets. Journal of Hydraulic Research, v. 52, no. 3, pp. 336-346.

Rock, A.I., Annandale, G.W. and Higgins, J.D. 2016. Towards Quantifying Rate of Scour using the Erodibility Index Method: Case Study, Proc. ICSE 2016, Oxford, U.K.

Rock, A.J. 2015. A Semi-Empirical Assessment of Plunge Pool Scour: Two-Dimensional Application of Annandale's Erodibility Index Method on Four Dams in British Columbia, Canada: M.S. Thesis, Department of Geological Engineering, Colorado School of Mines, Golden, CO

Split Engineering (2015). Split FX rock mass characterization software Version 2.3. http://www.spliteng.com/products/split-fx-software.

Wahl, T.L., Frizell, K.H., & Cohen, E.A., 2008, Computing the trajectory of free jets: Journal of Hydraulic Engineering, v. 134, no. 2, pp. 256-260.